

ABSTRACT

Title of dissertation: ENGINEERING A QUANTUM MANY-BODY
 HAMILTONIAN WITH TRAPPED IONS

Aaron Christopher Lee,
Doctor of Philosophy, 2016

Dissertation directed by: Professor Christopher Monroe
 Joint Quantum Institute,
 University of Maryland Department of Physics
 and
 National Institute of Standards and Technology

While fault-tolerant quantum computation might still be years away, analog quantum simulators offer a way to leverage current quantum technologies to study classically intractable quantum systems. Cutting edge quantum simulators such as those utilizing ultracold atoms are beginning to study physics which surpass what is classically tractable. As the system sizes of these quantum simulators increase, there are also concurrent gains in the complexity and types of Hamiltonians which can be simulated. In this work, I describe advances toward the realization of an adaptable, tunable quantum simulator capable of surpassing classical computation. We simulate long-ranged Ising and XY spin models which can have global arbitrary transverse and longitudinal fields in addition to individual transverse fields using a linear chain of up to 24 $^{171}\text{Yb}^+$ ions confined in a linear rf Paul trap. Each qubit is encoded in the ground state hyperfine levels of an ion. Spin-spin interactions are engineered by the application of spin-dependent forces from laser fields, coupling

spin to motion. Each spin can be read independently using state-dependent fluorescence. The results here add yet more tools to an ever growing quantum simulation toolbox. One of many challenges has been the coherent manipulation of individual qubits. By using a surprisingly large fourth-order Stark shifts in a clock-state qubit, we demonstrate an ability to individually manipulate spins and apply independent Hamiltonian terms, greatly increasing the range of quantum simulations which can be implemented. As quantum systems grow beyond the capability of classical numerics, a constant question is how to verify a quantum simulation. Here, I present measurements which may provide useful metrics for large system sizes and demonstrate them in a system of up to 24 ions during a classically intractable simulation. The observed values are consistent with extremely large entangled states, as much as $\sim 95\%$ of the system entangled. Finally, we use many of these techniques in order to generate a spin Hamiltonian which fails to thermalize during experimental time scales due to a meta-stable state which is often called prethermal. The observed prethermal state is a new form of prethermalization which arises due to long-range interactions and open boundary conditions, even in the thermodynamic limit. This prethermalization is observed in a system of up to 22 spins. We expect that system sizes can be extended up to 30 spins with only minor upgrades to the current apparatus. These results emphasize that as the technology improves, the techniques and tools developed here can potentially be used to perform simulations which will surpass the capability of even the most sophisticated classical techniques, enabling the study of a whole new regime of quantum many-body physics.

ENGINEERING A QUANTUM MANY-BODY HAMILTONIAN WITH TRAPPED IONS

by

Aaron Christopher Lee

Dissertation submitted to the Faculty of the Graduate School of the
University of Maryland, College Park in partial fulfillment
of the requirements for the degree of
Doctor of Philosophy
2016

Advisory Committee:
Professor Christopher Monroe, Chair/Advisor
Professor Andrew Childs
Professor Ian Spielman
Professor James Williams
Professor Mohammad Hafezi

© Copyright by
Aaron Christopher Lee
2016

Acknowledgments

To Ada, the love of my life

Acknowledgments

When I began my journey down this road, I had no clue about what type of people that I would meet along the way. As luck would have it, I have had the great privilege to work beside scientists who were not only good at their job but good people.

I first and foremost want to thank Chris Monroe, without whom none of this would have been possible. Chris is not just a world class physicist, but also a superb manager of his people. I have always enjoyed the benefit of his insight into field while simultaneously able to contribute my own ideas. This is a difficult balance to achieve, but Chris makes it look easy.

I also want to thank Phil Richerme who to this day remains one of the smartest people I know. His positive viewpoint was a constant source of motivation which coupled to his careful, insightful consideration of problems makes him a physicist I emulate to this day.

Before he left us for sunny California, I had the great pleasure of working with Wes Campbell who still stands as one of my foremost examples of what a physicist should be. His careful, methodical approach to problems together with being one of the most hilarious people I've met is something I continue to emulate today.

My years here at UMD would not have been the same without the two grad-students who spent years putting up with my antics, Crystal Senko and Jacob Smith. Crystal and Jake were a large part of the reason that I enjoyed going into work in the morning, even when nothing was working. Their good humor, intelligence, and

sheer determination made results which seemed impossible all too easy. My best wishes to both of you in your endeavors.

I also want to thank the other post-docs and grad students who I have had the privilege to work with directly: Jiehang Zhang, Paul Hess, Brian Neyenhuis, Emily Edwards, Kihwan Kim, Simcha Korenblit, Rajibul Islam and Antonis Kyprianidis. Each of you has taught me a lot and I thank you for your patience and guidance.

To all the other ion trappers who were always available to lend advice or equipment, thank you for all of the help.

Without the support of our various funding agencies, this work could not have been accomplished. Thanks to the ARO Atomic Physics Program, the AFOSR MURI on Quantum Measurement and Verification, and the NSF Physics Frontier Center at JQI who have supported this research.

Despite their assertions that they do not understand what I do, my parents, Larry and Janice Lee, have always supported me throughout grad school, even when it took their grandchildren 3000 miles away. They have provided help and encouragement when it was needed and have made a great many sacrifices to get me here today. My brother Alex Lee has always been a source of positive energy these last few years. Thank you all for everything you have done for me.

Finally, I want to thank Ada, my wife, for being supportive of this endeavor from day one, despite the sacrifices we had to make and trials we had to endure. Without her love and support, I could not have made it through grad school. Her insistence that I find something that I could love doing day in day out has made my life better than I could have done on my own. On top of all of that, she is also

a wonderful mother to our children: Aria, Alyssa, Andrew and Alec. They have all been a constant well of strength and joy that I draw upon every day. Thank you more than I can express.

Table of Contents

List of Figures	viii
1 Introduction	1
1.1 The trapped ion quantum simulator	4
1.2 Outline	6
2 Many-ion Hamiltonian Theory	9
2.1 Single Qubit Manipulation	11
2.2 Mølmer Sørensen	13
2.3 Beyond the Ising Model	21
2.3.1 Undesired Cross-term from TFIM	22
2.3.2 Global σ_z TFIM	24
2.3.3 Generating an X-Y Hamiltonian	29
2.4 Trotterization	31
2.4.1 Phonon Trotterization	33
2.4.2 X-Y Trotterization	35
3 Experimental apparatus	39
3.1 Experimental Overview	39
3.1.1 Trapping Ions	39
3.1.2 Resonant Light	43
3.1.3 Longer Lifetimes	46
3.1.4 Coherent Control	49
3.2 Spontaneous Emission	50
3.2.1 Resonant Light Leakage	51
3.2.2 Off-resonant Spontaneous Emission	53
3.2.2.1 The Two Level System	53
3.2.2.2 Generalization to $^{171}\text{Yb}^+$	54
3.3 State Detection	62
3.3.1 Camera Analysis	65
3.3.2 Detection Correction	69
3.3.3 Independent Component Analysis (ICA)	74

4	Fourth Order Stark Shift	78
4.1	Fourth-order Stark Shift Theory	79
4.2	Experimental Setup	86
4.3	Experimental Demonstration	90
4.4	Applications of the Fourth-order Stark Shift	95
5	Entanglement in Large N System	101
5.1	Spin Squeezing	102
5.2	Quantum Fisher Information	106
5.2.1	Directional QFI	107
5.2.2	Total QFI	108
5.2.3	Measured QFI for 10 spins	111
5.2.4	Measured QFI for 24 spins	115
6	Failures of Quantum Thermalization	118
6.1	Experimental Setup	120
6.2	Observation of Prethermalization	123
6.3	Spin-boson mapping and the GGE	128
6.4	Origin of the double well	131
	Bibliography	133

List of Figures

2.1	Schematic representation of $^{171}\text{Yb}^+$	10
2.2	Phase space evolution of a single ion.	16
2.3	Phase accrued from J_{ij}	19
2.4	Normal mode contributions to J_{ij}	20
2.5	Trottered Spin Phase Phonon Evolution.	34
2.6	Trottered XY Spin Phase Phonon Evolution.	37
3.1	Schematic of trap electrodes.	40
3.2	Picture of UHV chamber on table.	41
3.3	Cycling transition level diagram in $^{171}\text{Yb}^+$	44
3.4	Extended diagram of $^{171}\text{Yb}^+$ energy levels.	47
3.5	Schematic representation of resonant light leakage diagnosis experiments.	51
3.6	$^{171}\text{Yb}^+$ spontaneous emission level diagram.	55
3.7	Probability of a spontaneous emission during a pi pulse as a function of wavelength.	58
3.8	Probability of a single spontaneous emission in N ions.	60
3.9	Measured spontaneous emission rate.	61
3.10	Schematic representation of CCD hardware binning.	64
3.11	Example of camera summed row data.	67
3.12	Example raw ion fidelities using ICCD.	68
3.13	Fast ICA blind source separation.	75
3.14	Basis images from FastICA algorithm.	76
4.1	Schematic representation of the electron energy levels of $^{171}\text{Yb}^+$	81
4.2	Diagram of optics imaging 355nm light onto single ion.	83
4.3	Sketch of a typical raster pulse sequence.	88
4.4	Measured Stark shifts as a function of optical power and position. . .	91
4.5	Resolution of individual addressing beam.	92
4.6	Pulse sequence for preparing a string of 10 ions in a staggered spin configuration.	94
4.7	Fourth-order Stark shift used to generate disorder.	96

4.8	Schematic of individual rotation types.	98
4.9	Measured J_{ij} couplings for 7 and 10 ions.	99
5.1	Measurement of spin squeezing in 24 ions.	105
5.2	Measurement of QFI in 10 Spins.	112
5.3	Measurement of QFI in 24 Spins.	116
6.1	Emergent double well potential	121
6.2	Measured location of spin excitation	123
6.3	Comparison of prethermal data to exact numerics.	125
6.4	Scaling to large system size	127

Chapter 1: Introduction

Ever since Peter Shor introduced his now famous algorithm demonstrating an exponential speed up in factoring large numbers [1], intense interest has been shown in quantum information. Despite the tremendous amount of effort poured into developing a technology capable of implementing Shor's algorithm and others [2–4], fault-tolerant quantum computation remains just out of reach. Even with a multitude of quantum error correction techniques [5], the propensity of quantum systems toward “decoherence” remains the largest obstacle in the way of fault-tolerance.

That is not to say that progress has not occurred. Huge strides have been made in the engineering of quantum systems. Multiple physical implementations exist which have the tools necessary for quantum information [6]: ultra-cold gases [7], silicon quantum dots [8], superconducting circuits [9], and trapped ions [10], to name a few. There are demonstrations of high fidelity single qubit gates [11–13] and two-qubit gates [11, 12, 14] and small scale quantum algorithms are being implemented [15, 16] as the first step towards fault-tolerance. These significant milestones indicate that fault-tolerant quantum computation is close to realization.

While fault-tolerant quantum computation will provide significant speedup

in special problems [4], it will also make efficient simulations of large quantum systems possible [17]. These efficient simulations of quantum systems are critical since a classical simulation of N simple two-level particles requires interference of 2^N complex numbers, unless some approximation is used. To give some notion of what this exponential scaling means, if we wanted to simulate a system of 275 quantum two-level particles, the amount of memory required just to store the state of the whole system would be 7.8×10^{84} bits, assuming a double floating point representation. Estimates of the number of atoms in the known, observable universe range from 10^{78} to 10^{81} , implying that even if every atom in the universe was used as a classical bit of information, we still could not store the state of the system. While there exist cases where approximations can simplify the problem, this is not always possible, especially when large-scale entanglement is involved. A quantum computer, on the other hand, would potentially only need to interfere N qubits, exponentially fewer resources.

What has been described is typically known as a universal quantum computer, yet simulation of a quantum system does not necessitate such a device. As initially proposed by Feynman [18], a quantum simulation only requires a well-controlled quantum system which can implement the evolution of the the desired system. This can also be accomplished by a much simpler device which mimics the evolution in an analog manner [19]. Due to the relative simplicity of an analog quantum simulator, it is much easier to implement in the systems mentioned above and is a way to surpass classical methods without requiring a universal quantum computer.

Thus, quantum simulators stand as a bridge between classical computation

and universal quantum computation, allowing for the computation of very specific problems using the current cutting edge quantum technology. Quantum simulations have been implemented in many different quantum technologies [20–23], leading to a burgeoning field where each technology has specific types of problems that can be explored.

One problem which is of great interest is to find the ground state of a given Hamiltonian. If a quantum device can find the ground state of an arbitrarily connected Hamiltonian in polynomial time, then such a device can be used to solve the class of NP-complete problems [24]. Various techniques have been used to find the ground states of specific Hamiltonians, such as quantum annealing [25, 26] and adiabatic quantum computation [27–30]. The limitation of these techniques is that, in general, exponentially small energy gaps are expected to prevent the global ground state from being found.

Another significant application is to find the dynamics of a given quantum many-body system. Graphene-like physics have been simulated with a level of control not possible in a macroscopic material [31]. Artificial gauge fields in neutral atoms could enable the study of non-trivial topological states and even the simulation of quantum chromodynamics [32]. Observations of an interacting quantum many-body system after a quench have measured the propagation of quantum information throughout the system [33–36]. A uniquely quantum failure of thermalization due to many-body localization has been observed in optical lattices [37–39] and also in trapped ions [40]. Of growing interest is the implementation of long-range interactions, such as in dipolar molecules [41] or the van der Waals interactions in

Rydberg atoms [42–44]. Trapped ions also provide a platform for the study of a long-ranged spin system with the unique ability to tune the range of the interactions [45].

We are at a point in the field where systems are pushing beyond what is classically tractable while maintaining control and measurement of each qubit. In this thesis, I will describe experiments performed on a trapped ion quantum simulator that are on the very edge of surpassing classical techniques, having up to 24 ions used in a classically intractable simulation. This is much larger than what has been previously published of 18 spins [46] and can potentially even be improved in the short term up to ~ 30 spins.

1.1 The trapped ion quantum simulator

My focus in this thesis will be on a linear chain of trapped $^{171}\text{Yb}^+$ used to simulate a many-body quantum spin Hamiltonian. We leverage two hyperfine ground states of the ion which have a stable energy separation as our qubit or spin. Laser beams are used to cool, prepare, and measure these states via resonant transitions and further, apply spin-dependent forces to the ions which couple the spin to the motion. By careful tuning of this spin-dependent force, we can only virtually couple the spin to the motion, allowing the use of the collective motion of the atoms in the trap as a quantum bus. This type of coupling creates a pairwise interaction graph between the spins that falls off with ion separation r as $1/r^\alpha$. The parameter α is continuously tunable over a large domain, namely between long-range couplings,

which fall off slower than $1/r$ (small α), and short-range couplings, which fall off faster than $1/r$ (large α). In addition, we can apply transverse fields in all three directions, implement not only an Ising type Hamiltonian but also an XY Hamiltonian, and now even have independent control of each spin. Measurement of each individual ion is performed using state dependent fluorescence collected with an ICCD camera with high fidelity.

During my stay in the lab, this apparatus was used to study the ground state frustration of an anti-ferromagnetic spin chain as a function of range [28], measure the correlation growth rate for both an Ising and XY Hamiltonian while varying the range across the critical range $1/r$ [34], apply spectroscopic techniques to verify the interaction graph [46], produce a many-body localized state using programmable site-specific disorder [40], and to observe a new form of prethermalization unique to a long-ranged system with open boundaries [47]. What I think is most remarkable is that the control of this system has significantly improved from even 3 years ago where a 16 ion chain was the largest chain possible, to now where 24 spins is regularly used in a classically intractable simulation while still exerting the same level of control found in a system of 10. We think that with only a few minor improvements, performing quantum simulations with 30 spins or more should be possible. This system size regime is exciting as it is the boundary where exact diagonalization is no longer possible and only numeric approximation techniques are applicable. Even these approximations break down for certain classes of problems at > 40 spins. As I write this, my colleagues are trapping ions in a cryogenic apparatus that should be capable of manipulating > 50 spins with the potential to work with as many as 100

ions. Such a system will be more than capable of outperforming classical methods and will represent one of the first steps beyond the limits of the classical computer.

1.2 Outline

The structure of the rest of the thesis is as follows. Chapter 2 is an in depth discussion of how the spins are manipulated and entangled, highlighting especially a careful derivation the interactions and their different regimes. I then discuss the methods developed to expand the types of Hamiltonians applied, especially a technique used to produce a global σ_z field and how it can produce an XY interaction. Finally I discuss some attempts to use trotterization to generate Hamiltonians and ultimately why they didn't work.

Chapter 3 is a very brief overview of the experimental apparatus, as extensive documentation has been done in other theses [48–50]. I also discuss observations about lifetimes in long chains and the current hypothesis of why what we call “de-crystalization”, or the catastrophic loss of the ion crystal, occurs. I then derive the spontaneous emission rate due to our Raman beams and measure the spontaneous emission rate of ten ions to be consistent with the predicted rate. I go on to explain the current technique used to analyze the images from the ICCD camera and the data processing method used to correct known measurement error. Finally, I describe a method of analysis which is scalable to much larger system sizes.

Chapter 4 focuses on the surprisingly large fourth-order Stark shift implemented for individual coherent control. We first lay out the underlying theory for

$^{171}\text{Yb}^+$ with a pulsed laser and then discuss the experimental implementation in our system. We then present the observations of this fourth-order Stark shift and demonstrate its use for state preparation and individual Hamiltonian terms.

Chapter 5 is a review of our work measuring entanglement in a large spin system. We discuss the use of spin-squeezing as a demonstrable witness of genuine multi-partite entanglement and measure it in a system of 24 spins, showing an entanglement depth of 17% of the system. We then examine the quantum Fisher information, which is a witness of genuine multi-partite entanglement assuming a pure state, and measure this witness under the evolution of a quench to an XY Hamiltonian which is a classically intractable problem. First a system of 10 spins is measured and compared to numerics, where the observation is consistent with the entire system fully entangled. This is then scaled up to a system of 24 ions for which numerics are performed by a supercomputer, highlighting the classical computational difficulty. Here again observations are consistent with most of the system, up to 23 out of 24 particle entanglement.

Chapter 6 is an exposition a study of thermalization in closed quantum systems, particularly the failure of thermalization in these systems. Using the tools from previous chapters, we are able to study both the complete failure of thermalization due to many-body localization and also the suppression of thermalization due to quasi-stationary states. I focus on the latter, which is often called prethermalization. Previous observations of prethermal states focused on those described by a generalized Gibbs ensemble, but here we describe and observe a new form prethermalization that is caused by an emergent double-well potential arising from

the long-range interactions and open boundaries of the system, even in the thermodynamic limit. By changing the range of the interaction, we are able to change the system from a prethermal state described by a generalized Gibbs ensemble to this new kind of prethermal state. Finally, we show that this new prethermal state persists even in large system sizes by performing the simulation on 22 spins, one of the largest to date.

Chapter 2: Many-ion Hamiltonian Theory

In the following chapter, I describe the trapped ion system in the abstract and demonstrate the theory required to generate the Hamiltonians used for quantum simulations. I also describe some ideas explored as a means of extending control and also the subtle reasons why some of them failed. While I describe some relevant details here, chapter 3 will explain the experimental realization in greater detail.

The atomic system used throughout is $^{171}\text{Yb}^+$ which is atomic number 70 in the periodic table. This particular element and isotope are desirable since the nucleus is spin-1/2 and is hydrogen-like when ionized. This makes the groundstate manifold have a singlet/triplet structure which has a pair of “clock” states at zero magnetic field. The qubit is encoded in these clock states, namely $^2\text{S}_{1/2} |F = 0, m_f = 0\rangle$ ($|0\rangle$) and $^2\text{S}_{1/2} |F = 1, m_f = 0\rangle$ ($|1\rangle$) separated by the hyperfine frequency ω_{HF} , because they are magnetic field insensitive to first order which makes them ideal qubit states. Additionally, while the resonant transition wavelengths are ultraviolet (UV) at 369 nm, they are not deep UV and can still propagate with minimal losses through air and fibers. A more detailed discussion of the wavelengths used follows in chapter 3.

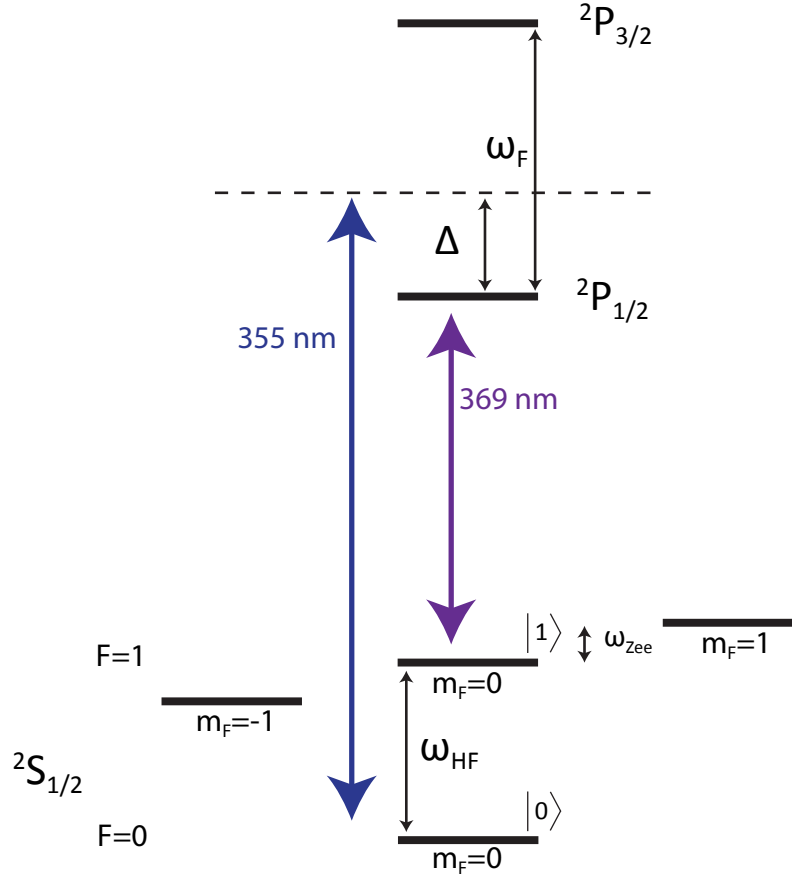


Figure 2.1: Schematic representation of $^{171}\text{Yb}^+$. The qubit is encoded in the ground state hyperfine clock states $|0\rangle \equiv ^2S_{1/2}|F=0, m_f=0\rangle$ and $|1\rangle \equiv ^2S_{1/2}|F=1, m_f=0\rangle$. The resonant transition between the ground state $^2S_{1/2}$ and excited state $^2P_{1/2}$ manifolds is 369 nm. A pulsed laser with center frequency 355 nm is used for stimulated Raman transitions between the qubit states.

2.1 Single Qubit Manipulation

The foundation for any quantum information apparatus is the coherent qubit manipulation. Coherent manipulation is what makes a pair of quantum states into a qubit. Much of the physics described here has been discussed at length elsewhere, but I will give a brief account again to provide a consistent notation later.

All of the coherent qubit operations are implemented using a 355 nm pulsed laser described in more detail in section 3.1.4. Since the laser is pulsed, the optical frequency comb is leveraged to coherently drive the qubits and even entangle them [51]. Despite the fact that stimulated Raman transitions from two far-detuned, non-copropagating laser beams are used for qubit manipulation rather than directly driving the qubit frequency ω_{HF} , the formalism is the same as that of a single beam which has been enumerated in [52] with $\hbar = 1$:

$$\mathcal{H}_I = \frac{\Omega}{2} \sigma_+^j \left(\exp \left[i(\eta(ae^{-i\omega_t t} + a^\dagger e^{i\omega_t t}) - \mu t + \phi) \right] \right) + h.c. \quad (2.1)$$

where Ω is the Rabi frequency, a and a^\dagger are the raising and lowering operators of the harmonic oscillator with frequency ω_t , $\eta = \Delta k x_0$ with Δk the difference of the wavevectors and $x_0 = \sqrt{1/2M\omega_t}$, $\mu = \omega_{HF} - \omega_L$ where ω_L is the difference in optical frequency of the two laser beams and ϕ is the difference in optical phase. By operating in the Lamb-Dicke approximation, $\eta \ll 1$, and the resolved sideband

limit, $\Omega \ll \omega_t$, Eq. 2.1 is approximated as the following:

$$\mathcal{H}_I \approx \frac{\Omega}{2} \sigma_+^j (1 + i\eta(ae^{-i\omega_t t} + a^\dagger e^{i\omega_t t})) e^{-i\mu t + i\phi} + h.c. \quad (2.2)$$

If $\mu = 0$, the phonon terms can be approximated as zero by a rotating wave approximation (RWA), leaving the Hamiltonian:

$$\mathcal{H}_{\text{Carr}} = \frac{\Omega}{2} (\sigma_+^j e^{i\phi} + \sigma_-^j e^{-i\phi}) \quad (2.3)$$

This interaction will flip the spin about an axis that is defined by the phase ϕ . Setting $\phi = 0$ is defined as a rotation around \hat{x} , whereas $\phi = \pi/2$ is a rotation around \hat{y} on the Bloch sphere.

Now if $\mu = -\omega_t$ and RWA is applied to all terms of order ω_t , the Hamiltonian becomes

$$\mathcal{H}_{\text{RSB}} = \eta \frac{\Omega}{2} (a\sigma_+^j e^{i(\phi+\pi/2)} + a^\dagger \sigma_-^j e^{-i(\phi+\pi/2)}) . \quad (2.4)$$

This is the standard Jaynes-Cummings Hamiltonian [53] or also known as a red sideband interaction. If instead $\mu = \omega_t$, the result is the anti-Jaynes-Cummings Hamiltonian or blue sideband interaction, which is

$$\mathcal{H}_{\text{BSB}} = \eta \frac{\Omega}{2} (a^\dagger \sigma_+^j e^{i(\phi+\pi/2)} + a\sigma_-^j e^{-i(\phi+\pi/2)}) . \quad (2.5)$$

2.2 Mølmer Sørensen

In trapped ion quantum information, the Mølmer-Sørensen (M-S) gate is the foundation of all multi-qubit operations. This fundamental entanglement operation has been derived many times before and in different limits. Here I will derive it again, but the context is to clarify different approximations and explain their implications to more sophisticated techniques.

To begin, I assume a standard Mølmer-Sørensen [54, 55] interaction arising from the application of two off-resonant Raman transitions with the beatnote frequencies detuned from both the blue sideband and red sideband. After some algebra, the result is the following Hamiltonian [45]:

$$\mathcal{H}_{MS} = \sum_{m,j=1}^N \eta_{im} \Omega_i \cos[\mu t + \phi_m] \sigma_{\phi_s}^i (a_m e^{-i\omega_m t} + a_m^\dagger e^{i\omega_m t}) \quad (2.6)$$

where the Lamb-Dicke parameter $\eta_{i,m} \equiv b_{i,m} \Delta k / \sqrt{2M\omega_m}$, $b_{i,m}$ is the normal mode transformation matrix element for the i th ion and m th mode, Δk the wave-vector difference of along the trap axis, M the mass of a single $^{171}\text{Yb}^+$, ω_m is the m th normal-mode frequency. Ω_i is the i th ion two-photon Rabi frequency, $\{a_m, a_m^\dagger\}$ are the phonon annihilation and creation operators, and $\sigma_{\phi_s}^i = e^{i\phi_s} \sigma_+^i + e^{-i\phi_s} \sigma_-^i$, where

$$\begin{aligned} \phi_s &= \frac{\phi_r + \phi_b + \pi}{2} \\ \phi_m &= \frac{\phi_r - \phi_b}{2} \end{aligned} \quad (2.7)$$

when $\phi_{r,b}$ are the relative phases of the red and blue sideband beatnotes. Since the

Hamiltonian in Eq. 2.6 is time dependent, the evolution operator requires time-ordering, which can be approximated by the Magnus expansion,

$$U(t) = T \left[e^{-i \int_0^t dt_1 H(t_1)} \right] = e^{\bar{\Omega}_1 + \bar{\Omega}_2 + \bar{\Omega}_3 \dots} \quad (2.8)$$

where T is the time-ordering operator. The first elements of the expansion are

$$\begin{aligned} \bar{\Omega}_1 &= -i \int_0^t dt_1 H(t_1) \\ \bar{\Omega}_2 &= -\frac{1}{2} \int_0^t dt_1 \int_0^{t_1} dt_2 [H(t_1), H(t_2)] \\ \bar{\Omega}_3 &= -\frac{i}{6} \int_0^t dt_1 \int_0^{t_1} dt_2 \int_0^{t_2} dt_3 \left([H(t_1), [H(t_2), H(t_3)]] + [H(t_3), [H(t_2), H(t_1)]] \right). \end{aligned}$$

Calculating $\bar{\Omega}_1$,

$$\bar{\Omega}_1 = - \sum_{i,m} \sigma_{\phi_s}^i (\alpha_{im} a_m^\dagger - \alpha_{im}^* a_m) \quad (2.9)$$

where

$$\alpha_{im} = \frac{i\eta_{im}\Omega_i}{\mu^2 - \omega_m^2} (e^{i\omega_m t} (\mu \sin[\mu t + \phi_m] + i\omega_m \cos[\mu t + \phi_m]) - (\mu \sin[\phi_m] + i\omega_m \cos[\phi_m])).$$

Examining this result, the phonon operator part of $\bar{\Omega}_1$ is exactly the form of a generator of displacement. If α_{im} is large, namely $\eta_{im}\Omega_i$ is large compared to $\mu - \omega_m$, then the spin and motion of the ion will be entangled. Since any measurement of the spin traces over the phonons, when the spin and motion are entangled the observed spin evolution appears incoherent. In fact, the trajectory of the ion in phase space

as a function of time and spin state can be calculated by rewriting $\overline{\Omega}_1$ in terms of the position and momentum operators,

$$\begin{aligned}\overline{\Omega}_1 &= \sum_{i,m} \sigma_{\phi_s}^i \left(\text{Re}[\alpha_{im}](a_m - a_m^\dagger) - i\text{Im}[\alpha_{im}](a_m + a_m^\dagger) \right) \\ &= i \sum_{i,m} \sigma_{\phi_s}^i \left(\text{Re}[\alpha_{im}] X_m \hat{p}_m - \text{Im}[\alpha_{im}] \frac{1}{X_m} \hat{x}_m \right)\end{aligned}\tag{2.10}$$

where $\hat{p}_m = -i \frac{1}{X_m} (a_m - a_m^\dagger)$, $\hat{x}_m = X_m (a_m + a_m^\dagger)$, and $X_m = \frac{1}{\sqrt{2M\omega_m}}$. In Fig. 2.2, two phase space trajectories are shown for a single ion where $\delta = \mu - \omega_m$ has two separate values, $3\eta\Omega$ and $0.3\eta\Omega$. The diameter of the trajectory in phase space is $1/\delta$. A small detuning thus has a larger excursion in phase space, representing greater possible entanglement with the phonons.

Now consider the second term of the expansion, $\overline{\Omega}_2$. The commutator, after doing some algebra, is the following

$$\begin{aligned}[H(t_1), H(t_2)] &= \sum_{i,j,m} \eta_{im} \eta_{jm} \Omega_i \Omega_j \sigma_{\phi_s}^i \sigma_{\phi_s}^j \\ &\quad \cos(\mu t_1 + \phi_m) \cos(\mu t_2 + \phi_m) \left(e^{-i\omega_m(t_1-t_2)} - e^{i\omega_m(t_1-t_2)} \right).\end{aligned}\tag{2.11}$$

Performing the integration and collecting terms is a chore, but fairly straightforward.

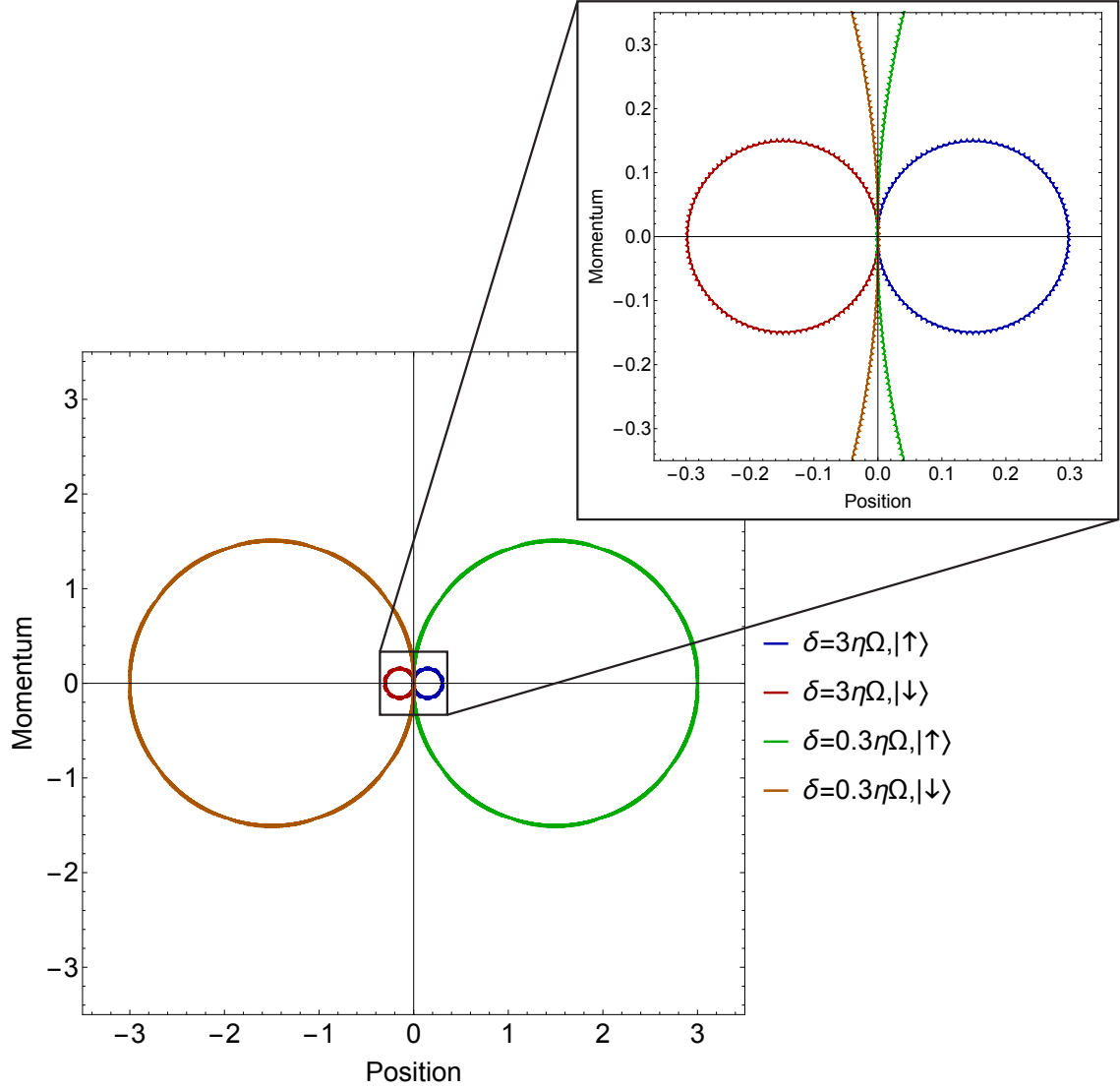


Figure 2.2: Phase space evolution of a single ion. Plots of spin phase space trajectories for two separate detunings, $\delta = 3\eta\Omega$ and $\delta = 0.3\eta\Omega$ where $X_m \equiv 1$ in the rotating frame of trap frequency. The radius of the trajectory is $\propto \frac{1}{\delta}$. A non-zero final value for \hat{x} and \hat{p} represents entanglement with the motion, with larger numbers implying greater entanglement.

The final result is

$$\begin{aligned}
\bar{\Omega}_2 = & \sum_{i,j,m} \sigma_{\phi_s}^i \sigma_{\phi_s}^j \frac{i\eta_{im}\eta_{jm}\Omega_i\Omega_j}{\mu^2 - \omega_m^2} \left[-\omega_m t + \frac{\omega_m}{2\mu} \sin(2\phi_m) - \frac{\omega_m}{2\mu} \sin(2(\mu t + \phi_m)) \right. \\
& + \mu \sin(\phi_m) \left(\frac{\cos((\mu + \omega_m)t + \phi_m)}{\mu + \omega_m} - \frac{\cos((\mu - \omega_m)t + \phi_m)}{\mu - \omega_m} \right) \\
& \left. + \omega_m \cos(\phi_m) \left(\frac{\sin((\mu + \omega_m)t + \phi_m)}{\mu + \omega_m} + \frac{\sin((\mu - \omega_m)t + \phi_m)}{\mu - \omega_m} \right) \right] \\
= & i \left(\sum_{i,j} J_{ij} \sigma_{\phi_s}^i \sigma_{\phi_s}^j \right) t
\end{aligned} \tag{2.12}$$

Finally, the higher order terms of the Magnus expansion are all identically zero since all terms commute. This allows the time evolution operator to be expressed as

$$U(t) = e^{\bar{\Omega}_1 + \bar{\Omega}_2}. \tag{2.13}$$

Ultimately, quantum information needs the time evolution operator in Eq. 2.13 to be just the spin-spin operator in the final line of Eq. 2.12, requiring $\bar{\Omega}_1 \Rightarrow 0$. This can be accomplished in two different ways, resulting in two distinct regimes.

The first case is where $\delta = \mu - \omega_m$ is the roughly the same or smaller than $\eta\Omega$. In this “fast gate” regime, the requirement that $\alpha_{jm}(t) = 0$ is fulfilled by finding times t such that all α_{jm} are zero. This becomes difficult with more modes and ions, unless one of the parameters is modulated to adjust the phase space evolution of these motional modes. A very fruitful method is to change Ω_i and the phase ϕ_s [56, 57], which has now been used to perform arbitrary gates in a small chain of 5 ions [16].

In the second case, or the “slow gate” regime, δ is much greater than $\eta\Omega$,

therefore $\overline{\Omega}_1 \approx 0$. The expression for J_{ij} can also be simplified by discarding all terms bounded in time since δ is very large. The only remaining term is the first in Eq. 2.12 which is linear in time. Thus, under the slow gate approximation, the time evolution operator becomes,

$$\begin{aligned}
U(t) &= \exp \left(-i \sum_{i,j,m} \frac{\eta_{im} \eta_{jm} \Omega_i \Omega_j}{\mu^2 - \omega_m^2} \omega_m \sigma_{\phi_s}^i \sigma_{\phi_s}^j t \right) \\
U(t) &= \exp \left(-i \sum_{i,j,m} J_{ij} \sigma_{\phi_s}^i \sigma_{\phi_s}^j t \right)
\end{aligned} \tag{2.14}$$

From this expression, the effective Hamiltonian is

$$\mathcal{H}_{eff} = \sum_{i,j,m} J_{ij} \sigma_{\phi_s}^i \sigma_{\phi_s}^j \tag{2.15}$$

This is the foundational Hamiltonian for all trapped ion quantum simulations. Relating this back to the fast-gate regime, the evolution of the modes in phase space can be envisioned as being very small circles cycling very quickly. Since the spin-spin interaction stems from a difference in phase between spin up and spin down and even though the resulting circles in phase space are very small, there is a huge number of them, producing a large phase difference and generating the effective spin-spin coupling. Another picture is that because the interaction arises from virtual coupling to phonons and no actual phonons are produced, the spins are only virtually entangled with the motion while still generating a spin-spin interaction.

On a practical note, while a larger detuning is better for suppression of the spin-motion entanglement, it also simultaneously suppresses J_{ij} . Experience has

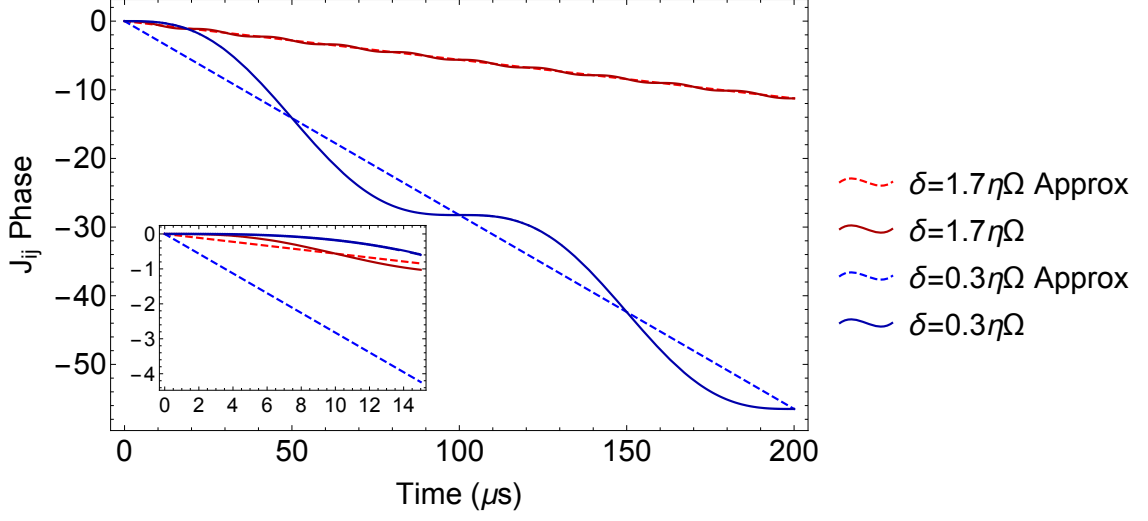


Figure 2.3: Phase accrued from J_{ij} . Plots of the accrued phase from J_{ij} for two separate detunings, $\delta = 1.7\eta\Omega$ and $\delta = 0.3\eta\Omega$. Dashed lines are slow gate approximation of the accumulated phase. Note that for short times and small detunings (shown in inset) the approximation breaks down and very little phase is accrued.

shown that the optimal detuning for the slow gate is around $3\eta\Omega$, giving reasonable J_{ij} with minimal residual spin-motion entanglement.

Since the way the two regimes are produced changes from essentially a gate model to a time evolution model, it is often hard to connect the dots between them. One easy way to envision the different regimes is to examine the accrual of phase as a function of time for the full expression of J_{ij} for different detunings. An illustration is shown in Fig. 2.3 where the accrued phase due to J_{ij} is shown for two separate detunings with the corresponding slow gate approximation. Clearly the approximation is good when δ is large, but does not work in the case of small δ at short times. This becomes important when trying to perform dynamics at times that are much smaller than $1/\delta$, as the slow-gate approximation that J_{ij} has a purely linear dependance on time is no longer valid.

One final observation has to do with the structure of J_{ij} itself. The coupling

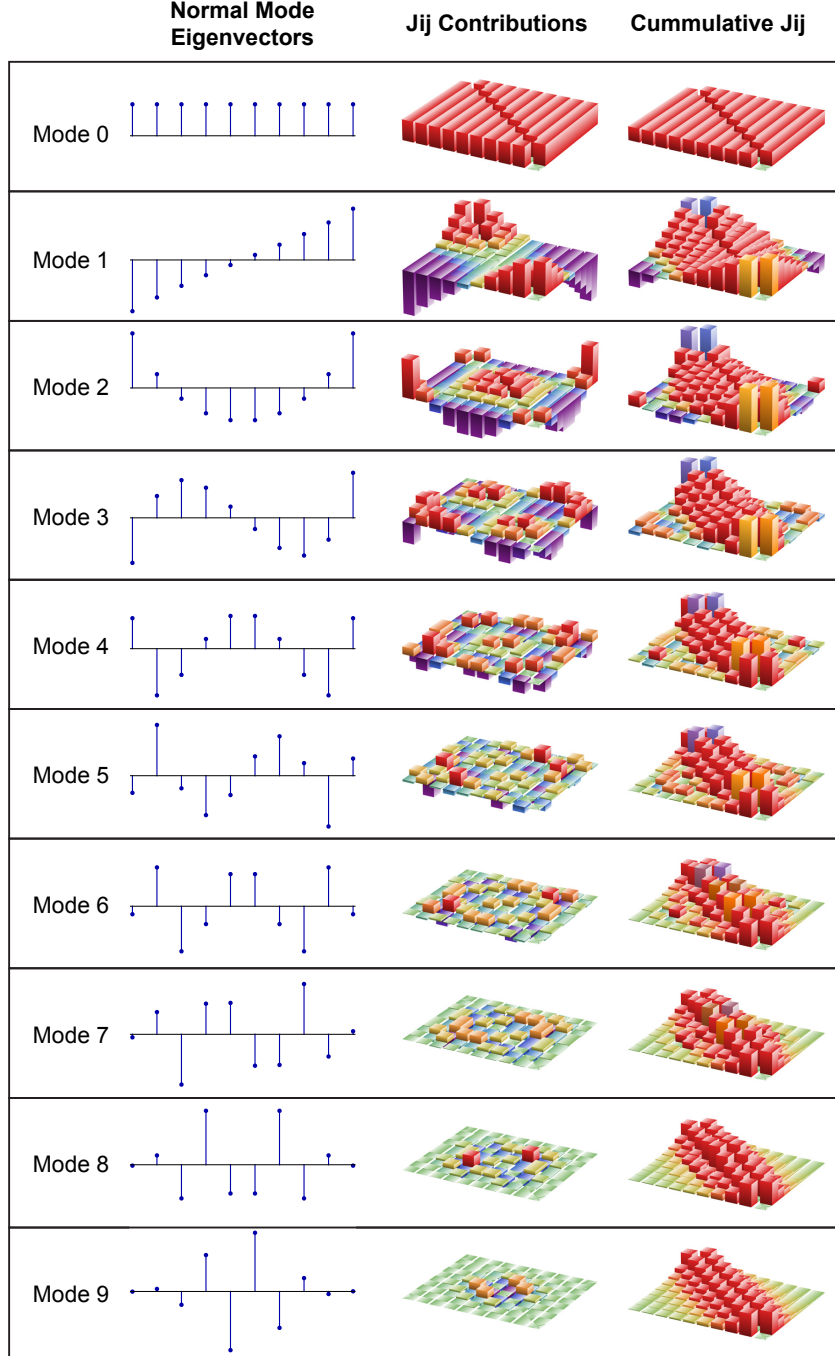


Figure 2.4: Normal mode contributions to J_{ij} . Plot of the normal mode eigenvectors for an axial trap frequency of 0.5 MHz and radial trap frequency of 5 MHz. Mode 0 corresponds to the center-of-mass mode and mode 9 to the zig-zag mode for a chain of ten spins. In order to visualize the contribution of each mode to the coupling matrix, the J_{ij} matrix contribution from each mode, ignoring the rest, with a detuning of $\delta = 3\eta\Omega$ from the center-of-mass mode is shown. Also shown is the resultant coupling matrix from a cumulative sum of the contributions. The final coupling matrix has an effective range of $\alpha = 1.2$.

matrix is fundamentally long-ranged, which is typically parametrized as $J_{ij} \sim J_0/|i-j|^\alpha$ where $|i-j|$ is the distance between spins i and j and α in theory ranges from 0 to 3, but in practice from about 0.5 to 1.8. The reason the interaction is long-ranged is due to the use of the normal modes of motion as our quantum information channel. The parameter α is varied by changing the strength of the coupling to each mode, either by modifying the detuning or by adjusting the mode dispersion using the axial trap frequency. An example of a short-range interaction is depicted in Fig. 2.4 showing how each mode contributes to the coupling matrix, giving the resulting interaction graph.

2.3 Beyond the Ising Model

The easiest way to extend the simulation beyond that of a long-range Ising model is to simply add a global transverse field. This can be accomplished by applying a carrier that is 90 deg out of phase with the interaction, as seen from Eq. 2.3. Yet, adding a transverse field has other implications when incorporated into the derivation of the effective Hamiltonian discussed above. Earlier, the third order and higher terms of the Magnus expansion vanished since the commutators were zero. With a transverse field, not only will the series no longer converge, but there will also be an additional term in the second order of the expansion which grows linearly with time. Below is a brief derivation to gain some insight into the size of this lowest order unwanted term and also what can be done to mitigate it.

2.3.1 Undesired Cross-term from TFIM

Fixing the phase of Eq. 2.6 to $\phi_s = \pi$ and $\phi_m = -\pi/2$ and also adding a carrier term along \hat{y} results in the following time-dependent Hamiltonian, \mathcal{H}_{TrF} :

$$\begin{aligned}\mathcal{H}_{MS} &= \sum_{m,j=1}^N \eta_{i,m} \Omega_i \sin[\mu t] (-\sigma_x^j) (a_m e^{-i\omega_m t} + a_m^\dagger e^{i\omega_m t}) \\ \mathcal{H}_C &= \frac{\Omega_C}{2} \sum_j \sigma_y^j\end{aligned}\tag{2.16}$$

$$\mathcal{H}_{TrF} = \mathcal{H}_{MS} + \mathcal{H}_C.$$

When this Hamiltonian is substituted into the Magnus expansion, an additional term in $\bar{\Omega}_1$ arises, namely $-i \left(\frac{\Omega_C}{2} \sum_i \sigma_y^i \right) t$, which gives the desired transverse field applied. There is also an unwanted term, \mathcal{H}_X , in $\bar{\Omega}_2$ which comes from the spin commutators. The size of \mathcal{H}_X can be estimated by starting with the observation,

$$\begin{aligned}[\mathcal{H}_{TrF}(t_1), \mathcal{H}_{TrF}(t_2)] &= [\mathcal{H}_{MS}(t_1), \mathcal{H}_{MS}(t_2)] + [\mathcal{H}_{MS}(t_1), \mathcal{H}_C(t_2)] \\ &\quad + [\mathcal{H}_C(t_1), \mathcal{H}_{MS}(t_2)] + [\mathcal{H}_C(t_1), \mathcal{H}_C(t_2)].\end{aligned}\tag{2.17}$$

The first commutator gives the same result as Eq. 2.12. The last commutator is identically zero since \mathcal{H}_C is time independent. The remaining two commutators result in an undesired cross-term, namely

$$\mathcal{H}_X = -\frac{1}{2} \int_0^t dt_1 \int_0^{t_1} dt_2 [\mathcal{H}_{MS}(t_1), \mathcal{H}_C(t_2)] + [\mathcal{H}_C(t_1), \mathcal{H}_{MS}(t_2)]\tag{2.18}$$

In order to make the algebra easier, a single mode is considered and it is assumed that $\delta \gg \eta\Omega$, discarding all terms which have dynamics faster than δ . Thus \mathcal{H}_{MS} becomes simply

$$\mathcal{H}_{MS} = \sum_{i=1}^N \frac{i\eta_i\Omega_i}{2} \sigma_x^i (ae^{i\delta t} + a^\dagger e^{-i\delta t}) \quad (2.19)$$

After doing the commutation and integration and performing a RWA to discard all non-stationary terms,

$$\mathcal{H}_X = \frac{\eta_i\Omega_i\Omega_C}{4\delta} \sigma_x^i \left(\frac{2}{\delta}(a - a^\dagger) + it(a + a^\dagger) \right) \quad (2.20)$$

Of course at times where $t \gg 1/\delta$, the only significant term is the second:

$$\mathcal{H}_X = i \left(\frac{\eta_i\Omega_i\Omega_C}{4\delta} \sigma_x^i (a + a^\dagger) \right) t \quad (2.21)$$

In order for \mathcal{H}_X to be negligible, J_{ij} must fulfill the inequality $J_{ij} \gg \frac{\eta_i\Omega_i\Omega_C}{4\delta}$ which implies that $2\eta\Omega_i \gg \Omega_C$. In practice, if $\eta\Omega \sim 30$ kHz, $\Omega_C \leq 20$ kHz is sufficiently small.

Since this is only the second order term and the series continues indefinitely, it is very likely that the higher order terms have some contribution to the dynamics. Experimental evidence suggests that these higher order terms might destructively interfere with the second order terms since the effect of this unwanted cross-term is observed to be smaller than expected. Even so, Eq. 2.21 still gives a reasonable regime where \mathcal{H}_X can be neglected, and thus the final effective Hamiltonian can be

written

$$\mathcal{H}_{eff} = \sum J_{ij} \sigma_x^i \sigma_x^j + \frac{\Omega_C}{2} \sum_i \sigma_y^i \quad (2.22)$$

which is a long-ranged transverse field Ising model (TFIM).

2.3.2 Global σ_z TFIM

Up until the last few years, the effective Hamiltonians simulated have been limited to an Ising Hamiltonian with either a transverse field along \hat{y} [28, 45] or an additional longitudinal field [29]. The following will be a discussion of techniques used to extend the types of Hamiltonians applied.

The first technique described will be a way to generate a significant global σ_z in the system without the need to modulate the qubit frequency, since this is difficult to do in a clock-state qubit [58]. The method itself is fairly simple. While driving a M-S interaction, instead of having a symmetric detuning of $\pm\mu$, instead an asymmetric detuning of $\omega_{HF} - \mu - D$ and $\omega_{HF} + \mu - D$ is used. As long as D is small compared to δ ($\delta = \mu - \omega_{CM}$ where ω_{CM} is the center of mass frequency), then this will result in an effective field $\mathcal{H}_z = \frac{D}{2} \sum_i \hat{\sigma}_z^i$. Intuitively, one can understand this by viewing the system from the frame defined by fixing the two sideband frequencies in absolute frequency. In this frame of reference, if a field $B_z \sigma_z$ was applied to the system, relative to the sidebands, it would appear that the qubit frequency had changed by $2B_z$. This technique simply inverts the effect and generates a B_z field by shifting the sideband detunings up or down in frequency by D , exactly as if a σ_z field is applied.

A proper account of this technique requires that a step back from the starting point of Eq. 2.1. Much like Eq. 2.1, the formalism will assume single beams for brevity but can easily be extended to the stimulated Raman transitions used in the experiment. Also assumed is that the only states coupled by the laser are the qubit states and all other states can be neglected, namely the system can be reduced to a two level system. Further, only one of the normal modes of motion is considered and then generalized to many after.

Assuming a system of N qubits which have a splitting of ω_{HF} with normal mode frequency of ω_m , the base atomic Hamiltonian is

$$\mathcal{H}_0 = \sum_i \frac{\omega_{HF}}{2} \sigma_z^i + \omega_m \hat{a}_m^\dagger \hat{a}_m. \quad (2.23)$$

Now if two lasers with frequencies $\omega_R \equiv \omega_{HF} - \omega_m - \delta_R$ and $\omega_B \equiv \omega_{HF} + \omega_m + \delta_B$ with the same intensity are applied, the result is the following:

$$\mathcal{H} = \sum_i \frac{\omega_{HF}}{2} \sigma_z^i + \omega_m \hat{a}_m^\dagger \hat{a}_m + \frac{\Omega}{2} \sigma_+^i e^{i(\mathbf{k} \cdot \mathbf{r} - \omega_R t)} + \frac{\Omega}{2} \sigma_+^i e^{i(\mathbf{k} \cdot \mathbf{r} - \omega_B t)} + h.c. \quad (2.24)$$

Applying the the Lamb-Dicke and resolved sideband approximations, typically the rotating frame $H_0 = \frac{\omega_{HF}}{2} \sigma_z^i + \omega_m \hat{a}_m^\dagger \hat{a}_m$ is used which, after an RWA, results in

$$\mathcal{H} = \sum_i \frac{i\eta\Omega}{2} (\sigma_+^i \hat{a} e^{i\delta_R t} - \sigma_-^i \hat{a}^\dagger e^{-i\delta_R t} + \sigma_+^i \hat{a}^\dagger e^{-i\delta_B t} - \sigma_-^i \hat{a} e^{i\delta_B t}) \quad (2.25)$$

where ω_R and ω_B have been substituted. If now $\delta_R = \delta_B = \delta$, a standard M-S

Hamiltonian is recovered (see Eq. 2.19).

Instead of using the rotating frame mentioned above, now let the rotating frame be defined $H_0 = \frac{\omega_{HF}-D}{2}\sigma_z^i + \omega_m \hat{a}_m^\dagger \hat{a}_m$. Using the same approximations as Eq. 2.25, the result is the following Hamiltonian:

$$\begin{aligned} \mathcal{H} = \sum_i \frac{D}{2} \sigma_z^i + \frac{i\eta\Omega}{2} & \left(\sigma_+^i \hat{a} e^{i(\delta_R-D)t} - \sigma_-^i \hat{a}^\dagger e^{-i(\delta_R-D)t} \right. \\ & \left. + \sigma_+^i \hat{a}^\dagger e^{-i(\delta_B+D)t} - \sigma_-^i \hat{a} e^{i(\delta_B+D)t} \right) \end{aligned} \quad (2.26)$$

Now the reason behind asymmetrically changing the detunings becomes clear, since by setting $\delta_R = \delta + D$ and $\delta_B = \delta - D$ and substituting into Eq. 2.26 and assuming that $D \ll \delta$, the result becomes

$$\mathcal{H} = \sum_i \frac{D}{2} \sigma_z^i + \frac{i\eta\Omega}{2} \left(\sigma_+^i \hat{a} e^{i\delta t} - \sigma_-^i \hat{a}^\dagger e^{-i\delta t} + \sigma_+^i \hat{a}^\dagger e^{-i\delta t} - \sigma_-^i \hat{a} e^{i\delta t} \right). \quad (2.27)$$

The resulting Eq. 2.27 is nearly identical to Eq. 2.25 except now there is a global σ_z field in addition. Reincorporating all of the motional modes, Eq. 2.27 is rewritten in the same form as Eq. 2.6 but has an additional global σ_z field. Just as discussed in section 2.3.1, this transverse field will also generate cross-terms in the Magnus expansion, adding a further restriction that $D/2 \ll \eta\Omega$. When D fulfills the specified limits, the effective Hamiltonian becomes:

$$\mathcal{H}_{eff} = \sum J_{ij} \sigma_x^i \sigma_x^j + \sum_i \frac{D}{2} \sigma_z^i \quad (2.28)$$

It should be noted here that this is a case where the rotating frame that

is chosen is not a “natural” frame. This technique doesn’t actually change the hyperfine frequency, but moves the system into a frame where the qubit frequency is different by exactly D , making the dynamics in this frame the same as a system with the coupling matrix and a transverse field. Interestingly, this means that all operations on the qubit, such as rotations around \hat{x} and \hat{y} on the Bloch sphere now occur with the imposed new qubit frequency. In the lab, this means that while normally the beat-note of the lasers is exactly ω_{HF} in order to rotate the qubit, now the beat-note has to be modified to $\omega_{HF} - D$ in order to perform these rotations.

There are even more profound implications to this technique since any time that is spent without the application of the asymmetric detunings is no longer unitary evolution from the perspective of the effective qubit! In fact, from the perspective of this imposed frame, what used to be unitary evolution is now the same as a $\hat{\sigma}_z$ field with strength $D/2$. This is relevant when trying to incorporate state preparation into the experiment since this generally takes a non-negligible amount of time prior to the application of the interaction. If there is a delay for some time τ prior to the interaction, the phase of the rotating frame J_{ij} , namely ϕ_s (see Eq. 2.7), has to be advanced by $D\tau$ so that a $\sigma_x\sigma_x$ interaction matches up with the effective qubit \hat{x} axis and similarly for \hat{y} . This is equivalent to performing a rotation around \hat{z} exactly equal and opposite the rotation that occurred during the delay. If this is not done, then ϕ_s is no longer what was specified experimentally and the observed dynamics will be incorrect. Since $\phi_s = (\phi_R + \phi_B + \pi)/2$, in order to advance ϕ_s by $D\tau$, both ϕ_R and ϕ_B must increase by $D\tau$ or just one of them must increase by $2D\tau$.

Similar arguments also apply to the analysis rotations which occur at the end of the experiment where now the normal rotations around \hat{x} or \hat{y} with qubit frequency $\omega_{HF} - D$ also have to take into account the shifted phase from any delay for time τ . In other words, the phase of the rotation ϕ_{rot} must be the same as the total phase of the system ϕ_{tot} . In order for the final rotation to be coherent with the qubit, time is tracked from the beginning of the experiment, namely for total time T . Thus the phase of the rotation is $\phi_{rot} = \omega_R T + \phi$ where ω_R is the rotation frequency and ϕ is an additional phase control. Now ϕ_{tot} takes into account the evolution under each rotating frame, where if there is some delay for time τ , then $\phi_{tot} = \omega_{HF}\tau + (\omega_{HF} - D)(T - \tau)$. Phase coherence requires that $\phi_{rot} = \phi_{tot}$. Since there are two control parameters, there are two possible solutions. One possible solution is to set $\omega_R = \omega_{HF} - D$ and solve for ϕ :

$$\begin{aligned}\phi_{rot} &= \phi_{tot} \\ (\omega_{HF} - D)T + \phi &= \omega_{HF}\tau + (\omega_{HF} - D)(T - \tau) \\ \phi &= D\tau\end{aligned}\tag{2.29}$$

which is identical to what was discussed in regards to the J_{ij} phase above. Clearly when τ goes to zero, then this is just the same as performing the rotation with the

imposed frequency. The other solution is to set $\phi = 0$ and let $\omega_R = \omega_{HF} + D'$:

$$\begin{aligned}
\phi_{rot} &= \phi_{tot} \\
(\omega_{HF} - D')T &= \omega_{HF}\tau + (\omega_{HF} - D)(T - \tau) \\
D'T &= D(T - \tau) \\
D' &= D(1 - \frac{\tau}{T}).
\end{aligned}
\tag{2.30}$$

Both possibilities are equivalent to performing a rotation of $D\tau$ around the \hat{z} axis. These other methods are only possible because the difference between \hat{x} and \hat{y} is just the phase of the laser beat-note as compared to the laser phase at the $t = 0$. This makes the \hat{z} axis special since rotations can be replaced by manipulation of the phase or frequency, over which experimental control is very good, versus performing a rotation the lasers, which has less control due to small intensity fluctuations.

One final note is that the discussion of rotations is particularly relevant for measurement of the \hat{x} and \hat{y} spin projections in the lab frame, yet there are no rotations required to measure the \hat{z} projections in the lab frame. This is simply due to the fact that the observable commutes with the rotating operator and thus $\langle \sigma_z \rangle$ is the same in both the lab frame and the rotating frame.

2.3.3 Generating an X-Y Hamiltonian

Here I describe an extension to a technique which produces an effective X-Y Hamiltonian shown previously [34, 50]. What is novel here is the incorporation of the transverse field in \hat{z} discussed above. Begin with the final effective Hamiltonian

described in Eq. 2.28 and now assume that $D/2 \gg J_{ij}$. By rewriting $\sigma_x^i \sigma_x^j$ in terms of the raising and lowering operators,

$$\mathcal{H}_{eff} = \sum J_{ij} (\sigma_+^i \sigma_+^j + \sigma_+^i \sigma_-^j + \sigma_-^i \sigma_+^j + \sigma_-^i \sigma_-^j) + \sum_i \frac{D}{2} \sigma_z^i. \quad (2.31)$$

If now the rotating frame of $\sum_i \frac{D}{2} \sigma_z^i$ is applied, then $\sigma_\pm^i \rightarrow \sigma_\pm^i e^{\pm i D/2 t}$ resulting in Eq. 2.31 becoming

$$\mathcal{H}_{eff} = \sum J_{ij} (\sigma_+^i \sigma_+^j e^{i D t} + \sigma_+^i \sigma_-^j + \sigma_-^i \sigma_+^j + \sigma_-^i \sigma_-^j e^{-i D t}). \quad (2.32)$$

Since $D/2 \gg J_{ij}$, a RW approximation of Eq. 2.32 discards both double spin-flip terms and leaves just the spin exchange terms, which is an X-Y Hamiltonian:

$$\mathcal{H}_{eff} \approx \sum \frac{J_{ij}}{2} (\sigma_x^i \sigma_x^j + \sigma_y^i \sigma_y^j). \quad (2.33)$$

While this result is, up to a basis rotation, the same as has been previously shown, there are unique advantages to using a transverse field in \hat{z} . The first is that the strength of the field is determined by a change in beat-note frequency, which is ultimately tied to the precision and stability of an RF source. Since these RF sources are experimentally well controlled, the stability of this field is ultimately limited by the noise on the qubit itself, which for a clock-state qubit is very small. This stability makes the above approximation good out to very long times when typical noise sources are become significant.

There is an additional experimentally relevant advantage, namely that the

rotations required to map the rotating frame back into the lab frame can be replaced by the techniques described in section 2.3.2. In fact, the rotating frame described in Eq. 2.32 is exactly equal and opposite the frame used to produce the effective σ_z field. This means that by keeping the laser beat-note at exactly ω_{HF} for all analysis rotations, the dynamics observed are described by Eq. 2.33 for all times. Experimentally, this is very powerful since no calibration is required to map the rotating frame back to the lab frame. Whereas if the transverse field is a laser driven carrier, the calibration of the field strength is critical to the mapping back to the lab frame and introduces noise at long times. Further, the laser driven carrier requires measurements at only times of $n2\pi/B$ [34], restricting the observation of the dynamics to discrete time periods.

The technique above provides an experimentally easy method of realizing an X-Y Hamiltonian for all times, making simulations of this type of system simple to implement even at long times. This has greatly expanded the types of simulations which can be performed and provided a unique ability to fundamentally change the simulated Hamiltonian.

2.4 Trotterization

Another technique explored for further expanding simulations was trotterization [17, 59]. An experimental demonstration of this technique has already been realized in a trapped ion apparatus [60], but trotterization was revisited for two purposes. The first was to enable extremely close detunings to motional modes while

still having negligible phonon population. The second was to have an exact X-Y Hamiltonian without the technique explained in section 2.3.3, which by combining the techniques would enable the production of a Heisenberg model.

The statement of trotterization is, that while for non-commuting operators A and B , $e^{A+B} \neq e^A e^B$, the following statement is true:

$$\mathcal{U}(t) = \lim_{n \rightarrow \infty} e^{i\mathcal{H}t} = \left(e^{iH_1 t/n} e^{iH_2 t/n} \dots e^{iH_\xi t/n} \right)^n \quad (2.34)$$

where $\mathcal{H} = H_1 + H_2 + \dots + H_\xi$ and $\{H_1, H_2, \dots, H_\xi\}$ are a set of non-commuting operators. Thus if n is chosen to be some large, but finite integer then

$$\mathcal{U}(t) = \left(e^{iH_1 t/n} e^{iH_2 t/n} \dots e^{iH_\xi t/n} \right)^n + \sum_{i < j} [H_i, H_j] \frac{t^2}{2n} + \sum_{k=3}^{\infty} E(k) \quad (2.35)$$

where $E(k)$ is bounded by $\|E(k)\|_{sup} \leq n \|\mathcal{H}t/n\|_{sup}^k / k!$. From this expression, $E(k) \sim (t/n)^k$ when $k \geq 3$. If $n > 1$, then the sum over k in Eq. 2.35 will be smaller than the second term which is only linearly dependent on n . Thus the dominant source of error will be the second-order term, $\sum_{i < j} [H_i, H_j] \frac{t^2}{2n}$.

This implies that to achieve any specified accuracy of the simulation of $1 - \epsilon$, where $\epsilon > 0$, then it is required that $n \propto t^2/\epsilon$. Whereas, solving for ϵ and allowing n to change but fixing the total time t ,

$$\epsilon \sim t^2/n = (\Delta t)t \quad (2.36)$$

where $\Delta t = t/n$ is the time of each trotter step. The error ϵ decreases linearly

with decreasing Δt , but increases linearly with the total time of the simulation. Essentially, for a fixed experimental time, the faster the trotterization, the better the trotter error. As will be shown, other factors can limit the trotter step size or even prohibit the use of trotterization entirely.

2.4.1 Phonon Trotterization

One of the first applications of trotterization stemmed from an observation that the first term of the Magnus expansion, $\overline{\Omega}_1$, is linear in $\sigma_{\phi_s}^i$ while the interaction term is quadratic. By alternating the sign of $\sigma_{\phi_s}^i$, it was supposed that any phonon evolution would immediately be canceled by phonon evolution with opposite sign. Trotterizing in this way would allow for detunings much closer to the motional modes, enabling larger J_{ij} and better control over which modes are contributing to the coupling matrix. This intuitive picture turned out to be a naive understanding of the problem. There are two issues which were not taken into account which make this application not practical.

The first issue has already been discussed and illustrated in Fig. 2.3, namely that for a small detuning δ from a particular motional mode, that mode's sinusoidal terms of J_{ij} become large and cannot be ignored at times smaller than $1/\delta$. This implies that the trotter time must be much larger than $1/\delta$, restricting how quickly the interaction can be trottered. By itself, this fact did not prohibit the technique since it could still be used to tune closer to the motional modes.

The second issue ends up being more important than the first. To compensate

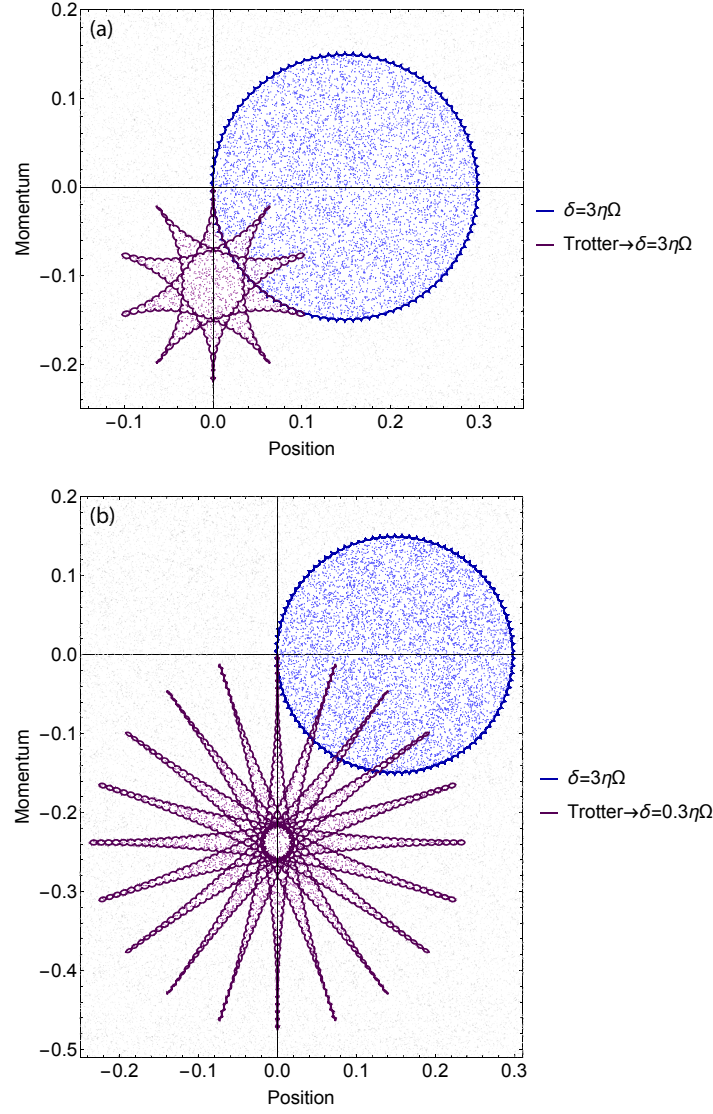


Figure 2.5: Trottered Spin Phase Phonon Evolution. Comparison of the continuous evolution to a trottered spin phase with same detuning (a). While the phonon population stays small, the area enclosed in phase space, which is directly related to the accrued J_{ij} phase, is smaller in the trottered evolution than in the continuous evolution. The total phase accrued by the continuous evolution is 5 times greater than the trottered evolution. This was measured by comparing the number of randomly distributed points in each shape. A similar comparison is shown (b) when the trottered evolution has a detuning ten times smaller than the continuous evolution. While the phonon population stays small due to the trottered phase, the enclosed area is still 1.6 times smaller than the continuous evolution. This demonstrates that it is better to just decrease $\eta\Omega$ than to trotter the spin phase.

for the first issue, let the trotter step time $\Delta t > 1/\delta$. Then evolution through phase space for the mode with the smallest detuning is no longer small circles, but star like shapes. From the discussion of the M-S gate, generating a spin-spin interaction is derived from a difference of phase accrued by spin-up and spin-down and so the size of J_{ij} is directly related to the amount of phase space enclosed by the loops in phase space. In Fig. 2.5, the loop in phase space from a continuous evolution is directly compared to the trotter spin phase evolution with the same detunings. Since analytically computing the area of the arbitrary shapes is fairly difficult, instead a uniform random distribution of points is created across the relevant area of phase space and then the number of points within the shapes in question is counted, giving a rough quantitative comparison of area. For the same detuning $\delta = 3\eta\Omega$, the continuous evolution is $\sim 5\times$ larger than the trottered evolution. This is when the detunings are the same, but even decreasing the trottered detuning to $\delta = 0.3\eta\Omega$, the continuous evolution area is still larger by a factor of $\sim 1.6\times$. This implies that it would be better to decrease $\eta\Omega$ by a factor of 10 and tune closer than to trotterize the spin phase. Since it is more efficient to decrease $\eta\Omega$, there is no reason to complicate matters by trotterizing.

2.4.2 X-Y Trotterization

The other proposed application centered around an issue that was mentioned above, namely that a large transverse field produces undesired cross terms, even when they are small. At long times, these cross-terms become more relevant and

are also phonon dependent. By trottering between a $\sigma_x\sigma_x$ interaction and a $\sigma_y\sigma_y$ interaction, it was hypothesized that an X-Y Hamiltonian could be produced without the cross-term or the need for rotating frames. This hypothesis was further strengthened by the fact that an X-Y Hamiltonian had already been demonstrated in a two-spin trapped ion qubit system using trotterization [60].

Again, the issues are more subtle than they first appear and ultimately can only be understood in the context of the phase space picture for the motional modes. Here the proposed experiment is to apply two separate M-S interactions, the first with $\phi_s = \pi$ and the second $\phi_s = \pi/2$, effectively trottering between a $\sigma_x\sigma_x$ interaction and a $\sigma_y\sigma_y$ interaction. In the phase space picture, when ϕ_s is changed by $\pi/2$, $|\uparrow\rangle_x \rightarrow \frac{1}{\sqrt{2}}(|\uparrow\rangle_y + |\downarrow\rangle_y)$ and similarly for $|\downarrow\rangle_x$. Thus the motional population splits, half the population maintaining the original sign and the other half swapping sign. Because of this sign swap, the trotter time compared to $1/2\delta$ becomes extremely important. If the trotter time is not $1/2\delta$, then the phonon population stays small and the trotterization works as expected. This can be seen in Fig. 2.6a, where the trottered phonon population stays localized close to zero when the trotter time $\tau_{XY} = .675/\delta$. The worst case scenario is shown in Fig. 2.6b, where the trotter time is half $1/\delta$. In this case, there is some phonon population that grows linearly with time. Each time the population splits, there are two paths in phase space. What is computed here is only one path but it is the largest. This puts limits on the possible size of the phonon population, but the reality is that the population fills the area enclosed by this trajectory, which in this worst case scenario is a huge amount of phase space. While the population going out to infinity decays exponentially with

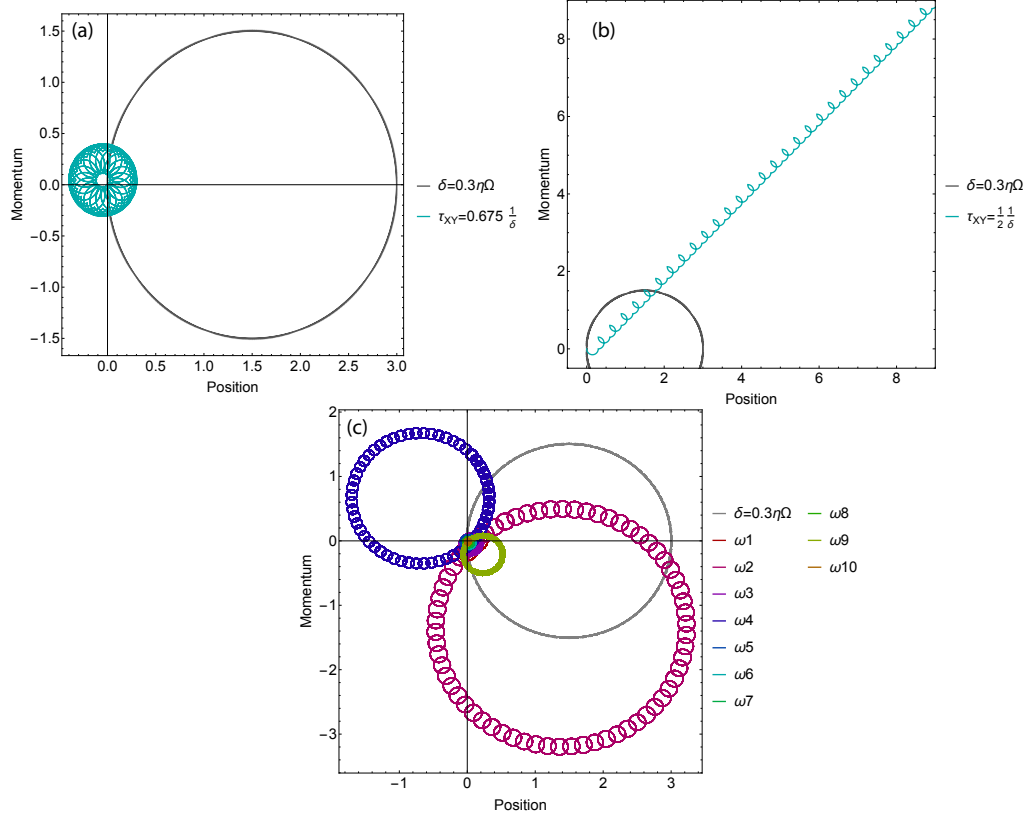


Figure 2.6: Trottered XY Spin Phase Phonon Evolution. Phonon population of a single mode where the trotter time is $0.675/\delta$ (a). This figure shows that the phonon population is small as long as the trotter time is not close to $1/2\delta$. The phonon evolution is compared to a continuous Hamiltonian with $\delta = 0.3\eta\Omega$ where the phonon population is large. A similar comparison is made when the trotter time is exactly $1/(2\delta)$ (b). Here the phonon population is growing linearly with time indicating that certain trotter times cannot be used. Finally the phonon populations of many modes for a random trotter time is shown. Since the populations get very large if the trotter time is $\sim (2n+1)/(2\delta)$ and the number of modes increases with ion number, for any trotter time it is highly likely that some of the normal modes will have a large phonon population. This makes trottering an XY Hamiltonian impossible for a large system.

the number of trotter steps, there is still a large population entangled with the phonons leading to effective spin decoherence.

At first glance, this issue can be solved by making the trotter time not equal to or even close to $(n + 0.5)/\delta$ where n is an integer for all motional modes. This is easily accomplished for two or three ions. However as more ions are added to the trap, the density of “bad” times grows quickly due to there being more motional modes with the same requirement and the problem rapidly becomes intractable. An example is shown in Fig. 2.6c, where an arbitrary trotter time is chosen in a system of ten ions. The figure shows large population excursions and are compared to a close detuned constant interaction. Changing the time by a little changes which modes have these large excursions, but they do not go away. For ten, it still might be possible to find a time which does not have this phonon generation, but any noise on the trap frequency would immediately change this stable point and destroy the simulation. This becomes even harder as the number of spins increases. For this reason, trotterization between a $\sigma_x\sigma_x$ and a $\sigma_y\sigma_y$ Hamiltonian from a M-S interaction is not practical with a large chain of spins, despite the proof of principle in two ions.

Chapter 3: Experimental apparatus

3.1 Experimental Overview

In this chapter, I will give a brief overview of the techniques and equipment used to trap and coherently manipulate the ions. Much more detailed accounts of this apparatus can be found in [48–50]. I will also present our current hypothesis as to what limits the lifetimes of long chains of ions and the steps we have done in order to mitigate it. I then show a simple derivation of the spontaneous emission rate along with direct measurements in a chain of ten ions. Finally, I recount the methods we use to analyze the camera data along with an exposition of the data processing used to recover fidelity lost by known measurement error.

3.1.1 Trapping Ions

$^{171}\text{Yb}^+$ ions are confined using a hand-assembled, three-layer, linear RF-Paul trap. RF voltages with a frequency of ~ 38 MHz are applied via a quarter-wave helical resonator to the central layer, generating a pseudo-potential which has a linear node along the center of the trap parallel to the electrode plane. This pseudo-potential node defines the \hat{z} axis of the trap. The pseudo-potential itself is confining

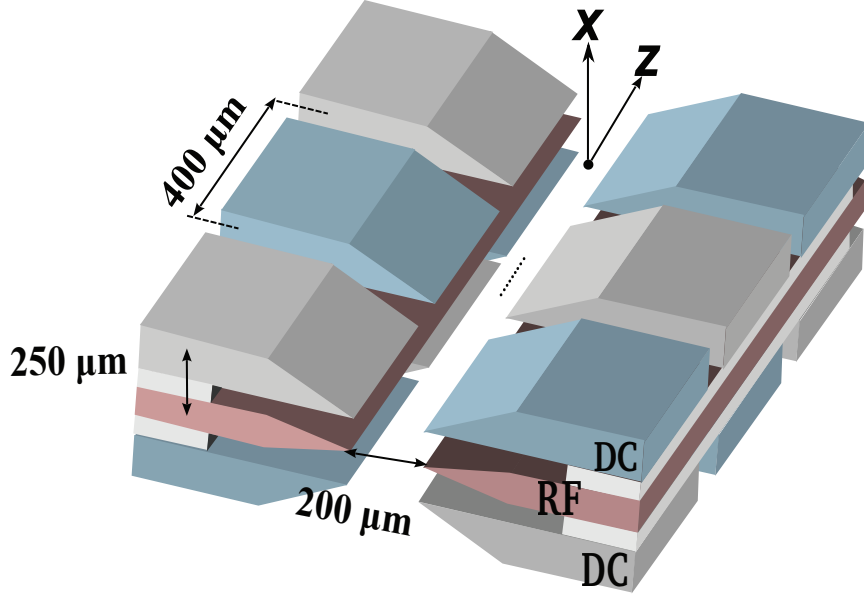


Figure 3.1: Schematic of trap electrodes. RF voltage is applied to central layer (highlighted in red) and provides confinement along \hat{x} and \hat{y} . Electrodes in gray are grounded while electrodes in blue carry DC voltages which provide axial confinement and also a quadrupole to break the degeneracy of the \hat{x} and \hat{y} secular frequencies. Ions are imaged along \hat{x} direction.

in the radial directions (\hat{x} and \hat{y}). The outer two layers of the trap have DC voltages applied which provide axial confinement (\hat{z}) and also a quadrupole used to break the radial secular frequency degeneracy. The whole electrode assembly is suspended in a ultra-high vacuum (UHV) chamber which is evacuated to 10^{-11} Torr or less.

Ions are loaded using an ^{171}Yb isotope enriched oven which is heated to produce a flux of neutral atoms across the trapping region. At the trapping region, neutral atoms are excited by a laser at 399 nm, resonant with the 1S_0 to 1P_1 transition, which is applied perpendicularly to the atomic flux in order to minimize Doppler shifts and give isotope selectivity. A second beam at 355 nm photo-ionizes the atoms by way of a resonantly assisted, dichroic, two-photon transition [61, 62]. Deterministic loading of single ions is achieved by pulsing the 355 nm light for a short time and then

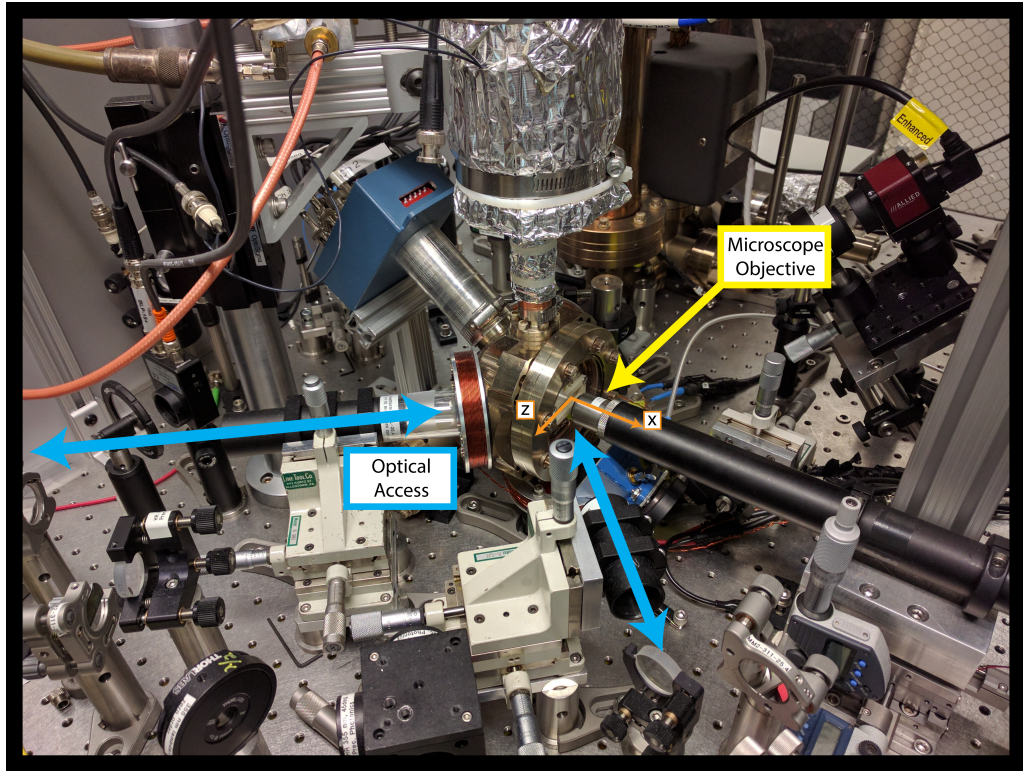


Figure 3.2: Picture of UHV chamber on table. Chamber has a large window close to trap for imaging ion fluorescence. Optical access is limited by microscope objective to paths which are at ~ 45 deg to large window via small windows on backside of chamber. Trap axes are denoted, showing imaging axis along \hat{x} .

waiting for the ions to cool down, which is repeated until the requisite number of ions is loaded, allowing large chains of exact size to be loaded quickly and efficiently. By automating the loading process and using image processing techniques to count the number of ions on the camera, I was able to greatly improve the rapidity and ease of loading large deterministic numbers of ions.

While one ion can be loaded in a high RF trap (secular frequency in \hat{x} direction is $\omega_x \sim 5$ MHz), we have found that in order to load larger chains we need to lower both the RF confinement and the DC confinement in order to load efficiently. We refer to this lowering of voltages as “recrystallizing”. When at the lower recrystallized voltages, we are able to quickly ionize and cool many ions at the cost of generating thermal drifts in the helical resonator due to the change in applied power. For this reason, we try to keep the time spent at the lower voltages to a minimum and then wait for the same amount of time the trap was low after loading in order to allow the system to re-equilibrate.

Currently what limits the number of ions which can be used in quantum simulations is collisions with the residual background gas in the UHV chamber. Under a catastrophic collision at high RF, the chain destabilizes and “melts”. This means that the ions are no longer able to be cooled by the lasers, which we believe is due to the ion orbits becoming large enough that the high RF is driving energy into the system. In order to cool the atoms and reform the linear ion crystal, we slowly recrystallize attempting to recover all ions. For small and medium size chains, this technique works well and allows for immediate recovery. Large chains (> 12) typically do not recool all ions. We believe that either the ions are hot enough that they

cannot be efficiently cooled or their spatial orbit lies outside the intensity profile of the lasers. While it is possible that the ions not recovered might have escaped the trap, this is unlikely due to the well depth (~ 1 eV). Since we believe that it is more likely that the ions are still trapped but hot, not recovering all ions requires that the ions are dumped and a new chain loaded in order to prevent further catastrophic events caused by the extremely hot ions in large orbits.

3.1.2 Resonant Light

The ions are cooled, initialized, and measured by means of a resonant cycling transition between the $^2S_{1/2}$ and $^2P_{1/2}$ manifolds which is at 369.5 nm. With a ~ 5 G magnetic field as a quantization axis, the Zeeman frequency is ~ 7 MHz while the spontaneous emission rate of $^2P_{1/2}$ is 20 MHz, allowing all three Zeeman states of the $F = 1$ $^2S_{1/2}$ to be excited using the same laser. When driven, this cycling transition produces a high flux of photons which is then collected onto the imaging device, whereas the singlet state of the ground state manifold cannot be coupled to the excited state singlet because it is dipole forbidden. Thus an ion in the singlet state appears dark, allowing for detection of the qubit state of the atom, where $|1\rangle$ is bright and $|0\rangle$ is dark.

The excited state manifold has a small probability (0.5%) of decaying into a low lying D -state. Since the state $^2D_{3/2}$ has a life-time of 52.7 ms, which is very long compared to the experimental reptime, a repump laser at 935 nm is used to drive population into the $^3[3/2]_{1/2}$ state which has a short life-time of 37.7 ns. Since

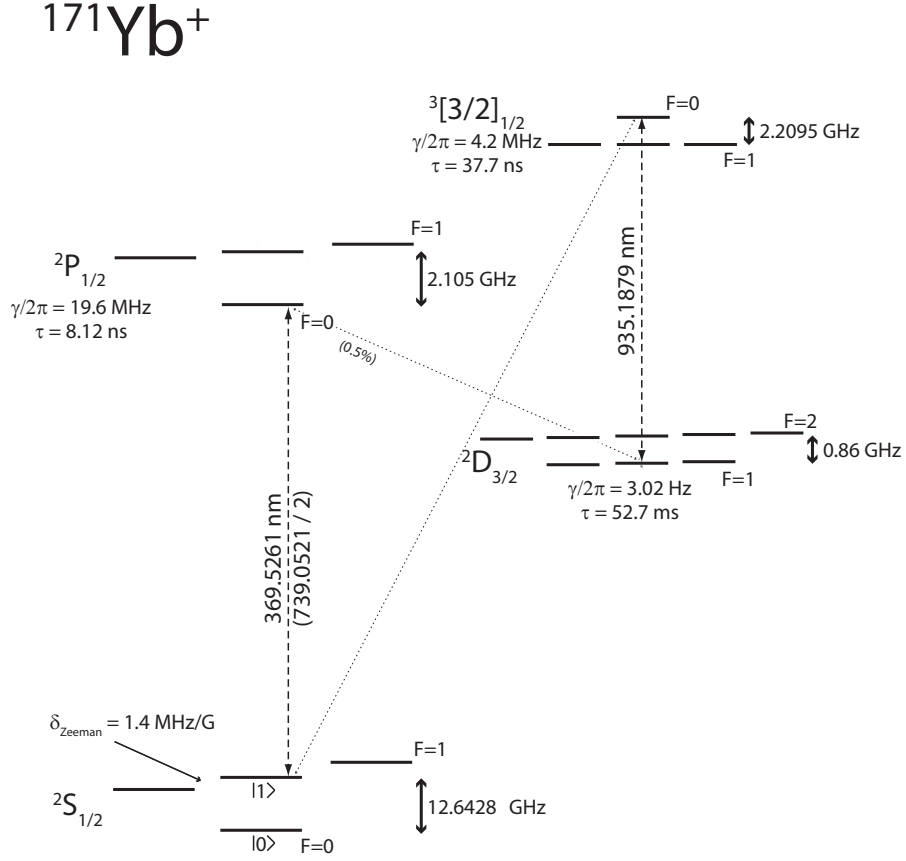


Figure 3.3: Cycling transition level diagram in $^{171}\text{Yb}^+$. The primary cycling transition in $^{171}\text{Yb}^+$ is between $|^2S_{1/2}, F=1\rangle$ and $|^2P_{1/2}, F=0\rangle$. There is a small probability of decay into a low lying metastable state $^2D_{3/2}$. Due to dipole selection rules, this only decays to the $F=1$ manifold of the D state from the $F=0$ level in the P state. A repump laser at 935 nm then drives the population back to the $F=1$ states in the ground state manifold via the $F=0$ state in the $^3[3/2]_{1/2}$ manifold without mixing $|1\rangle$ and $|0\rangle$ since a $F=0$ to $F=0$ transition is forbidden. Since the $[3/2]$ state has fairly high spontaneous emission rate, there is not a large suppression of the fluorescence.

the coupling of the $F = 0$ state in the $[3/2]$ manifold and $|0\rangle$ is dipole forbidden, there is no mixing of $|1\rangle$ and $|0\rangle$ due to the repump, closing the cycling transition loop. While the repump does not mix $|1\rangle$ and $|0\rangle$, there is a small probability of off-resonant coupling via the $F = 1$ manifold of $^2P_{1/2}$. This can lead to mis-diagnosis of the atomic state, which will be discussed later in this chapter.

In order to initialize the ions, we resonantly couple the $F = 1$ manifolds of $^2S_{1/2}$ and $^2P_{1/2}$. The excited states all have a $1/3$ probability of decaying into the singlet ground state. Thus after scattering only a few photons, all ions are optically pumped into $|0\rangle$ with $> 99\%$ fidelity. This enables deterministic initialization of all spins with high fidelity. For this reason, every experiment begins by first Doppler cooling and then optically pumping the ions into $|0\rangle$.

Doppler cooling is performed using a beam which is 10 MHz detuned from resonance. The optical power of the doppler cooling beam is optimized by performing red sideband thermometry [50] on the ion during the daily calibration and adjusting the power for minimal \bar{n} . When holding an ion chain and not running experiments, the Doppler cooling beam power is increased to make the chain more resilient to background gas collisions. During loading and recrystallization, this power is further increased to its maximum in order to quickly cool the ions and prevent ion loss. Further, another color which is 50 MHz detuned from resonance is also applied simultaneously in order to cool the first micro-motion sideband at 38 MHz. Without this second color, loading and maintaining large chains becomes difficult since the chain is not linear at the recrystallized voltages, but is in fact a zig-zag type configuration. When in this configuration with large ion numbers, many ions no longer

sit on the RF null, making cooling more difficult due to micro-motion. Even when the RF is restored to full strength, the chain is more resilient due to the cooling of the first micro-motion sideband. Thus better lifetimes are achieved by cooling both the zeroth and the first micro-motion sideband while the chain is not in use, but during experiments only the optimized Doppler cooling that is 10 MHz detuned is used in order to achieve the lowest possible temperature. Using this technique, we are able to load and hold extremely large chains and still achieve extremely low Doppler temperatures.

3.1.3 Longer Lifetimes

What follows is a small aside on observations regarding large chain lifetimes. Recently, we were able to demonstrate the ability to coherently work with ≥ 20 spins. Up to now the greatest number we had been able to work with was 18 spins [46]. The reason was that as we increased the ion number the rate of catastrophic background gas collisions also went up. This led to a chain lifetime of $\lesssim 1$ minute for large crystals, whereas loading and recovering took well over a minute, making it practically impossible to take data.

This improved dramatically once we optimized the frequency of the 935 nm repump beam by maximizing the detection scattering rate of a chain of 10 ions. This is very unintuitive since the 935 nm transition is power-broadened from 4 MHz to over 150 MHz, making changes on the order of 20 MHz in the 935 frequency imperceptible with one ion. Yet it appears that the ion chain lifetime is sensitive to

leading to RF heating as opposed to confinement. Due to the suppressed cooling rate of the chain from the dark ion, chain cannot be cooled as quickly as they are heated and so the ions are then heated until either they are too hot even for far detuned light to cool or they are spending too much time outside the spatial profile of the Doppler cooling beam. We believe that this is why we need to drop the RF in order to recover or load more ions, in order that we lower the effective RF heating rate so that our cooling can overcome the heating. This also explains why some ions are not recovered, as they have been heated beyond our ability to cool them.

Under this hypothesis, we believe that our lifetimes are improved dramatically by improving the repump rate simply because if there is some small probability of collision while in the D state $p_c = \tau s$ where τ is the dwell time in the D state and s is the background gas collision rate, then the probability of not having a collision in the D state for a single ion is $p = 1 - p_c$. Since this process is independent for each ion, in a chain of N spins the probability that no ion has a collision is p^N . This effect makes the chain lifetimes drop off rapidly with even small decreases to this repump rate in addition to the increased collision rate due to the increased size of the chain. By optimizing cooling along with maximizing the repump rate, we believe that we improved the resilience of the chain to collision, reducing the incidence of catastrophic collisions.

3.1.4 Coherent Control

As mentioned in chapter 2, we use a pulsed laser to produce the necessary frequencies used for coherent control. Specifically, we use a ND:YVO₄ tripled pulsed laser (Coherent - Paladin compact 355-4000) which has a center frequency at 355 nm. The pulse duration of the laser is $\tau \sim 14$ ps, giving a spectral bandwidth of ~ 70 GHz, and has a repetition rate of $f_{rep} \sim 120.125$ MHz. By selecting the comb-tooth $n = 105$, we find that $f_{HF} - n f_{rep} = 29.7$ MHz. This frequency difference is easily spanned using acousto-optical modulators (AOMs). The AOMs act as both a fast switch and frequency control, transferring control of optical frequencies and intensity to control of microwave frequency and power. Experimentally, this maps the exquisite control we have in the microwave regime to the ion, allowing for coherent control of each spin with the manipulation of microwaves.

In order to generate two beams, we split each pulse out of the laser in two using a 50/50 beam splitter. Each beam arm is controlled using an AOM (Brimrose QZF-210-40-355). This light is then shaped and imaged onto the ion chain where both beams are applied in a non-copropagating configuration such that the difference in their wave-vector (Δk) is parallel to the \hat{x} axis of the trap. When the difference in the two AOMs is exactly 29.7 MHz, the two beams drive stimulated Raman transitions. The effective Lamb-Dicke parameter of the Raman beams along the \hat{x} axis is $\eta \sim 0.07$, which is large enough to allow for a significant coupling to the red and blue sidebands while keeping the second order sidebands minimal.

Since the 12.6 GHz beat-note at the ions is derived from the 105th comb-tooth,

it is extremely sensitive to small perturbations in the rep-rate, especially since we need the beat-note to be stable down to ~ 1 Hz. This requires a passive stability of the rep-rate at a fraction of a Hz, which is technically challenging if not impossible. Since the pulsed laser does not have a way to feed back to the cavity, we must compensate for this noise in some other way. By beating a fast-photodiode signal from the laser against a stable frequency source, we can feed forward to the frequency of one of the Raman AOMs, locking the beatnote of the two beams [63] even as the rep-rate fluctuates. With such a technique, the beatnote has been observed to be stable to < 1 Hz.

3.2 Spontaneous Emission

Within quantum information, true dissipation is always a constant threat. In trapped $^{171}\text{Yb}^+$ ions, one of the primary causes of dissipation is undesired spontaneous emission during coherent operations. The two primary causes of this unwanted spontaneous emission are resonant light leakage and off-resonant coupling. The first is a problem which can always be overcome by better engineering. The second is more difficult and due to fundamental physics and thus more interesting. In the following, I will first give a brief account of methods which can be used to diagnose resonant light leakage. I will then present a derivation of spontaneous emission due to the presence of far detuned 355 nm light and further compare the predicted spontaneous emission rate to observed spontaneous emission in a chain of ten ions.

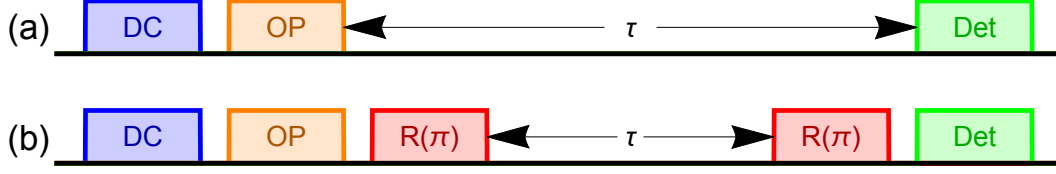


Figure 3.5: Schematic representation of resonant light leakage diagnosis experiments. In this figure, “DC” represents doppler cooling, “OP” optical pumping, “Det” detection, and “R(π)” a qubit rotation of π . Doppler cooling sideband leakage experiment (a). Experiment is as follows: doppler cool, optical pump, wait for time τ , detect. Ideal measurement is zero probability bright, so any bright state population is due to light leakage. Detection light leakage experiment (b). Experiment is as follows: doppler cool, optical pump, π rotation, wait for time τ , π rotation, detect. As before, the ideal case is zero probability bright, thus bright state population is due to leakage.

3.2.1 Resonant Light Leakage

The underlying cause of resonant light leakage is as simple as it sounds. It means that there is light resonant with a transition that couples the qubit to an excited state, which then decays and emits a photon. The real difficulty with resonant light leakage is that it only takes one photon from a resonant laser, and so we are talking about optical powers on the level of less than a nW. In this case, diagnosis is the key. There are two experiments which each test for a different kind of light leak.

The first test is as follows (see Fig. 3.5a): Doppler cool, optical pump, wait, and detect. The wait time τ should be on the order of 100 ms. This test measures the spontaneous emission due to the Doppler cooling sidebands, indicating a light leak from the Doppler cooling beam or any beam with those sidebands. The essence of this measurement is that the sidebands will make $|0\rangle$ scatter into the $F = 1$ manifold of the ground state making the ion appear bright, otherwise it will remain

dark. Thus, if there is not any light hitting the ion, the fluorescence will remain zero regardless of the length of τ . In practice this is fairly difficult to achieve and so we typically try to limit it to less than 15% brightness in 100 ms.

The second test is similar (see Fig. 3.5b): Doppler cool, optical pump, rotate qubit by π , wait, rotate qubit by π , detect. Again the wait time, τ , should be on the order of 100 ms. This test measures the direct light leakage from the detection transition by first rotating $|0\rangle$ to $|1\rangle$. If there is any detection light, the ion will scatter with a high probability into one of the Zeeman states and so the second π pulse will not affect them and again the ion will appear bright. Otherwise, it will appear dark. As before, the optimal measurement then would be zero fluorescence regardless of wait time. It is important that the pi-pulse be well calibrated so as not to introduce false signal, but the tolerated leakage should still be less than 15% in 100 ms.

If any issues are observed, further identification needs to be performed to narrow down which laser beam is leaking on the ion. The most effective way to identify the culprit is to put a ND filter wheel into the different suspect paths to see if the signal can be diminished or changed. Once the beam is identified, the possible reasons for the unwanted light can be scattering off of optics, RF leakage onto the AOM, and RF crosstalk to name a few.

3.2.2 Off-resonant Spontaneous Emission

Off-resonant spontaneous emission, unlike the resonant light leakage, is due to fundamental atomic physics and as such inherent to the system. In particular, I consider here the small off-resonant coupling due to the presence of the 355 nm light used to generate qubit operations. Previous estimations of this rate in our system over-estimated it by a factor of four [50, 64, 65]. I re-derive it here for clarity and find an equation consistent with [66, 67] and finally compare measured spontaneous emission in ten ions to the predicted value.

3.2.2.1 The Two Level System

We start by assuming a simple two level system with a detuned laser applied. The total scattering rate, γ_p , for this system is [68, p. 25]:

$$\gamma_p = \frac{s_0 \frac{\gamma}{2}}{1 + s_0 + \left(\frac{2\Delta}{\gamma}\right)^2} \quad (3.1)$$

where γ is the linewidth of the transition, $s_0 \equiv I/I_{sat}$, $I_{sat} \equiv \frac{\hbar\omega^3\gamma}{12\pi c^2}$, I is the applied intensity, ω is the radial resonant transition frequency, c is the speed of light, and Δ is the detuning of the applied light from the resonant frequency. Now if we assume that $\Delta \gg \gamma$ and that $s_0 \ll \left(\frac{2\Delta}{\gamma}\right)^2$, namely that the detuning is much greater than the linewidth and the saturation parameter is much smaller than the relative

detuning, we can make the approximation:

$$\begin{aligned}
\gamma_p &= \left(\frac{\gamma}{2\Delta}\right)^2 s_0 \frac{\gamma}{2} \left(\frac{1}{1 + \left(\frac{\gamma}{2\Delta}\right)^2 + s_0 \left(\frac{\gamma}{2\Delta}\right)^2} \right) \\
&= \left(\frac{\gamma}{2\Delta}\right)^2 s_0 \frac{\gamma}{2} \left(1 - \left(\frac{\gamma}{2\Delta}\right)^2 (1 + s_0) + O\left(\frac{\gamma}{2\Delta}\right)^4 \right) \\
&= s_0 \frac{\gamma}{2} \left(\left(\frac{\gamma}{2\Delta}\right)^2 - \left(\frac{\gamma}{2\Delta}\right)^4 (1 + s_0) + O\left(\frac{\gamma}{2\Delta}\right)^6 \right) \\
&\approx s_0 \frac{\gamma}{2} \left(\frac{\gamma}{2\Delta}\right)^2
\end{aligned} \tag{3.2}$$

The single photon Rabi frequency, $\Gamma \equiv \gamma \sqrt{\frac{I}{2I_{sat}}}$, can be used to rewrite Eq. 3.2 as the following:

$$\gamma_p = \gamma \left(\frac{\Gamma}{2\Delta}\right)^2 \tag{3.3}$$

This gives the rate at which the far detuned light will couple to the excited state in a simple two level system.

3.2.2.2 Generalization to $^{171}\text{Yb}^+$

In $^{171}\text{Yb}^+$, the laser can now couple to multiple excited states. For a first order estimation, we will consider simply the total rate of spontaneous emission and not worry about the final state. Under this assumption, we can calculate each excited state independently and their total will be the total spontaneous emission rate, γ_p , from a starting state A . Thus,

$$\gamma_{(p,A)} = \sum_B \gamma_B \left(\frac{\Gamma_{AB}}{2\Delta_B}\right)^2 \tag{3.4}$$

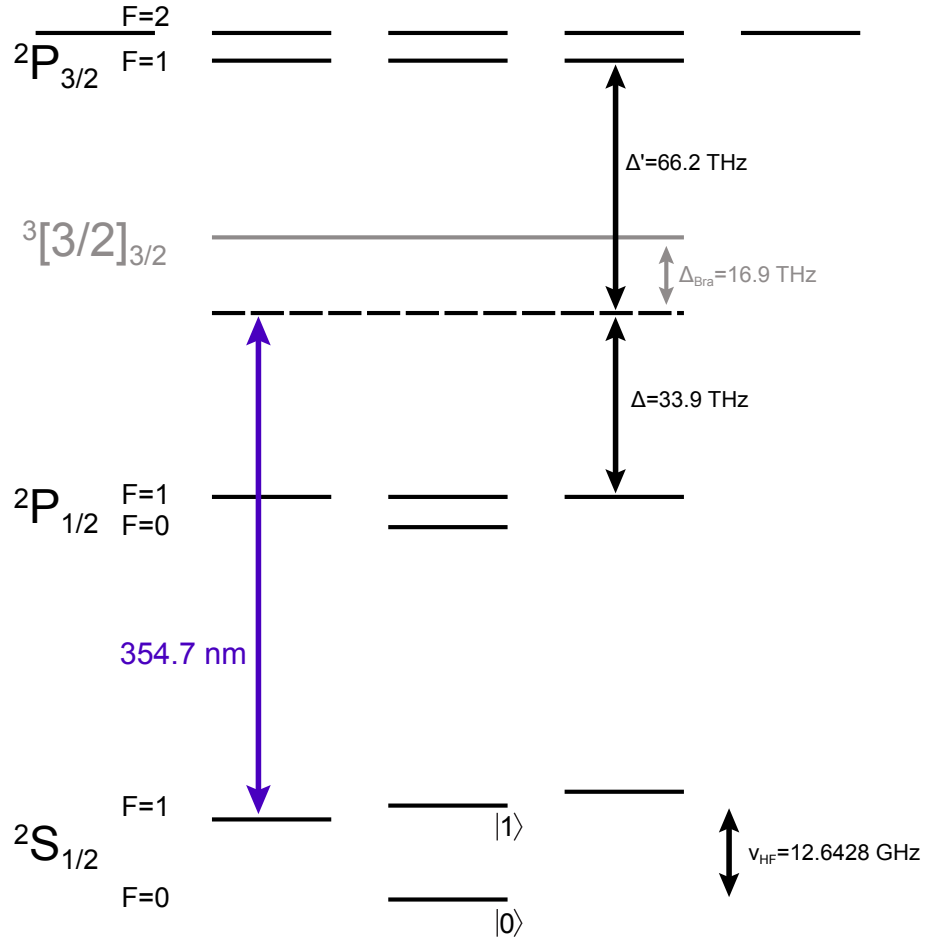


Figure 3.6: $^{171}\text{Yb}^+$ spontaneous emission level diagram. Relevant electron states when considering spontaneous emission from the 355 nm laser. Note that the $3[3/2]_{3/2}$ state has been included as it's proximity has an effect on the spontaneous emission of $\approx 10\%$.

where γ_B is the linewidth of the excited state B and Δ_B is the laser's detuning from state B . Γ_{AB} is the coupling between the two states by the laser:

$$\Gamma_{AB} = \langle B | \vec{\mathcal{E}} \cdot \vec{\mu} | A \rangle \quad (3.5)$$

where $\vec{\mathcal{E}} = \mathcal{E}\hat{\epsilon}$ is electric field of the laser with polarization $\hat{\epsilon}$ and $\vec{\mu}$ is the dipole moment. Now by applying Fermi's Golden Rule and doing some math, the following can be derived, but this has been done by Mizrahi [65, p. 77]. I will just summarize the results, namely

$$\Gamma_{AB} = \left(C_{AB,\epsilon} \sqrt{(2J' + 1)} \right) \Gamma_B \quad (3.6)$$

where $C_{AB,\epsilon}$ is the Clebsch-Gordan coefficients between the two states, A and B with a laser polarization of $\hat{\epsilon}$, J' is the total electron angular momentum of the excited state B , and $\Gamma_B = \gamma_B \sqrt{\frac{I}{2I_{satB}}}$ is the single photon Rabi frequency for the transition. Let us define

$$\hat{\epsilon} = \epsilon_- \hat{\sigma}_- + \epsilon_\pi \hat{\pi} + \epsilon_+ \hat{\sigma}_+ \quad (3.7)$$

and further require that $\epsilon_-^2 + \epsilon_\pi^2 + \epsilon_+^2 = 1$.

Calculating the values for $C_{AB,\hat{\epsilon}} \sqrt{(2J' + 1)}$ is straight forward and included in a summary of all single photon Rabi frequencies depending on polarization from the states $|0\rangle$ and $|1\rangle$ in the Table 3.2.2.2. The table takes advantage of the fact that the D1 manifold ($^2S_{1/2} \rightarrow ^2P_{1/2}$) and D2 manifold ($^2S_{1/2} \rightarrow ^2P_{3/2}$) have the property that $\Gamma_0 \equiv \gamma_{D1} \sqrt{\frac{I}{2I_{satD1}}} \approx \gamma_{D2} \sqrt{\frac{I}{2I_{satD2}}}$, differing only by about 3%. This approximation will be used throughout to simplify expressions.

Γ_{AB} for the D1 Manifold ($^2S_{1/2} \rightarrow ^2P_{1/2}$)					
m_F		F=0	F=1		
		0	-1	0	1
A	$ 0\rangle$	0	$\epsilon_- \frac{1}{\sqrt{3}} \Gamma_0$	$\epsilon_\pi \frac{1}{\sqrt{3}} \Gamma_0$	$\epsilon_+ \frac{1}{\sqrt{3}} \Gamma_0$
	$ 1\rangle$	$\epsilon_\pi \frac{1}{\sqrt{3}} \Gamma_0$	$\epsilon_- \frac{1}{\sqrt{3}} \Gamma_0$	0	$\epsilon_+ \frac{1}{\sqrt{3}} \Gamma_0$

Γ_{AB} for the D2 Manifold ($^2S_{1/2} \rightarrow ^2P_{3/2}$)							
m_F		F=1			F=2		
		-1	0	1	-1	0	1
A	$ 0\rangle$	$\epsilon_- \sqrt{\frac{2}{3}} \Gamma_0$	$\epsilon_\pi \sqrt{\frac{2}{3}} \Gamma_0$	$\epsilon_+ \sqrt{\frac{2}{3}} \Gamma_0$	0	0	0
	$ 1\rangle$	$\epsilon_- \frac{1}{\sqrt{6}} \Gamma_0$	0	$\epsilon_+ \frac{1}{\sqrt{6}} \Gamma_0$	$\epsilon_- \frac{1}{\sqrt{2}} \Gamma_0$	$\epsilon_\pi \sqrt{\frac{2}{3}} \Gamma_0$	$\epsilon_+ \frac{1}{\sqrt{2}} \Gamma_0$

Table 3.1: Table of single photon Rabi frequencies. A summary of all single photon Rabi frequencies, Γ_{AB} , from the states $A = |0\rangle$ and $A = |1\rangle$ to both the D1 manifold and the D2 manifold depending on polarization. The excited states are denoted by their total angular momentum, F, and its projection on the z-axis, m_F .

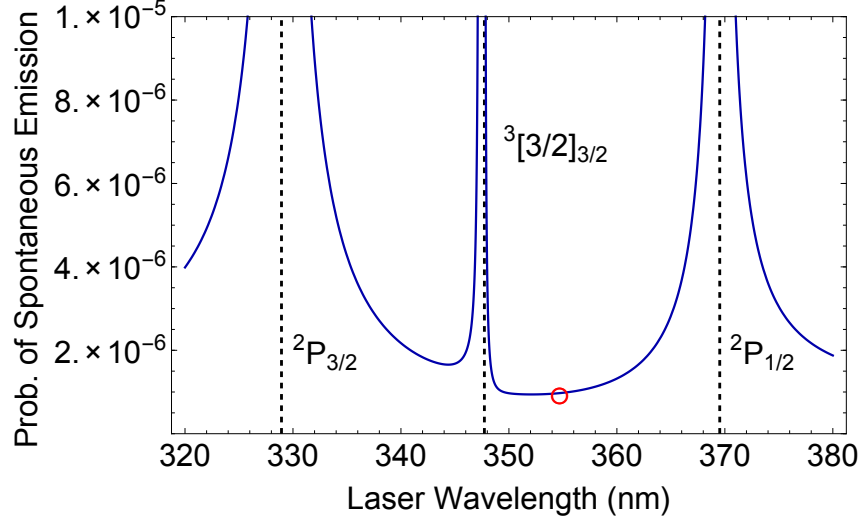


Figure 3.7: Probability of a spontaneous emission during a pi pulse as a function of wavelength. Important to note is that missing factors of 2 have been corrected from previous calculations, making it 4 times smaller than predicted prior.

If we only consider the D1 and D2 lines and ignore the hyperfine structure since it only modifies the answer on the order of $2\omega_{HF}/\Delta$, which in the worst case is 7×10^{-4} , then the total spontaneous emission rates for $\{|0\rangle, |1\rangle\}$, reduce to simply

$$\gamma_{(p,|0\rangle)} = \gamma_{(p,|1\rangle)} = \frac{\Gamma_0^2}{4} \left[\frac{1}{3} \frac{\gamma_{D1}}{\Delta^2} + \frac{2}{3} \frac{\gamma_{D2}}{(\Delta')^2} \right] \quad (3.8)$$

where Δ is the detuning from the D1 manifold and Δ' is the detuning from the D2 manifold.

There is actually an additional energy level that must be considered for this calculation due to its proximity, namely the $^3[3/2]_{3/2}$ state, which is only 16.9 THz away [69]. A good explanation of what a bracket state is and how to understand it has been done by Senko [50] and won't be repeated here. Writing the state in the

LS basis,

$$|{}^3[3/2]_{3/2}\rangle = \sqrt{\frac{10}{21}} |{}^2P_{3/2}\rangle + \sqrt{\frac{8}{21}} |{}^4P_{3/2}\rangle + \frac{1}{\sqrt{35}} |{}^2D_{3/2}\rangle - \frac{2}{\sqrt{35}} |{}^4D_{3/2}\rangle \quad (3.9)$$

we see that the overlap with $|{}^2P_{3/2}\rangle$ is almost half. The lifetime of this state has not been measured but has two separate calculated lifetimes of $\tau = 120$ ns [70] and $\tau = 150$ ns [71] which gives a line-width of $\gamma/2\pi = 1.1 \pm 0.3$ MHz. If we incorporate this bracket state as if it were simply, to leading order, a ${}^2P_{3/2}$ state, then the spontaneous emission in Eq. 3.8 is modified to

$$\gamma_{(p,|\{1,0\})} = \frac{\Gamma_0^2}{4} \left[\frac{1}{3} \frac{\gamma_{D1}}{\Delta^2} + \frac{2}{3} \frac{\gamma_{D2}}{(\Delta')^2} \right] + \frac{\Gamma_{Bra}^2}{4} \frac{2}{3} \frac{\gamma_{Bra}}{(\Delta_{Bra})^2} \quad (3.10)$$

where Γ_{Bra} is the single ion Rabi frequency for the bracket state and Δ_{Bra} is the laser detuning from the state. Using this equation, we can examine the probability of spontaneous emission during a π pulse as a function of wavelength which is shown in Fig. 3.7. By measuring the Rabi frequency at the ions, we can also calculate what the spontaneous emission probability is as a function of time. For a single Raman beam and one ion, even out at 50 ms, there is still less than 4% probability. Still, since each ion has an independent probability, p , to spontaneously emit, then the probability to not have a single spontaneous emission event in a chain of N ions is $(1 - p)^N$. Using the same parameters, the probability of a single ion in a chain of N ions spontaneously emitting is shown for multiple N in Fig. 3.8. Assuming a 10 ms total experimental time, Fig. 3.8 exhibits what this exponential scaling implies:

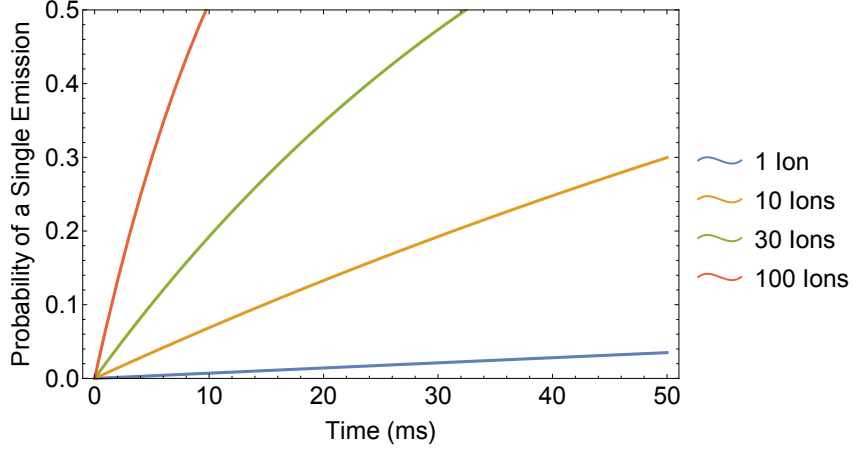


Figure 3.8: Probability of a single spontaneous emission in N ions. Due to the exponential scaling with system size, spontaneous emission errors become a significant consideration at the time-scale of experiments at 30 ions. With 100 ions, spontaneous emission will be a dominant error-source.

while for 10 spins and maybe even 30 spins this spontaneous emission can be treated perturbatively, at 100 spins one of the dominant errors will be spontaneous emission.

We can use the exponential scaling of the spontaneous emission probability to experimentally measure the spontaneous emission rate. With a system of ten ions, we perform an experiment similar to that of Fig. 3.5a, except this time, instead of letting the ions sit in the dark, we instead apply a single Raman beam to the chain and wait. Any ions that measure as bright beyond the normal background have had a spontaneous emission event. Using the camera, we can count the number of ions bright and measure the rate at which the zero bright population decreases. Just such a measurement is shown in Fig. 3.9 for ten ions. A baseline with no applied light was measured and showed no change for the duration of the experiment. Whereas when the light is applied, by fitting the decay of the 0 bright population to an exponential of $e^{-Nt/\tau}$, we can extract the spontaneous emission rate, namely $\gamma_{(p, \{1,0\})} = 1/\tau = 2\pi 103 \pm 6$ mHz. This measured rate is consistent with the

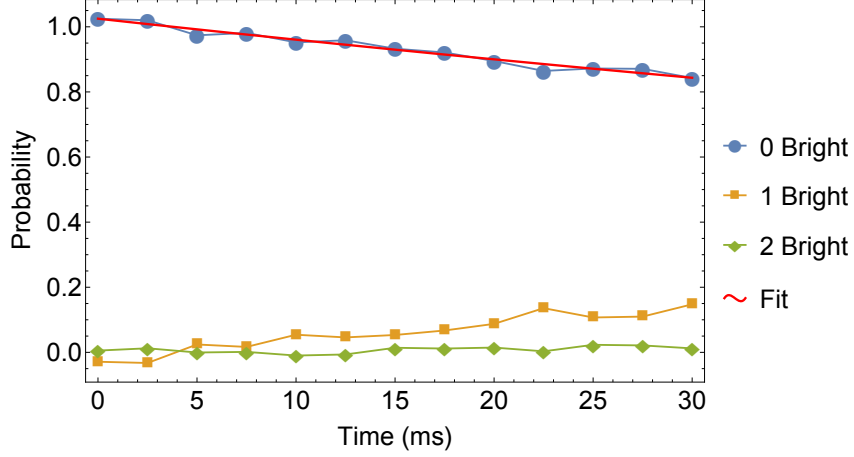


Figure 3.9: Measured spontaneous emission rate. Experiment is to prepare $N = 10$ ions dark and apply a Raman beam for some time t and then measure. By using the camera, we count the number of ions bright at the end of the experiment. We fit the decay of the zero ions bright to an exponential, $e^{-Nt/\tau}$. The spontaneous emission rate, $\gamma_{(p,|\{1,0\})}$, is then calculated $\gamma_{(p,|\{1,0\})} = 1/\tau = 2\pi 103 \pm 6$ mHz

predicted value from Eq. 3.10 and Fig. 3.7.

Further, the spontaneous emission is difficult to improve beyond the observed value. From Fig. 3.7, it is clear 355 nm is a local minimum in spontaneous emission and in fact does not improve as the wavelength gets larger than 369 nm due to the large drop in Rabi frequency. The spin-spin interaction used to generate entanglement is proportional to the square of the intensity I , namely $J \propto (\eta\Omega)^2/\delta$ where $\Omega \propto I$ and δ is the detuning from the motional mode. Initially, this indicates that increasing the intensity would effectively suppress the spontaneous emission, since $\gamma_{(p,|\{1,0\})} \propto I$ and J is increasing quadratically with intensity, thus performing the simulation faster than the spontaneous emission events. Yet in the slow gate regime, where δ must be much greater than $\eta\Omega$, the optimal detuning is $\delta \approx 3\eta\Omega$. Plugging this back in to the equation for J , we see that J is effectively proportional to the intensity and that there is no suppression of the spontaneous emission in the slow

gate regime. As we scale up to larger systems, we will have to be more aware of spontaneous emission in the simulations, especially since there is a $2/3$ probability that the event will take the atom outside the qubit basis.

3.3 State Detection

As discussed above, state detection is performed using state-dependent fluorescence which is collected on either a photo-multiplier tube (PMT) or an intensified charge-coupled device (ICCD). The collection optic for the light is a 0.23 NA microscope objective (CVI UVO-20.0-10.0) which is used in a finite conjugate configuration with an effective front focal length of ~ 18 mm, which is then imaged by a doublet onto the measurement device, giving an effective total magnification of ~ 200 . Between the objective and the camera is an adjustable zero aperture iris (ThorLabs SM1D12CZ) for spatial filtering and two interference filters for color selectivity at 370 nm, one which is a 10 nm narrow band around 370 nm (Semrock FF01-370/10-25) and the other which is a long pass filter (Semrock LP02-355RS-25). These filters effectively suppress the background scatter from room light to less than 1 photon at the camera. We can switch from the camera to a PMT by using a simple flipper mirror, where there is an additional 370 nm narrow band filter for better 355 nm suppression at the PMT. Since the PMT area is smaller than that of the camera, there is a demagnifying lens in the PMT arm of the imaging system.

The PMT (Hamamatsu H10682-210) has a quantum efficiency of $\sim 30\%$ at 370 nm. We use the PMT for diagnostics and calibrations because of the near

instantaneous readout and low noise. Typical mean photon counts on the PMT within an $800\ \mu\text{s}$ window is ~ 18 while background counts are ~ 3 . The excess background counts are due to reflections of the resonant light off of the Raman optics after the trap reflecting back into the imaging optics. While not ideal, since all data is taken using the ICCD camera which has spatial discrimination, the large background is not problematic.

The ICCD camera (Princeton Instruments PI-Max3:1024i) has a smaller quantum efficiency of $\sim 20\%$ at $370\ \text{nm}$. While this is comparable to the PMT, there are additional complications in any amplified CCD that decrease the signal-to-noise ratio. Since the ICCD amplifies the photo-electrons by using an electron cascade, the pixel values end up having a super-Poissonian distribution which has twice the variance of the photon distribution [72]. This effectively halves the signal-to-noise of the camera in single shot measurements due to a much larger overlap with the dark distribution. In order to recover a comparable signal-to-noise, the camera exposure is doubled to $1.5\ \text{ms}$. The drawback is that due to the off-resonant coupling of the detection light to the $F = 1$ states of the $^2P_{1/2}$ manifold, there is a greater chance of misdiagnosis of dark as bright.

The PI-Max3:1024i has also presented significant technical difficulties. The largest problem is that the charge transfer operations of the CCD are not efficient when the camera run with a fast clock-speed at low light levels. This leads to a displacement and elongation of the signal in the vertical shift direction. In order to collect the signal, we have to integrate most of the CCD in the vertical direction (approximately half). By using the hardware binning feature, which for a binning

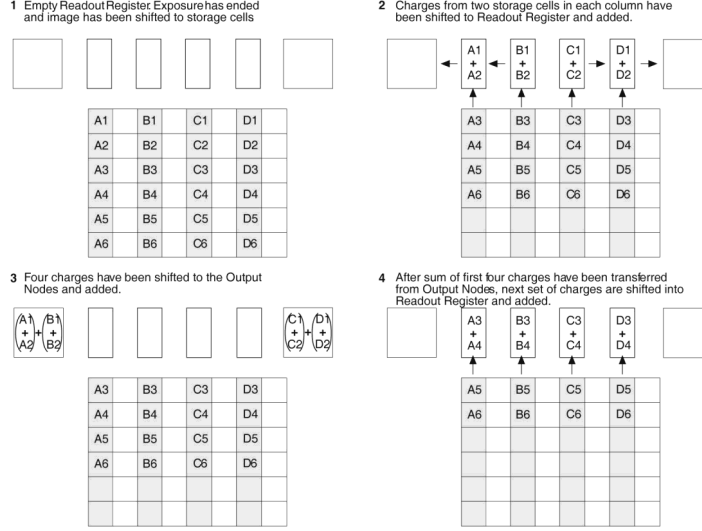


Figure 3.10: Schematic representation of CCD hardware binning. When using the hardware binning on a PI-Max3:1024i, the photo-sensitive pixels are first shifted to the adjacent storage pixels. For a binning of 2×2 , first two successive vertical shift operations are performed, followed by two horizontal shift operations in the readout register. Then once the four pixel's worth of charge has been combined and shifted to the output node, the charge is readout, creating only one “super-pixel” of data. This is then repeated. Compliments of Princeton Instruments.

of $m \times n$ collects m pixels horizontally and n pixels vertically prior to read out, we can generate “super-pixels” which recover most of the signal. The optimal hardware binning parameters is a binning of 4×64 , which is highly asymmetric in order to compensate for the poor fidelity of the shift operations.

Another difficulty stemming from the hardware is that the base background value of each pixel was dependent on the time between readouts. What we observed is that for long experiments (~ 5 ms or more), the background values of each pixel grows to be comparable to the original signal size. The growth of this background is due to the accumulation of dark charge which is exacerbated as the camera heats up during heavy data collection. Thankfully, the photon signal is additional to this background value and not competing with it, meaning that the effective signal to

noise is approximately the same, just with a larger offset. This issue made any discrimination of the ion signal based directly on the pixel values prone to errors.

One final issue is the overlap of the point-spread functions (PSF) of the ion fluorescence on the camera. With only an $\text{NA}=0.23$, the final width of the PSF when observed on the camera is comparable to the effective inter-ion spacing, meaning that ion crosstalk is a non-negligible source of error. This issue is compounded as the axial trap is tightened or more atoms are added to the trap.

We examined multiple methods of analysis [73] and due to these issues, we settled on a method of analysis that attempted to mitigate the effect of most of the issues.

3.3.1 Camera Analysis

In order to reduce data handling overhead, the pictures are summed down to a single row, reducing the dimension of the data to 1-D. By calibrating the center of each ion PSF and its width on the camera, a sum of N Gaussians is fit to the data where there are only N free parameters, namely the height of each Gaussian distribution. A Gaussian is used as the fundamental distribution because the PSF of a point source, namely an Airy disk, has a large overlap with a Gaussian. A sum of Gaussians is used so that the ion crosstalk is diminished since the overlap of distributions is taken into account by the fitting itself. There is an additional free parameter which is the global offset to the whole distribution. This global offset compensates for the growth of the background and only requires that there is at

least an ion width of dark area outside of the ion chain on each side. Once the data has been fitted, the state of each ion reduces to the discrimination of the Gaussian amplitude.

The fitting of this distribution requires prior knowledge of the ion number, positions and widths. Discrimination requires high statistics in order to determine the optimal threshold and what the resulting errors are. We calibrate these parameters prior to data collection by using 1000 images of an all bright chain and 1000 images of an all dark chain. These calibration images are first averaged with the averaged dark image being used as a background. The resulting background-subtracted distribution is used to determine the parameters for each ion's Gaussian distribution. An example of this averaged distribution can be seen in Fig. 3.11a. Once the Gaussian parameters are calibrated, the Gaussian distribution is then fit to each of the 2000 calibration images. A histogram of each set of images is generated in order to optimize the threshold.

In the ideal case, the point where the bright histogram and dark histogram have equal error is the best point to discriminate. In the current apparatus, this is not the case because despite the fact that the fitted Gaussians take into account the PSF overlap, the photon counts are low enough that the data is fairly stochastic. Figure 3.11b shows a single image of bright 24 ions which has only been background subtracted and shows how large signal spikes can occur even in-between ions. This results in a residual inter-ion crosstalk which increases the bright and dark histogram separation biasing the discrimination towards the bright state. This is especially apparent when looking at spin chain configurations with alternating spin states. To

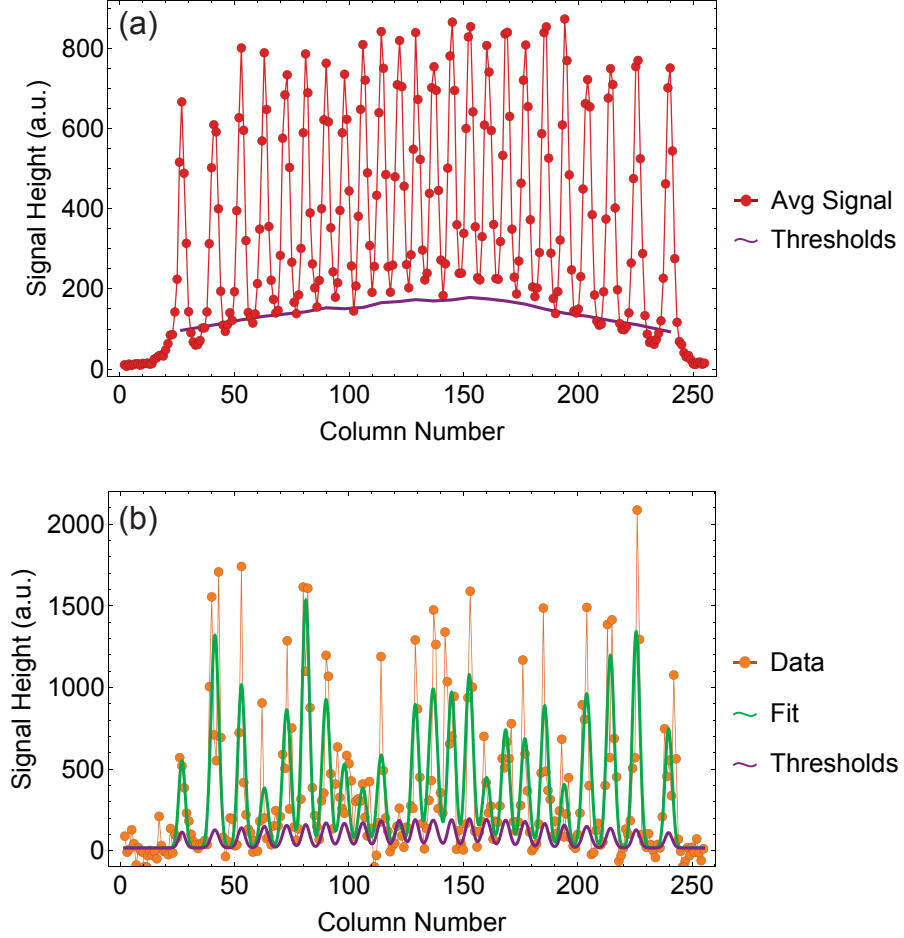


Figure 3.11: Example of camera summed row data. Averaged signal from a twenty-four ion calibration (a). Ions are optically pumped dark for 1000 images, which are averaged together to form the background. Ions are rotated bright for 1000 images, which are then averaged and background subtracted, producing an average signal. This is used to calibrate fit of the distribution. Also displayed are the thresholds associated with each ion, indicating height that fitted Gaussian must be in order to be determined bright. Single image summed row distribution (b). Displayed here are the background subtracted single image data and the associated Gaussian fit. Small photon numbers lead pixel heights to have a wide variance. Also shown are threshold Gaussian amplitudes, showing that threshold sizes are reasonable.

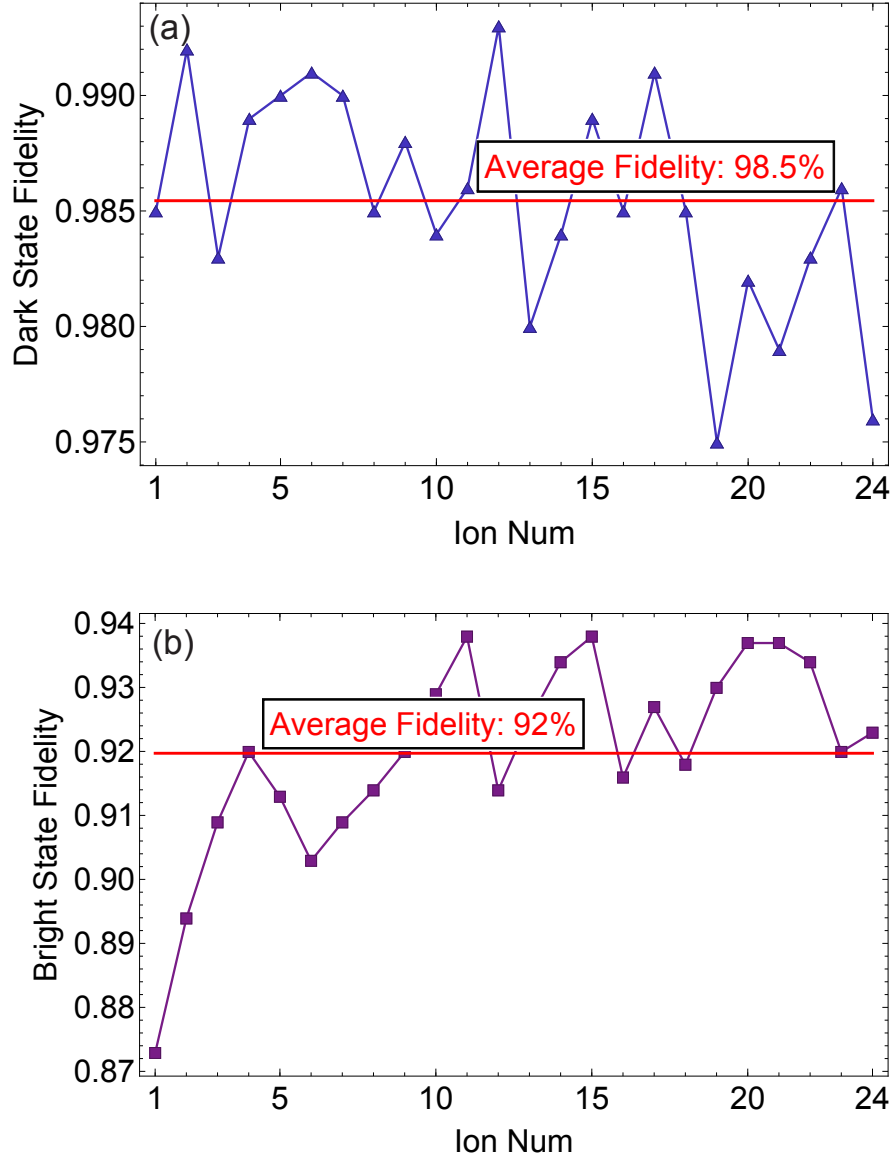


Figure 3.12: Example raw ion fidelities using ICCD. Raw dark/bright state fidelities after discrimination (a)/(b). Due to bias required in bright state thresholds to suppress inter-ion crosstalk, the resulting raw bright state fidelities are typically worse than raw dark state fidelities. For this string of twenty-four ions, the averaged dark state fidelity is 98.5% and the averaged bright state fidelity is 92%

compensate for this, we apply thresholds to the data with the following equation:

$$T(I) = T_0 + \eta B(I) \quad (3.11)$$

where T is the threshold value for ion I , T_0 is a threshold offset chosen to be slightly larger than the individual summed column noise, and η is a scaling coefficient for the background due to adjacent ion overlap $B(I)$. The calculated threshold is shown in Fig. 3.11a. In comparison to the relative background, it is clear why this threshold is scaled by background from the other ions. This type of operation allows for the maximal sensitivity to staggered states. The drawback is that this greatly increases the error on the bright state. In Fig. 3.12, we show the resulting bright and dark fidelities, where there is an average of fidelity of 98.5% for the dark and 92% for the bright.

Ultimately these fidelities are insufficient to make any observations of any global spin observable as the observable fidelity $\mathcal{F} \sim (f)^N$ where f is the single ion fidelity in an N spin system. For a twenty-four spin system with a single ion fidelity of 95%, the global observable fidelity is only 29%, where now the single largest error is just due to detection error.

3.3.2 Detection Correction

The solution to this difficulty is to leverage the knowledge we have of the detection infidelities in order to compensate for the detection error. These detection errors are corrected using a data processing technique described in [74]. We will

first lay out an intuitive understanding of this error correction and then describe the technique in [74] as it is implemented in our analysis.

For a single qubit, the most generic representation is a 2×2 matrix:

$$D = \begin{bmatrix} 1 - p_0 & p_1 \\ p_0 & 1 - p_1 \end{bmatrix} \quad (3.12)$$

where p_0 (p_1) is the error on the bright (dark) state. If we take some ideal input probability distribution of g_i , then the observed probabilities f_i are $F = DG$. This is just a prediction of what the observation will be based on our knowledge of p_0 and p_1 . In order to recover the ideal probabilities from our imperfect measurement, we just need to invert the equation $G = D^{-1}F$. This works very well for a single ion.

The key observation of [74] was that for an N spin system, the $2^N \times 2^N$ matrix M_{ji} equivalent to the single spin matrix D , where $f_j = \sum_{i=1}^{2^N} M_{ji}g_i$, has a very simple tensor product structure. In other words, we can instead express M_{ji} as

$$M = \otimes_{k=1}^N D_k \quad (3.13)$$

where D_k is the single ion detection matrix for ion k . This is critical, as a general matrix M is not necessarily invertible and even if it is, M has 2^{2N} elements which makes constructing it difficult, let alone inverting it due to the cost in computational resources as N gets larger. Since M can be expressed as this tensor product, inverting M is as simple as inverting each D_k which has a very simple analytic

expression:

$$M^{-1} = \otimes_{k=1}^N D_k^{-1} = \otimes_{k=1}^N \begin{bmatrix} 1 - p'_{0,k} & p'_{1,k} \\ p'_{0,k} & 1 - p'_{1,k} \end{bmatrix} \quad (3.14)$$

where

$$\begin{aligned} p'_{0,k} &= \frac{p_{0,k}}{p_{0,k} + p_{1,k} - 1} \\ p'_{1,k} &= \frac{p_{1,k}}{p_{0,k} + p_{1,k} - 1} \end{aligned} \quad (3.15)$$

with $p_{0,k}$ ($p_{1,k}$) is the bright (dark) error for ion k . Solving for the real probability distribution g_i from the observed probability distribution f_i , we find $g_i = \sum_{j=1}^{2^N} M_{ij}^{-1} f_j$, allowing us to recover the real probabilities by just constructing M^{-1} .

Now in general M^{-1} is still a very large matrix and computationally costly to compute. For some idea of the resources involved, a twenty-four spin M^{-1} has $2^{48} \sim 2.8 \times 10^{14}$ elements and is not sparse. If each entry is an 8-byte float, the amount of memory required to just store the matrix is 2.2 petabytes.

One additional observation in [74] greatly improves this resource cost. Assume that for an N spin system, we want to measure some observable \hat{O} which is some combination of spin projections. We can write \hat{O} as a tensor product of Pauli matrices, namely $\hat{O} = \otimes_{k=1}^N \sigma_k^{\mu_k}$, where $\sigma_k^{\mu_k}$ is a component of the Pauli matrices for spin k with $\mu_k = 1, 2, 3 \equiv x, y, z$ and $\mu_k = 0$ is the identity matrix. In order to measure a particular axis of the Bloch sphere, that axis is coherently rotated into the \hat{z} basis which is the measurement basis. Thus \hat{O} can be written as diagonal matrix with $\hat{O} = \otimes_{k=1}^N \text{diag}(\sigma_k^{\mu_k})$ where $\text{diag}(\sigma_k^{\mu_k}) = [1, -1]$ for $\mu_k \neq 0$ and $[1, 1]$ for $\mu_k = 0$, implying that \hat{O} can be simplified to a vector of length 2^N . With a probability

distribution of g_i , the expectation value of \hat{O} becomes simply $\langle \hat{O} \rangle = \sum_i \hat{O}_i g_i$. Yet, applying the results above, we find

$$\begin{aligned}
\langle \hat{O} \rangle &= \sum_i \hat{O}_i g_i \\
&= \sum_i \hat{O}_i \sum_j M_{ij}^{-1} f_j \\
&= \sum_j \left(\sum_i \hat{O}_i M_{ij}^{-1} \right) f_j \\
&= \sum_j \hat{O}_j^c f_j
\end{aligned} \tag{3.16}$$

where \hat{O}^c now defines a corrected operator. This corrected operator can be written using $M^{-1} = \otimes_{k=1}^N D_k^{-1}$, namely $\hat{O}^c = \otimes_{k=1}^N [\text{diag}(\sigma_k^{\mu_k}) D_k^{-1}]$. This equation reduces the computation of a $2^N \times 2^N$ matrix to only computing a 2^N vector. The elements for this vector are expressed simply as

$$\hat{O}^c = \otimes_{k=1}^N [(1 - 2p'_{0,k}), -(1 - 2p'_{1,k})]. \tag{3.17}$$

Generating this vector for \hat{O}^c can be accomplished very efficiently, making this an effective technique even at larger ion numbers ($N < 30$).

We implement this in the data analysis by first taking the discriminated spin values and constructing a probability vector of all 2^N possible spin states for the chain. Then the ion errors from the camera calibration are used to either generate the full matrix M^{-1} when we are measuring the global state probabilities or only the single spin magnetization vector \hat{O}_k^c of the k th spin for magnetization measurements.

These single spin magnetization vectors can be multiplied together to generate correlation measurements to as many orders as required. The distinction of purpose arises since when constructing the corrected operators, the observable is being corrected, not the probabilities. When using the full matrix M^{-1} on the measured probability vector, the matrix effectively moves population around to compensate for the observation error whereas the corrected observable simply rescales the final value of the observable. Ultimately, constructing the full matrix and finding the real probabilities g_i and then constructing the observable versus constructing the corrected observable result in slightly different answers because the full matrix is more sensitive to the detection error calibration.

If we let the bright and dark detection errors be the same $p_0 = p_1 = p$ for the sake of brevity, then a relative error e in the calibration of p is $\delta p/p \sim e$. The support of \hat{O} , n_p , is equivalent to the number of Pauli matrices in the tensor product of \hat{O} . Thus the single spin magnetization has a support of $n_p = 1$ whereas a two-point correlation function has a support of $n_p = 2$. Now, the error in the corrected observable \hat{O}^c due to calibration error is $\delta\langle\hat{O}^c\rangle/\langle\hat{O}^c\rangle \sim 2n_p p e$. Constructing the matrix has a support of $n_p = N$, whereas constructing \hat{O}^c only has the support of the observable. For this reason and also since it is computationally more tractable, it is always preferable to use the corrected observable.

3.3.3 Independent Component Analysis (ICA)

As our working system sizes have increased, there has been a dramatic increase in the computation time required to perform the data analysis. This slow down is a direct consequence of the increase in the number of free parameters in the Gaussian amplitudes fit. For a system of 26 spins, analysis of a scan with 21 points and 1000 experiment per point takes over 24 hours. This is not tenable, especially when considering system sizes of > 50 spins and the corresponding non-linear increase in analysis time. Any replacement of this Gaussian amplitude fit needs to not only be more computationally efficient, but also automatically determine the ion positions on the camera.

The ideal case would be to generate a set of basis images where only one ion is bright and the rest are dark. Analysis would then just be the convolution of the basis images with the data images, where the basis image would act as a mask, selecting out the fluorescence from only a one ion, leading to a signal value for that ion. This would then be discriminated in the exact same way as the Gaussian amplitudes. Further, the basis images could be used to extract and compensate the inter-ion crosstalk, further improving over the Gaussian amplitude difficulties described.

The difficulty is that generating these basis images is arduous as preparing a single spin excitation for each spin has a high experimental time cost, whether it be using single-site addressing or by moving a single ion around. A better method would be to use an algorithm to identify what fluorescence belongs to each ion. One very good possibility is to use independent component analysis (ICA). ICA is an ideal

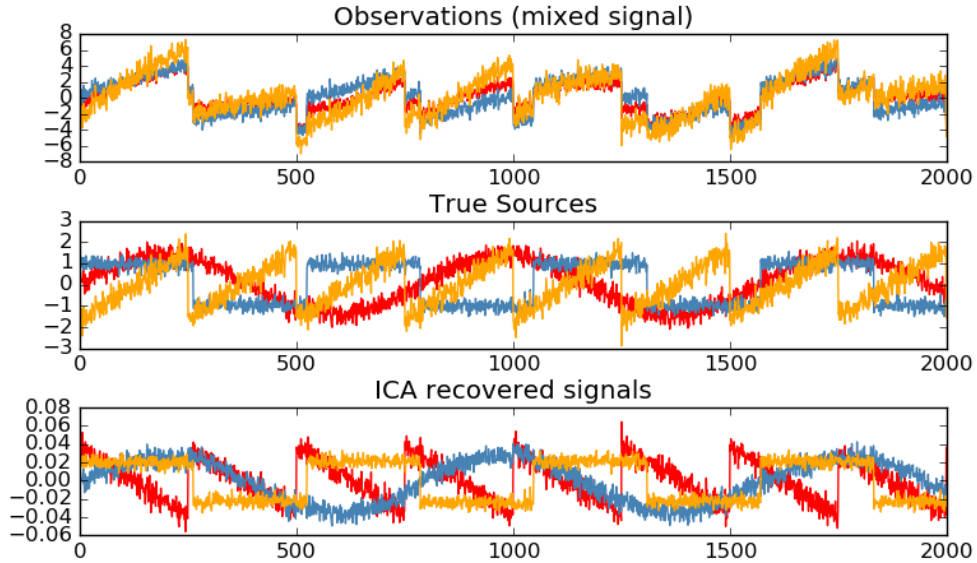


Figure 3.13: Fast ICA blind source separation. Fast ICA is used here to identify super-imposed sources in noisy data. First image is the “observed” signals. Second image is the true sources used to generate the data. Third are the components recovered by the ICA algorithm. These recovered signals are the same as the true sources up to a minus sign. All credit for image to scikit-learn.

algorithm for separating superimposed signals, one classic example being the “blind source separation” problem. In the blind source separation problem, there are, for example, three audio sources which are recorded by three separate microphones. The problem is to recover the true sources by examining their superposition from the three separate recordings, which ICA does remarkably well.

We can map the problem of identifying ions directly to the blind source separation [75]. This is done by reducing each image to a 1-D array where each row is appended in sequence. Finding the ions in the image now is the same as finding its unique “frequency” in the waveform of the picture. As long as the number of images input is much greater than the number of ions, this now reduces to the same problem as that of blind source separation. Now there is one very stringent

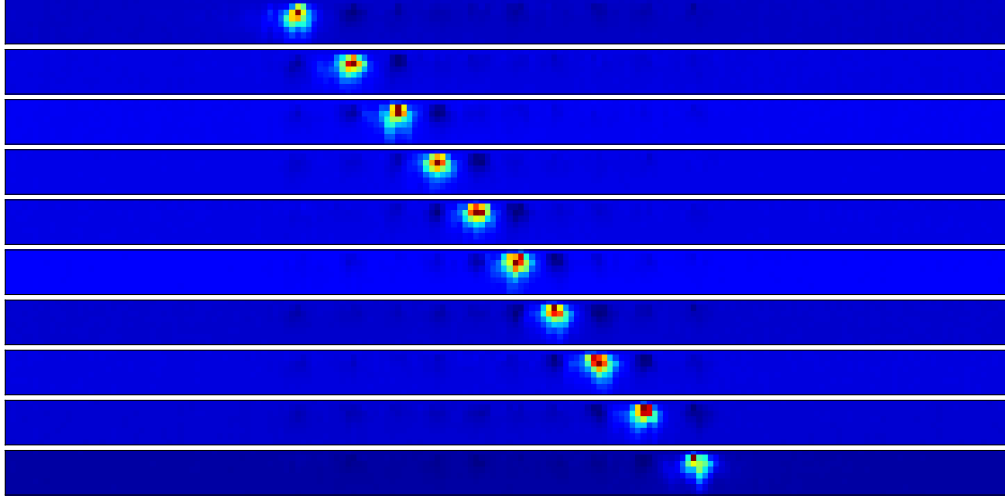


Figure 3.14: Basis images from FastICA algorithm. “FastICA” from the is applied to 10,000 images of ions with $\pi/2$ rotation in order to make signals uncorrelated. Result is 10 images, each with a single ion separated out. These basis images are then used as a mask for the data to determine ion brightness.

requirement to using ICA that can make or break the algorithm and that is the sources being examined must be statistically independent. For the ion system, this requires essentially that $\langle \sigma_z^i \sigma_z^j \rangle = 0$ for all pairs. This is achieved by simply rotating all spins by $\pi/2$. An example of this being applied to a 10 ion system can be seen in Fig. 3.14. The particular implementation of ICA is from the open-source Python package of Scikit-Learn and called “FastICA”.

While this algorithm works well for small system sizes (~ 10 ions), when the system gets much larger the algorithm has a high failure rate. Initially, the quality of the images were suspected, but later it was realized that in fact the $\pi/2$ pulses on the outer ions were no longer $\pi/2$ but were under-rotated. Thus their signals were no longer statistically independent and so the ICA could no longer appropriately distinguish them as a source. In order to implement this as a replacement to the current analysis, it requires that the $\pi/2$ pulses are even across the chain. Currently

the Raman beams are used to perform the $\pi/2$ pulse leading to the issues described, but this can be circumvented by using microwaves for the calibration images which should produce much more even rotations.

Chapter 4: Fourth Order Stark Shift

The pervasive challenge facing all quantum information platforms is the undesired interaction of the qubit with environment. In trapped ions, one such coupling to the environment is via the modulation of the qubit energy splitting by stray magnetic fields. This can be circumvented by using clock-states, allowing for coherence times exceeding 10 minutes [76, 77]. However, the use of clock-state qubits by definition does not easily allow the direct generation of certain classes of Hamiltonians that are equivalent to the modulation of qubit energy splittings [58]. In quantum computing, such control is desirable for efficiently realizing universal logic gate families such as arbitrary rotations [78].

In this chapter, I propose and demonstrate the use of a fourth-order Stark shift to achieve fast, individually addressed, single-qubit rotations in a chain of $^{171}\text{Yb}^+$ ions. We experimentally realize up to a 10 MHz shift on the qubit splitting with only moderate amounts of laser power. We exploit this control in a quantum system of 10 ions by preparing arbitrary initial product states and applying an independent programmable disordered splitting on each lattice site in a quantum simulation, all demonstrated with low cross-talk.

4.1 Fourth-order Stark Shift Theory

The studies reported here are performed on a linear chain of $^{171}\text{Yb}^+$ ions, but can be generalized to any species of clock qubits. Here we will adopt the notation $^2\text{S}_{1/2} |F=0, m_f=0\rangle$ and $^2\text{S}_{1/2} |F=1, m_f=0\rangle$ are denoted as $|0,0\rangle$ and $|1,0\rangle$ respectively.

We assume the ions are irradiated using an optical frequency comb generated from a mode-locked laser with a center frequency detuned by Δ from the $^2P_{1/2}$ manifold and by $\omega_F - \Delta$ from the $^2P_{3/2}$ manifold. We assume that the pulse area of each laser pulse is small and has only a modest effect on the atom, and that the intensity profile for each pulse is well approximated by a hyperbolic secant envelope [64]. Under these assumptions, the k th comb tooth at frequency $k\nu_{rep}$ from the optical carrier has a resonant $S \rightarrow P$ Rabi frequency [79],

$$g_k = g_0 \sqrt{\pi \nu_{rep} \tau} \text{sech}(2\pi k \nu_{rep} \tau) \quad (4.1)$$

where τ is laser pulse duration, $g_0^2 = \gamma^2 \bar{I} / 2I_0$, \bar{I} is the time-averaged intensity of the laser pulses, I_0 is the saturation intensity of the transition, and γ is the spontaneous decay rate. Since $\sum_{k=-\infty}^{\infty} g_k^2 = g_0^2$, and assuming the parameters specified above, the second-order Stark shift $E_\alpha^{(2)}$ of state $|\alpha\rangle$ due to the frequency comb can be

computed for an arbitrary polarization (taking $\hbar = 1$) [64, 66]:

$$\begin{aligned} E_{00}^{(2)} &= \frac{g_0^2}{12} \left(\frac{1}{\Delta} - \frac{2}{\omega_F - \Delta} \right) \\ E_{10}^{(2)} &= \frac{g_0^2}{12} \left(\frac{1}{\Delta + \omega_{HF}} - \frac{2}{\omega_F - (\Delta + \omega_{HF})} \right). \end{aligned} \quad (4.2)$$

Here we neglect all excited state hyperfine splittings since they only contribute to the Stark shifts at a fractional level of $\sim 10^{-5}$. We also ignore all other states outside of the P manifold since their separation from the ground S states are too far detuned from the applied laser fields to give appreciable Stark shifts.

Assuming that 20 mW of time-averaged power is focused down to a 3 μm waist, the differential second-order Stark shift on the qubit splitting is $\delta\omega^{(2)} = E_{10}^{(2)} - E_{00}^{(2)} = -1.5$ kHz.

We will show that there is a fourth-order effect that can be much larger than the differential second-order Stark shift when using a frequency comb for specific polarizations of the beam. An intuitive understanding can be gained by considering that any two pair of comb teeth, k_0 and k_1 , have a beat-note frequency $(k_0 - k_1)2\pi\nu_{rep}$. If the bandwidth of the pulse is large enough, then there will be beat-notes that are close to the ground state hyperfine splitting. Assuming that none are on resonance, these off-resonant couplings can have a large effect on the ground states, as much as three orders of magnitude larger than the differential AC Stark shift.

We first calculate the fourth-order Stark shift in the simplified case of just two comb teeth and one excited state of the $^{171}\text{Yb}^+$ level structure (see Fig. 4.1), equiv-

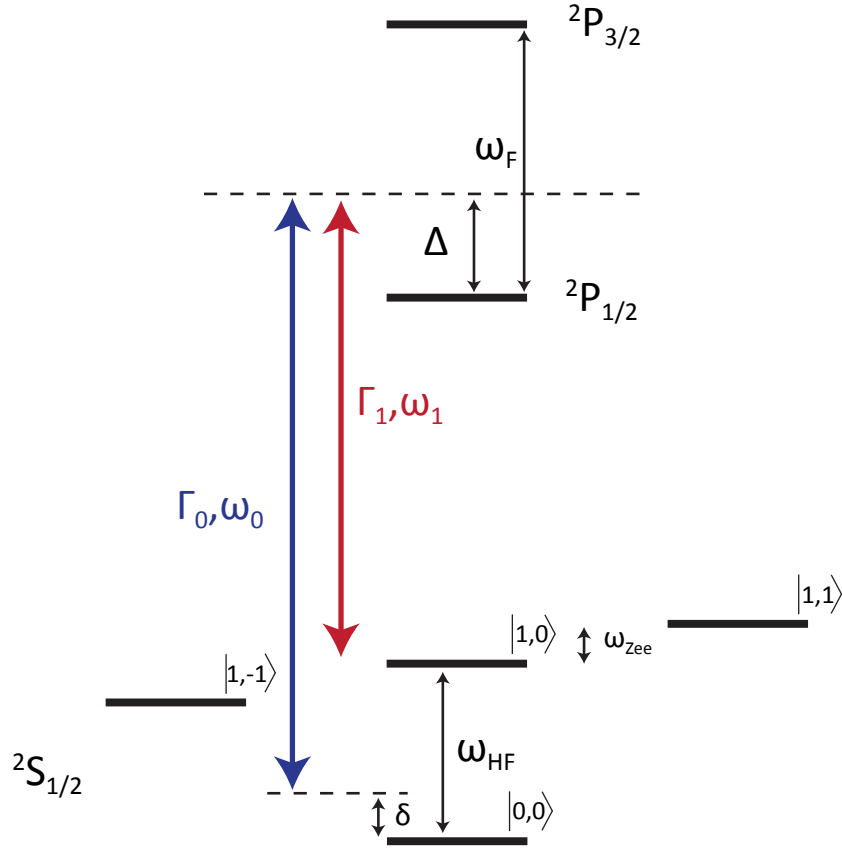


Figure 4.1: Schematic representation of the electron energy levels of $^{171}\text{Yb}^+$. When two phase-coherent colors of light are applied to the atom which have a beatnote approximately equal to the qubit splitting, there is an effective fourth-order differential light shift which can be much larger than the second-order differential Stark shift.

alent to two phase coherent continuous wave (CW) beams in a three level system. Let the excited state $|e\rangle$ have frequency splitting ω_e from the $|0,0\rangle$ ground state, and the absolute frequencies of the comb teeth k_0 and k_1 be ω_0 and ω_1 respectively. Also, let the polarization of each tooth, i , be defined as $\hat{\epsilon}^i = \hat{\epsilon} = \epsilon_- \hat{\sigma}_- + \epsilon_0 \hat{\pi} + \epsilon_+ \hat{\sigma}_+$ with $|\epsilon_-|^2 + |\epsilon_0|^2 + |\epsilon_+|^2 = 1$ where $\hat{\sigma}_-$, $\hat{\pi}$, and $\hat{\sigma}_+$ are the polarization basis in the frame of the atom. In the rotating frame of the electro-magnetic fields of the laser, we can write the Hamiltonian

$$\begin{aligned}\mathcal{H} &= \mathcal{H}_0 + V \\ &= \delta |1,0\rangle \langle 1,0| + \Delta |e\rangle \langle e| \\ &\quad + \frac{\Gamma^0}{2} |0,0\rangle \langle e| + \frac{\Gamma^1}{2} |1,0\rangle \langle e| + h.c.\end{aligned}\tag{4.3}$$

where \mathcal{H}_0 contains the diagonal terms and V includes the off-diagonal terms induced by the laser, $\delta = \omega_{HF} - (\omega_0 - \omega_1)$, $\Gamma^i = g_0 C(\hat{\epsilon}^i)$ is the resonant Rabi frequency from beam i with a dipole coupling matrix element $C(\hat{\epsilon}^i)$ for polarization $\hat{\epsilon}^i$. The fourth-order correction $E_n^{(4)}$ to the ground state energy levels, from perturbation theory, has the following form:

$$\begin{aligned}E_n^{(4)} &= \sum_{j,l,m \neq n} \frac{V_{n,m} V_{m,l} V_{l,j} V_{j,n}}{E_{n,m} E_{n,l} E_{n,j}} - \frac{|V_{n,j}|^2 |V_{n,m}|^2}{E_{n,j} (E_{n,m})^2} \\ &\quad - 2V_{n,n} \frac{V_{n,m} V_{m,l} V_{l,n}}{(E_{n,l})^2 E_{n,m}} + V_{n,n}^2 \frac{|V_{n,m}|^2}{(E_{n,m})^3}.\end{aligned}\tag{4.4}$$

Here j, l, m , and n each represent different energy levels, $V_{a,b} = \langle a|V|b\rangle$, $E_{a,b} = E_a^{(0)} - E_b^{(0)}$ is the unperturbed energy difference between the states $|a\rangle$ and $|b\rangle$.

Applying this to the Hamiltonian above, the last two terms are zero since V has no

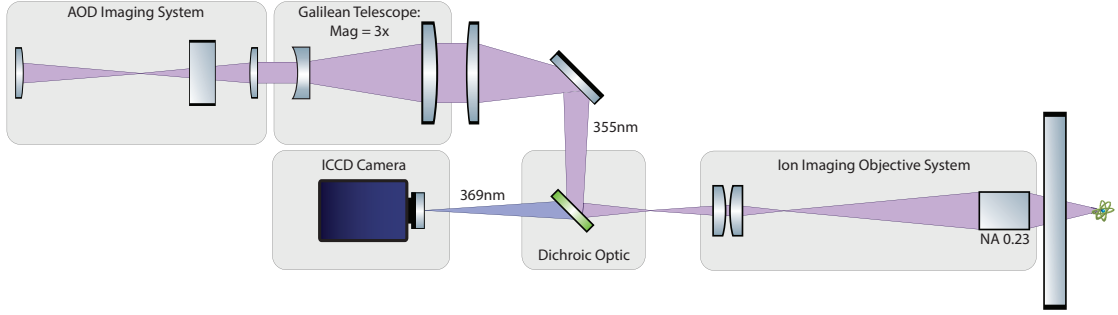


Figure 4.2: Diagram of optics imaging 355nm light onto single ion. Final spot size is $< 3 \mu\text{m}$, giving rise to controllable and individual-addressed Stark shifts on the qubits. This optical system utilizes a NA 0.23 objective lens for state detection of the ions at 369nm. Since the AOD is not imaged, deflections at the AOD correspond to displacement at the ions. This maps RF drive frequency to ion position, enabling control of the horizontal position of the beam.

diagonal terms leaving the fourth-order Stark shifts of the qubit levels,

$$\begin{aligned} E_{00}^{(4)} &= -\frac{|\Omega|^2}{4\delta} \\ E_{10}^{(4)} &= \frac{|\Omega|^2}{4\delta}. \end{aligned} \tag{4.5}$$

In these expressions, we assume $\delta \ll \Delta$ and $\Gamma_0 \sim \Gamma_1$. We also parametrize $\Omega = \Gamma_0\Gamma_1/2\Delta$, which is the resonant ($\delta = 0$) stimulated Raman Rabi frequency.

The above derivation is valid for any three level system. We now include the more complete case in $^{171}\text{Yb}^+$ where all excited states with major contributions, namely the $^2P_{1/2}$ and $^2P_{3/2}$ manifolds, are considered. Calculating the fourth-order Stark shift on any state $|n\rangle$ reduces to computing its shift due to all other states coupled via a two-photon Raman process by fields at frequencies ω_0 and ω_1 . In $^{171}\text{Yb}^+$, this means we must consider all hyperfine ground states. The two Zeeman states, $|F = 1, m_f = \pm 1\rangle$, of the ground state manifold will be denoted as $\{|1, 1\rangle, |1, -1\rangle\}$.

To calculate the fourth-order Stark shift, we sum over all states $|a\rangle \neq |n\rangle$,

$$E_n^{(4)} = \sum_{a \neq n} \frac{\Omega_{n,a}^2}{4\delta_{n,a}} \quad (4.6)$$

where $\Omega_{n,a}$ is the two-photon Rabi frequency between $|n\rangle$ and $|a\rangle$, $\delta_{n,a} = \omega_a - (\omega_0 - \omega_1)$, and $\omega_a = E_a^{(0)} - E_n^{(0)}$. Computing all of the relevant Rabi frequencies $\Omega_{n,a}$ under the same assumptions as in Eq. 4.2 [66], we find

$$\begin{aligned} \Omega_{00,10} &= (\epsilon_-^0 \epsilon_-^{1*} - \epsilon_+^0 \epsilon_+^{1*}) \Omega_0 \\ \Omega_{00,1-1} &= -(\epsilon_-^0 \epsilon_\pi^{1*} + \epsilon_\pi^0 \epsilon_+^{1*}) \Omega_0 \\ \Omega_{00,11} &= (\epsilon_+^0 \epsilon_\pi^{1*} + \epsilon_\pi^0 \epsilon_-^{1*}) \Omega_0 \\ \Omega_{10,1-1} &= (\epsilon_-^0 \epsilon_\pi^{1*} + \epsilon_\pi^0 \epsilon_+^{1*}) \Omega_0 \\ \Omega_{10,11} &= (\epsilon_+^0 \epsilon_\pi^{1*} + \epsilon_\pi^0 \epsilon_-^{1*}) \Omega_0. \end{aligned} \quad (4.7)$$

Here $\Omega_0 = \frac{g_0^2}{6} \left(\frac{1}{\Delta} + \frac{1}{\omega_F - \Delta} \right)$ and $g_0^2 = \gamma^2 \bar{I} / 2I_0$. From Eq. 4.7, we see that if $\hat{\epsilon} = \hat{\sigma}_\pm$, the Rabi frequency $\Omega_{00,10}$ is maximized and equal to Ω_0 . If instead $\hat{\epsilon} = \hat{\beta} \equiv 1/2\hat{\sigma}_- + 1/\sqrt{2}\hat{\pi} + 1/2\hat{\sigma}_+$, which corresponds to a circularly polarized input beam, then $\Omega_{00,10} = 0$ while all other Rabi frequencies are equal to $\Omega_0/\sqrt{2}$. It should be noted that a linear polarization from a single beam cannot drive Raman transitions between any of the $^{171}\text{Yb}^+$ hyperfine ground states. These polarizations are the two which provide the largest Rabi frequencies, while all others have smaller effective Rabi rates, so we dwell on these two cases. An important note is that in the case of $\hat{\epsilon} = \hat{\beta}$, $E_{10}^{(4)} = 0$ because the shifts from $|1, 1\rangle$ and $|1, -1\rangle$ are equal and cancel each

other.

We now compute the differential fourth-order Stark shift on the qubit states

$|1, 0\rangle$ and $|0, 0\rangle$, $\delta\omega^{(4)} = E_{10}^{(4)} - E_{00}^{(4)}$,

$$\delta\omega^{(4)} = \begin{cases} \frac{\Omega_0^2}{2\delta_{00,10}} & \text{when } \hat{\epsilon} = \hat{\sigma}_{\pm} \\ \frac{\Omega_0^2}{8} \left(\frac{1}{\delta_{00,11}} + \frac{1}{\delta_{00,1-1}} \right) & \text{when } \hat{\epsilon} = \hat{\beta}. \end{cases} \quad (4.8)$$

Finally, we generalize to incorporate all possible pairs of comb teeth. The two-photon Rabi frequency for any two comb teeth k_0 and k_1 , where $k_1 - k_0 = l$ is $\Omega_n = g_{k_0}g_{k_0+l}/2\Delta \approx \Omega_0 \text{sech}(\pi l \nu_{rep} \tau)$ [79]. Let j be defined such that $|\omega_a - 2\pi j \nu_{rep}|$ is minimized, assuming that it is nonzero. If we now plug this into Eq. 4.6 summing over all comb teeth, we find

$$\begin{aligned} E_n^{(4)} &= \sum_{a \neq n} \frac{\Omega_{n,a}^2}{4} \sum_{k=-\infty}^{\infty} \frac{\text{sech}^2((j+k)\pi \nu_{rep} \tau)}{\delta_{n,a} - k(2\pi \nu_{rep})} \\ &= \sum_{a \neq n} C_{n,a} \frac{\Omega_{n,a}^2}{4\delta_{n,a}} \end{aligned} \quad (4.9)$$

where $\delta_{n,a} = \omega_a - j(2\pi \nu_{rep})$, and

$$C_{n,a} = \sum_{k=-\infty}^{\infty} \frac{\text{sech}^2((j+k)\pi \nu_{rep} \tau)}{1 - k(2\pi \nu_{rep})/\delta_{n,a}}. \quad (4.10)$$

Because the denominator in Eq. 4.10 grows rapidly with k , only the closest few beatnotes are important, and as long as $2\pi \nu_{rep} \gg \omega_{Zee}$, then $E_{10}^{(4)}$ remains zero for

$\hat{\epsilon} = \hat{\beta}$. The differential fourth-order Stark shift then becomes

$$\delta\omega^{(4)} = \begin{cases} \mathcal{C}_{00,10} \frac{\Omega_0^2}{2\delta_{00,10}} & \text{when } \hat{\epsilon} = \hat{\sigma}_{\pm} \\ \frac{\Omega_0^2}{8} \left(\frac{\mathcal{C}_{00,11}}{\delta_{00,11}} + \frac{\mathcal{C}_{00,1-1}}{\delta_{00,1-1}} \right) & \text{when } \hat{\epsilon} = \hat{\beta}. \end{cases} \quad (4.11)$$

Assuming the same parameters as with the second-order Stark shift (20 mW of time-averaged power focused down to a 3 μm waist) and with $\nu_{rep} = 120$ MHz and $\tau = 14$ ps, we find that the fourth-order shift is

$$\delta\omega^{(4)}/2\pi = \begin{cases} 247 \text{ kHz} & \text{when } \hat{\epsilon} = \hat{\sigma}_{\pm} \\ 132 \text{ kHz} & \text{when } \hat{\epsilon} = \hat{\beta}. \end{cases} \quad (4.12)$$

This result is ~ 100 times larger than the differential second-order Stark shift for the same parameters. Comparing the fourth and second-order expressions, we find that $\delta\omega^{(4)}/\delta\omega^{(2)} \propto g_0^2/(\omega_{HF}\delta)$, clearly defining the regime where the fourth-order shift dominates. The second-order shift only becomes larger with a hundred-fold reduction in the laser intensity, corresponding to an applied shift below 10 Hz. Since the differential fourth-order shift can easily be made large as shown above, it is a practical means to control a large number of qubits.

4.2 Experimental Setup

The laser used to generate the fourth-order Stark shift is the same mode-locked, tripled, ND:YVO₄ used for coherent manipulation of the qubit (see section

3.1.4). The optical access of our current vacuum chamber restricts the polarization of the Stark shifting beam since the magnetic field is orthogonal to all viewports, prohibiting the use of pure σ_{\pm} light. However, as discussed earlier, the differential fourth-order Stark shift has two possible polarizations with large shifts for a single beam: the first is pure σ_{\pm} , the second is $\hat{\epsilon} = \hat{\beta} \equiv 1/2\hat{\sigma}_{-} + 1/\sqrt{2}\hat{\pi} + 1/2\hat{\sigma}_{+}$. We use the $\hat{\beta}$ polarization which slightly reduces the maximum shifts applicable, but does not require pure σ_{\pm} .

The small spot size required to individually apply a shift to each qubit is achieved by using the imaging objective designed for qubit state readout. Since the cycling transition of $^{171}\text{Yb}^{+}$ is 369 nm and the center wavelength of the modelocked laser is 355 nm, we use a Semrock dichroic beam combiner (LP02-355RU-25) for separating the 355 nm laser from the resonant light at 369 nm (Fig. 4.2). Guided by simulations of the optical system in the commercial ray-tracing software, Zemax [80], we focus the 355 nm light down to a less than 3 μm horizontal waist using an objective lens with a 0.23 numerical aperture.

In order to address each ion in a chain of up to 10 sites, we use an acousto-optical deflector (AOD, Brimrose CQD-225-150-355). Since the AOD is not imaged, it maps the rf drive frequency to ion position and the rf power of that drive frequency to the applied intensity. The rf control is implemented using an arbitrary waveform generator (AWG, Agilent M8109A), because it allows precise, easy, and arbitrary control while being easily reconfigurable. The differential fourth-order Stark shift is a direct change in the energy splitting of the qubit, so unlike in stimulated Raman processes, phase coherence does not require optical phase stability or even rf

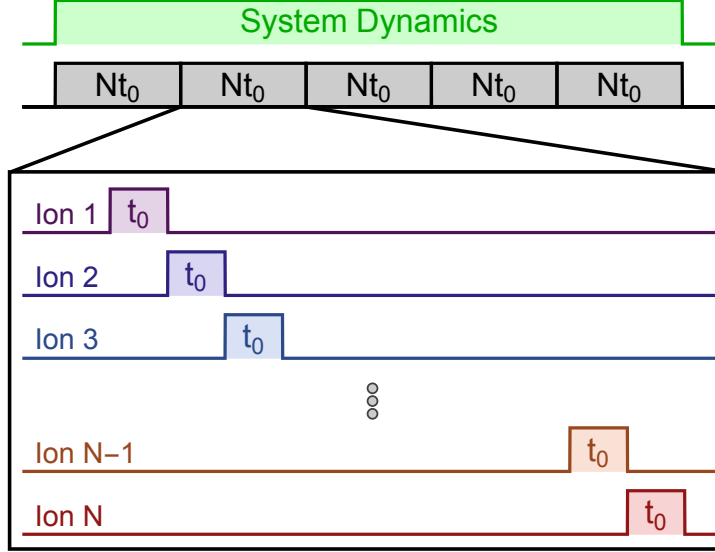


Figure 4.3: Sketch of a typical raster pulse sequence. When the light is evenly distributed across N ions, the applied fourth-order stark shift diminishes by $1/N^2$ due to the quadratic dependence on intensity. We recover a linear dependence on ion number by rastering the beam, or applying a large shift for a short time, t_0 sequentially to the ions. As long as each pulse chapter of length Nt_0 is much shorter than the interaction time-scale, then the shift on each ion is then proportional to $1/N$.

phase stability, but only depends on the integrated time-averaged intensity. Thus phase-coherent control only requires timing resolution better than the period of the differential fourth-order Stark shift, which is easily achieved with the AWG. The AWG also allows the application of many frequencies to the AOD, which will Stark shift multiple ions simultaneously. Additionally, the AWG gives arbitrary amplitude control of each frequency, providing time-dependent amplitude modulation of the four photon Stark shift.

Due to the quadratic dependence of the differential fourth-order Stark shift on intensity, when we divide the optical power across N ions, each ion's fourth-order

Stark shift is diminished by a factor N^2 ,

$$\delta\omega^{(4)}(ion) = \max(\delta\omega^{(4)})/N^2. \quad (4.13)$$

In order to recover a linear dependence, we “raster”, or rapidly sweep, the beam position from site to site across the chain. If this rastering occurs much faster than the dynamics of the system, then the effective fourth-order shift can be safely time-averaged, yielding

$$\delta\omega^{(4)}(ion) = \max(\delta\omega^{(4)})\frac{mt_0}{T} \quad (4.14)$$

where m is the number of raster cycles in the total elapsed time T and t_0 is the time the light is applied to each ion in a single cycle. In order for the raster to be fast enough to justify averaging the Stark shift, the length of each raster cycle, Nt_0 , must be small compared to the total elapsed time $T = Nmt_0$. We assume that any time where the beam is not hitting any of the ions during a raster cycle is small compared compared to the raster cycle duration and can be neglected. Substituting into Eq. 4.14,

$$\delta\omega^{(4)}(ion) = \max(\delta\omega^{(4)})\frac{1}{N} \quad (4.15)$$

which recovers a linear dependence on the system size. In Fig. 4.3, we show a diagram of an example raster sequence. The limitation on this technique is how small t_0 can be made. In our case, t_0 is limited by the rise time of the AOD, which is approximately 50 ns, which is still fast compared to $N/\delta\omega^{(4)}$ and very fast when

compared to a mechanical deflector rise time.

4.3 Experimental Demonstration

Using Ramsey spectroscopy [81], we measure the total Stark shift on the qubit splitting from the applied light. A quadratic dependence on the intensity distinguishes the fourth-order Stark shift from the typical linear dependence of the second-order AC Stark shift (Eq. 4.11). By measuring the total shift as a function of applied time-averaged optical power, the data in Fig. 4.4a demonstrates that the observed shift is consistent with the \bar{I}^2 dependence of the fourth-order Stark shift.

By translating the ion through the beam, we measure the horizontal beam waist by fitting the resulting Stark shift to the square of a Gaussian distribution (Fig. 4.4b):

$$\delta\omega^{(4)}(\Delta x) = \delta\omega^{(4)}(0) \left(e^{-2\Delta x^2/\sigma^2} \right)^2. \quad (4.16)$$

We measure the horizontal waist to be $\sigma = 2.68 \pm 0.03 \text{ } \mu\text{m}$. This small waist allows for independent control of qubits. In Fig. 4.5a, we show how qubit 5 can be driven in a ten ion system with only minimal crosstalk of approximately 2% on the adjacent spins (ions 4 and 6). In this configuration, the ions are separated by 2.76 and 2.64 μm respectively. By increasing the distance between ions, we can decrease the crosstalk on adjacent spins. For example, in a system of two spins separated by 7 μm , we individually drive each ion with the cross-talk $\leq 2 \times 10^{-5}$ over a time $t = 30 \times 2\pi/\delta\omega^{(4)}$.

As indicated above, the rf drive frequency maps to position at the ion chain,

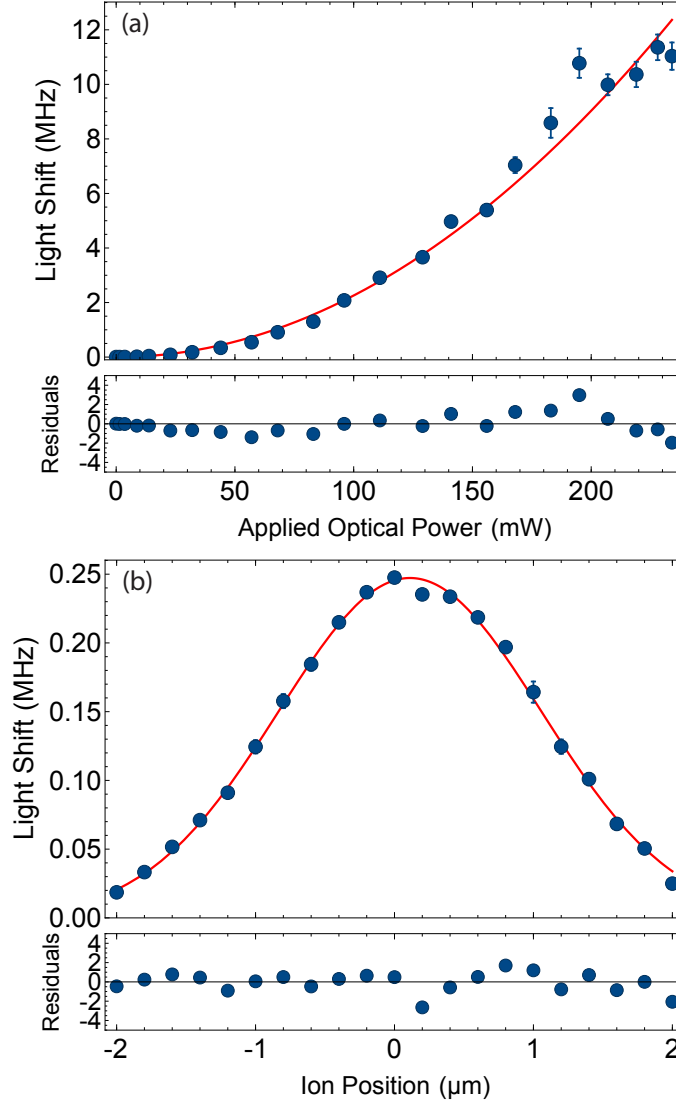


Figure 4.4: Measured Stark shifts as a function of optical power and position. Measured fourth-order Stark shift as a function of optical power with fit residuals (a). We fit the measured light shift as a function of optical power to Eq. 4.11 for $\hat{\epsilon} = \hat{\beta}$ taking into account an astigmatism of the imaging optics resulting in the vertical waist being ~ 1.5 times the horizontal and find very good agreement showing that the light shift arises from the fourth-order Stark shift. Measurement of the beam waist at the ion with fit residuals (b). By translating the ion through the beam with a fixed applied optical power of 40 mW, we extract the horizontal optical waist at the ion. We found this to be $2.68 \mu\text{m}$.

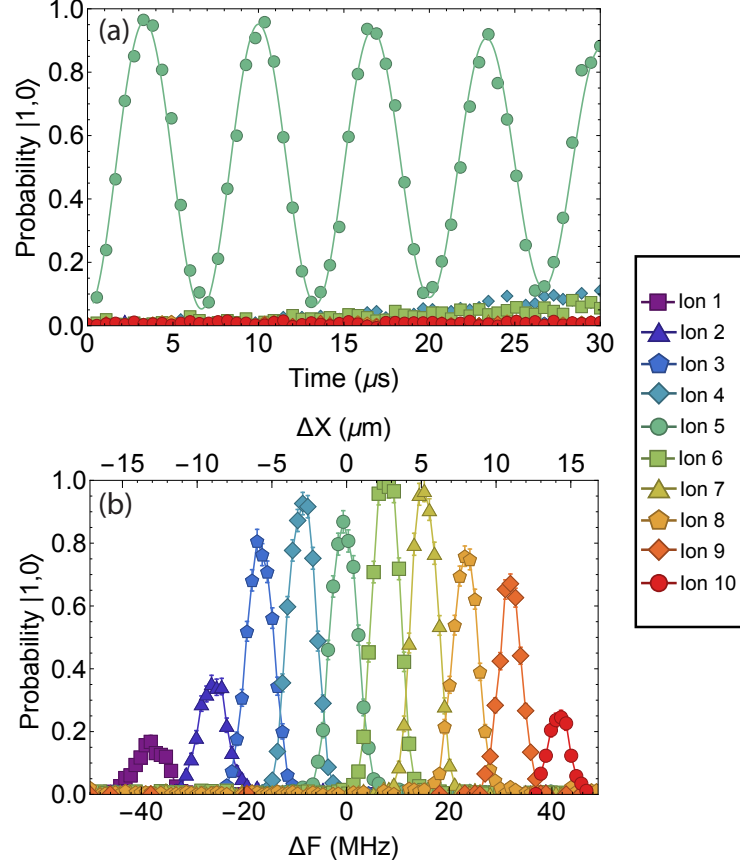


Figure 4.5: Resolution of individual addressing beam. Observed crosstalk of beam applied to one ion (a). By applying light to only ion 5 in a chain of 10, we measure the crosstalk on the nearest neighbors, ion 4 and 6, to be only 2%, which is consistent with our measured horizontal beam waist and the ion separation. Solid line is a fit to an exponential decaying oscillation with decay parameter $\tau = 133\mu\text{s}$, which is a 2% error per π -pulse. Individual ion signal as the beam is swept over a chain of ten ions (b). By scanning the AOD drive frequency for a fixed power and duration, we map the fourth-order Stark shift as a function of drive frequency. This corresponds to a displacement of beam position at the ion chain. The effective scanning range of the AOD is approximately $30\text{ }\mu\text{m}$.

while the small spot size allows for individual control of the ions. In Fig. 4.5b, we show this mapping in a chain of ten ions by scanning the drive frequency of the AOD while fixing the rf power and time. The difference in the applied fourth-order Stark shift of each ion is due to the rf bandwidth of the AOD, since the diffraction efficiency is lower at the extremes of the bandwidth. In the current optical setup, a change of 10 MHz to the drive frequency corresponds to a displacement of approximately 3.4 μm along the ion chain.

This control enables the preparation of arbitrary, high-fidelity product states when the individual addressing beam is used in conjunction with global qubit operations from the Raman beams. In Fig. 4.6, we illustrate a pulse sequence used to generate a product state. This method, effectively a Ramsey sequence, is used to prepare a spatially-alternating spin state, which is the most difficult state to produce since it is the most susceptible to crosstalk. We observe a fidelity of $87 \pm 1\%$ for the desired state, which includes all state preparation and measurement (SPAM) errors. This fidelity is consistent with a 2% error of the π -pulses on five of the ions arising from the intensity noise and the small inter-ion crosstalk of the individual addressing beam, and some residual infidelity stemming from the off-resonant coupling of the ground states and the ion detection error.

Two features of the experimental noise should be noted. The first stems from the quadratic nature of the fourth-order light shift. This quadratic dependence on the intensity doubles the fractional uncertainty in the light shift relative to small amplitude noise in the laser intensity. The second arises from the off-resonant coupling of levels in the ground state manifold. This off-resonant coupling leads to effective

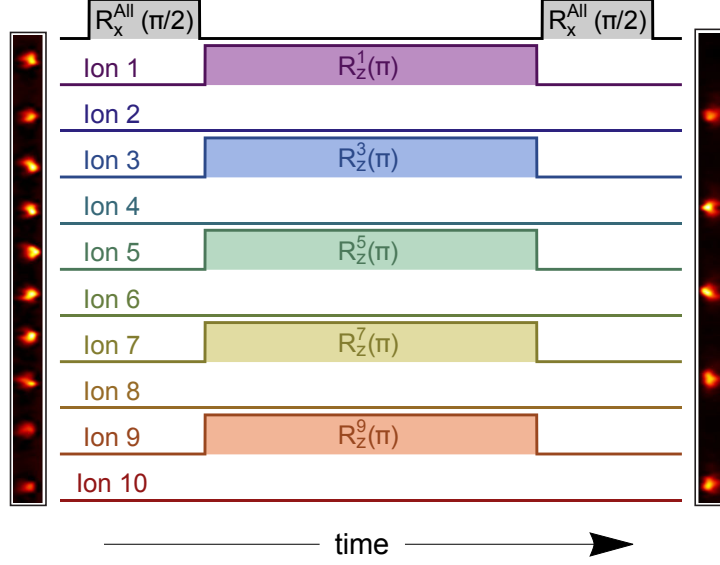


Figure 4.6: Pulse sequence for preparing a string of 10 ions in a staggered spin configuration. All 10 ions are prepared in $|0,0\rangle$ and then a global $\pi/2$ pulse is applied. Depending on the state being prepared, some number of the ions have a π phase shift applied, creating the desired configuration. A final global $\pi/2$ pulse projects the configuration back into qubit basis, completing the effective Ramsey sequence.

Rabi dynamics that results in a mixture of the qubit states and the coupled states that is $\sim \frac{1}{2}\Omega_{n,a}^2/(\delta_{n,a}^2 + \Omega_{n,a}^2)$. In the experiment, light shifts of order 5 MHz are therefore expected to mix qubit state and the coupled state up to 20%. Mixing the states together is effectively dissipation, causing decoherence of the spin. For this reason, during coherent operations we restrict the shift size to < 300 kHz, where this mixture is less than 2.5% the qubit population.

The primary limitation in the current apparatus is the intensity applied to each ion, especially those on the edge of the chain due to the bandwidth of the AOD. The maximum intensity on each ion is simply

$$I_{ion} = \frac{2\pi\bar{P}(\text{NA})^2}{\lambda^2} DE_\nu \quad (4.17)$$

where \bar{P} is the time-averaged power into the AOD, NA is the objective numerical aperture, λ is the wavelength of the light, DE_ν is the diffraction efficiency of the AOD at the drive frequency, ν , corresponding to the ion position. By enlarging the NA of the objective lens, the intensity applied to each ion would greatly increase while simultaneously lowering the inter-ion crosstalk. Further, improving the diffraction efficiency and bandwidth of the AOD will allow more ions to be addressed. By implementing changes on both of these elements, we should be able to address 20+ ions without difficulty.

4.4 Applications of the Fourth-order Stark Shift

The freedom and control afforded by an individually addressed, Stark-shifting beam opens many possibilities that were previously inaccessible to clock state qubits. One such new application is that we can now apply site dependent transverse magnetic fields to an interacting Ising spin system [40]. Since the strength of each field is controlled by the rf amplitude from the AWG, we are able to quickly generate hundreds of different random instances of individual ion fields in a reproducible way. Schematic representations are shown in Fig. 4.7.

We have also developed techniques for the individual resolution of ions when the ion spacing is smaller than the beam waist. The Ramsey method technique described in section 4.3 for the preparation of arbitrary product states works well if the light has very little overlap on the other spins. Yet when the ion separation is of the order of the beam waist, crosstalk significantly perturbs the other ions, reducing

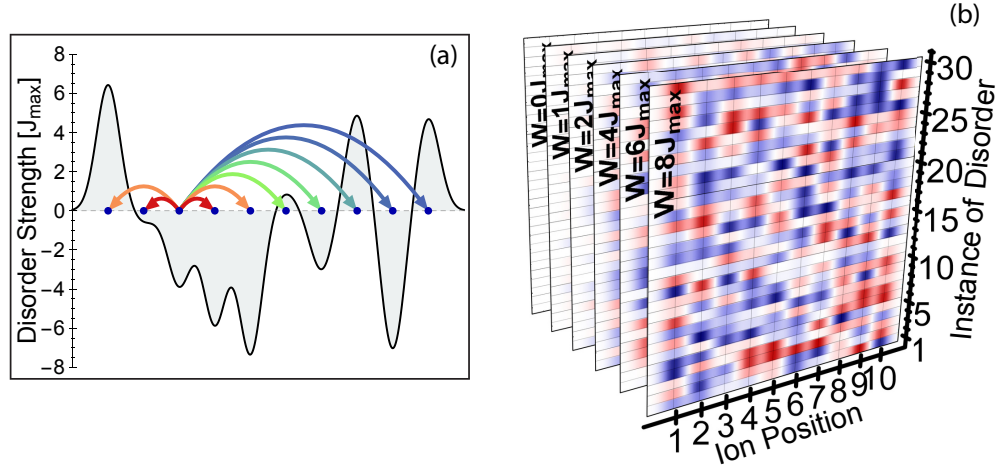


Figure 4.7: Fourth-order Stark shift used to generate disorder. Schematic of one particular instance of disorder (a). Each blue dot represents an ion while the black line is a representation of the applied field. By controlling the rf frequency and amplitude applied to the AOD, we can “paint” an arbitrary potential onto the ion chain. Since these individual fields are controlled by a computer, the strength and configuration can be easily manipulated. Representation of all instances experimentally realized (b). Here we show an intensity plot where each panel is a particular disorder strength, row is a particular instance of disorder, each column is the ion position and the color represents the strength of the potential. We experimentally realized over 150 unique instances of disorder using the individually addressed fourth-order Stark shift beam.

the fidelity of the desired state. In order to implement arbitrary state preparation in an ion chain where the ions are closer together than the beam waist, we utilize a different technique of single rotation known as the Rabi method (see Fig. 4.8). In the Rabi method, we first initialize all spins in $|0, 0\rangle$ and a large fourth-order Stark shift is applied to all ions except the ones to be rotated. We then drive a π pulse with a weak global carrier at the normal ω_{HF} . All the ions with the large Stark shift are unaffected since the carrier is off-resonant, while the unshifted ions go from $|0, 0\rangle$ to $|1, 0\rangle$, generating the desired product state.

While both methods are useful for state preparation, only the Ramsey method is used for analysis rotations because, in the Rabi method, the other spins undergo a rotation around σ_z while the unshifted spins are flipped. This rotation could leave an additional unwanted relative phase in the measurement, unless the Stark shift was applied for exactly an integer 2π time. This is difficult due to small fluctuation in the Stark shift, making the Rabi method undesirable for analysis.

Another technique realized with this fourth-order Stark shift beam has been the direct measurement of the J_{ij} coupling matrix. Previously, we have reconstructed a coupling matrix by using spectroscopic techniques [46], but with the individual control afforded by this fourth-order Stark shift, we can now directly measure the coupling between an arbitrary pair of ions. The procedure is similar to the Rabi method for arbitrary state preparation. After all spins are initialized in $|0, 0\rangle$ or $|\downarrow\rangle$, the two spins k and l whose coupling are to be measured have a large Stark shift applied while the rest of the spins do not. We then use a global Raman transition to drive all the unshifted ions to one of the Zeeman levels in the

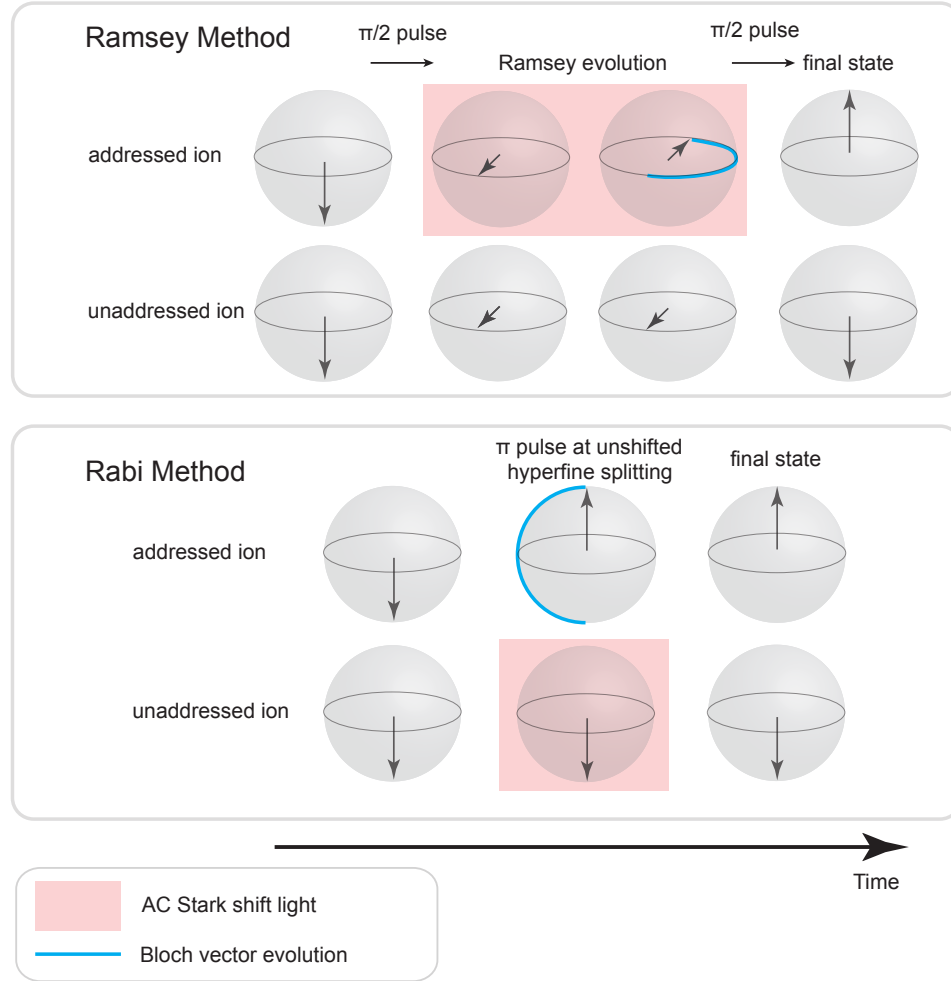


Figure 4.8: Schematic of individual rotation types. Upper panel is a Bloch sphere representation of the type of rotation described in section 4.3 called the Ramsey method. This method is ideal for both state preparation and analysis since the phases of the unaddressed spins are unmodified. The lower panel shows what we call the Rabi method where the unaddressed ions are shifted out of resonance while a weak carrier rotates the unshifted spins. This method is used for state preparation when the ion spacing is smaller than the beam waist.

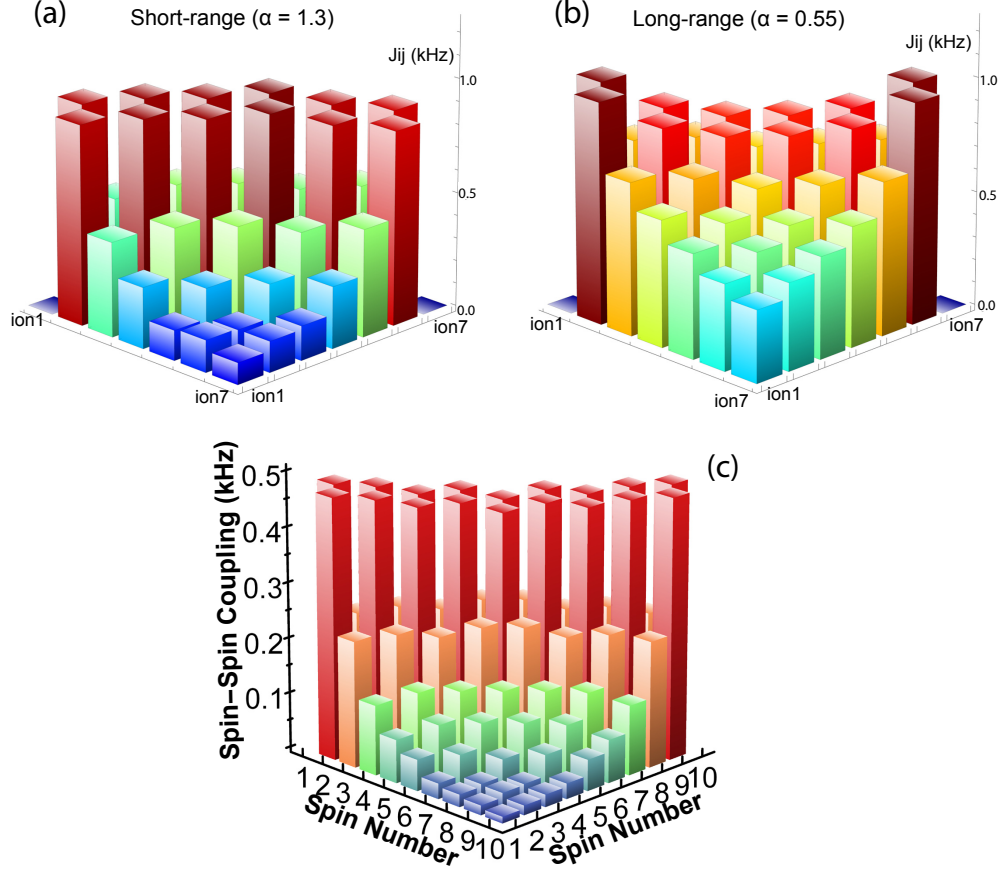


Figure 4.9: Measured J_{ij} couplings for 7 and 10 ions. Using the individual addressing beam, all but two spins are driven to one of the ground state manifold Zeeman states and the two remaining spins are evolved with a M-S interaction, oscillating between $|\downarrow\downarrow\rangle$ and $|\uparrow\uparrow\rangle$. The oscillation frequency corresponds to the interaction strength and is used to reconstruct the coupling matrix for 7 spins with an $\alpha = 1.3$ (a) and an $\alpha = 0.55$ (b). We also reconstruct a 10 ion coupling matrix with an $\alpha = 1.13$ (c).

ground state manifold, namely $|1, \pm 1\rangle$. Afterwards, a M-S interaction is applied which induces coherent oscillations between $|\downarrow\rangle_k |\downarrow\rangle_l$ and $|\uparrow\rangle_k |\uparrow\rangle_l$ for only the ions k and l since the Zeeman lines are not coupled by the M-S interaction, leaving the rest of the ions alone. The frequency of this oscillation corresponds to the strength of the interaction between the two ions and is extracted by fitting to the measured populations.

This has been used to precisely measure the coupling matrix of seven ions

under two very different ranges, namely a short-range matrix with $\alpha = 1.3$ (Fig. 4.9a) and a long-range matrix with $\alpha = 0.55$ (Fig. 4.9b). The measured matrices show good agreement with the predicted couplings and even capture the nearest-neighbor coupling asymmetry across the chain. These J_{ij} couplings are the very couplings used to study a failure in quantum thermalization discussed in chapter 6. We even made a similar measurement in a system of ten ions with a range of $\alpha \sim 1.13$ (Fig. 4.9c). This measurement highlights that the interaction graph is really long-ranged in a ten spin system, coupling even ions 1 & 10. The long-ranged character of the couplings is important because it prevents the Hamiltonian discussed in [40] from being mapped to non-interacting Fermions, allowing for the realization of a many-body localized state.

Finally, this individual addressing beam using the fourth-order Stark shift enables dynamic individual control, allowing for the simulation of interesting systems such as loops with non-zero magnetic flux [82], the dynamics of lattice gauge theories [83], or even the realization of a new kind of quantum system [84]. The fourth-order Stark shift has added a new and very powerful tool to our quantum simulator toolbox.

Chapter 5: Entanglement in Large N System

As our quantum simulation system size grows, an ever present problem is the verification and validation of the results. This problem can be broken into different questions, one of which is, “How quantum is the system?” This question is highly non-trivial to answer. In fact, large systems that have pursued quantum information with a “top-down” approach are seeking to prove that their results are quantum in origin [26, 85–87] and that these quantum processes result in a quantum advantage [88, 89]. On the other hand, a “bottom-up” approach to quantum systems begins with small systems which can be verified classically [28–30, 34–36, 90] and seeks to increase the system size while maintaining the “quantumness” and confirming the dynamics. While confirming the dynamics of a system that cannot be classically simulated is a very difficult problem, a good approximation is achieved by measuring the imposed Hamiltonian. Verifications of an imposed Hamiltonian have been shown that do not require an exponential number of measurements [46, 91], ensuring that the dynamics are those believed to be applied. In conjunction with this, a full verification of a quantum system requires that the system itself has not undergone decoherence. One possibility to measure this decoherence is to measure the amount of entanglement in the system, verifying that noise has not destroyed

this quintessential quantum phenomenon.

Entanglement of a large system is itself difficult to measure. The most direct measure of entanglement is to reconstruct the density matrix of the system. Despite density matrix reconstruction having been performed on up to 8 spins [92] in trapped ions and small systems in photonic bits [93], complete reconstruction quickly becomes intractable as it takes $\sim 3^N$ measurements for an N spin system. Thus measurement of entanglement needs to be reduced to some observable which does not require density matrix reconstruction, but is experimentally accessible. This has led to a variety of methods [94] proposed to measure entanglement in a variety of systems. Some of these methods use a copy of the system to extract the entanglement [36, 95] while others use algorithms to extract the highest probable density matrix from an incomplete measurement set [96–98]. Witnesses constructed for specific types of entanglement have also been successfully used in medium system sizes [99, 100], yet witnesses of this kind are generally very sensitive to experimental noise and give only a binary answer of entangled or unknown. Ideally, in order to act as a useful diagnostic, the measurement should somehow quantify the amount of entanglement present in the system.

5.1 Spin Squeezing

One observable which is shown to quantify the entanglement is spin squeezing [101, 102]. Spin squeezing was originally a quantization of the metrological advantage gained from an entangled quantum many-body system over the standard quantum

limit of phase resolution. Ultra-cold atomic systems have leveraged their control in order to achieve observed metrological gains of up to 100 times the standard quantum limit [103, 104]. This metrological gain can also be used to as a way to quantify the k -particle entanglement [105]. Here k -particle entanglement is defined as a state of N particles which cannot be decomposed into a convex sum of products of density matrices with all density matrices involving less than k -particles, namely one of the terms must be a k -particle entangled density matrix. The metrological gain in the ultra-cold atom experiments is equivalent to the entanglement of $< 1\%$ of the atoms in the cloud.

While quantum metrology holds great promise for high precision measurement, spin squeezing also offers an experimentally realizable means of characterizing a qubit system. Initial experiments in trapped ion qubits have had some success in demonstrating metrological gain [106] as well as an entanglement of $\sim 5\%$ of the system. Here we will measure the spin squeezing in a large well controlled qubit system which is used for quantum simulation.

The Hamiltonian we apply is a long-ranged transverse field Ising model,

$$\mathcal{H} = \sum_{i,j} J_{ij} \sigma_x^i \sigma_x^j + B \sum_i \sigma_z^i. \quad (5.1)$$

The experiment initializes all spins down, parallel to the transverse field and then the Hamiltonian in Eq. 5.1 is applied. Since the amount of squeezing is improved with longer range interactions, we set $\alpha = 0.74$. The applied transverse field is $B = 2.5J_{max}$. The specific value of B is chosen to balance the sensitivity of the

measurement to spin depolarization due experimental noise and spin dynamics while keeping the largest possible k -particle entanglement. By measuring the spin projections along both \hat{x} and \hat{z} , we can then construct the observables of $\langle S_z \rangle = \sum_i \langle \sigma_z^i \rangle$ and $\Delta S_x^2 = \sum_{i,j} \langle \sigma_x^i \sigma_x^j \rangle - \langle \sigma_x^i \rangle \langle \sigma_x^j \rangle$ required by the Ramsey squeezing parameter, defined as [101]

$$\xi_R^2 = \frac{N \Delta S_x^2}{\langle S_z \rangle^2}. \quad (5.2)$$

In Fig. 5.1a, we show the Ramsey squeezing parameter as a function of time for one of the largest qubit systems to date, 24 ions. The largest squeezing observed is -2.84 ± 0.16 dB as compared to the initial product state. While the measurement enhancement is not large due to the relatively small system size as compared to 5×10^5 , it still demonstrates significant entanglement. The amount of entanglement can be quantified using k -particle entanglement curves generated following [105]. This comparison is shown in Fig. 5.1b demonstrating 4-particle entanglement. Thus our data is consistent with 17% of the entire system being entangled, which is much larger than comparable experiments.

While four out of twenty-four is only a small portion of the system, numerics only predict a maximal entanglement of 10 spins [107]. We believe that the large disparity between the measured k -particle entanglement and the predicted value is largely due to measurement error, particularly inter-ion crosstalk. With larger ion numbers, the ions in the middle of the chain are pushed closer together, exacerbating the issue of ion PSF function overlap. While this cross-talk is only a couple percent, the variance is computed using individually resolved camera images where this ion

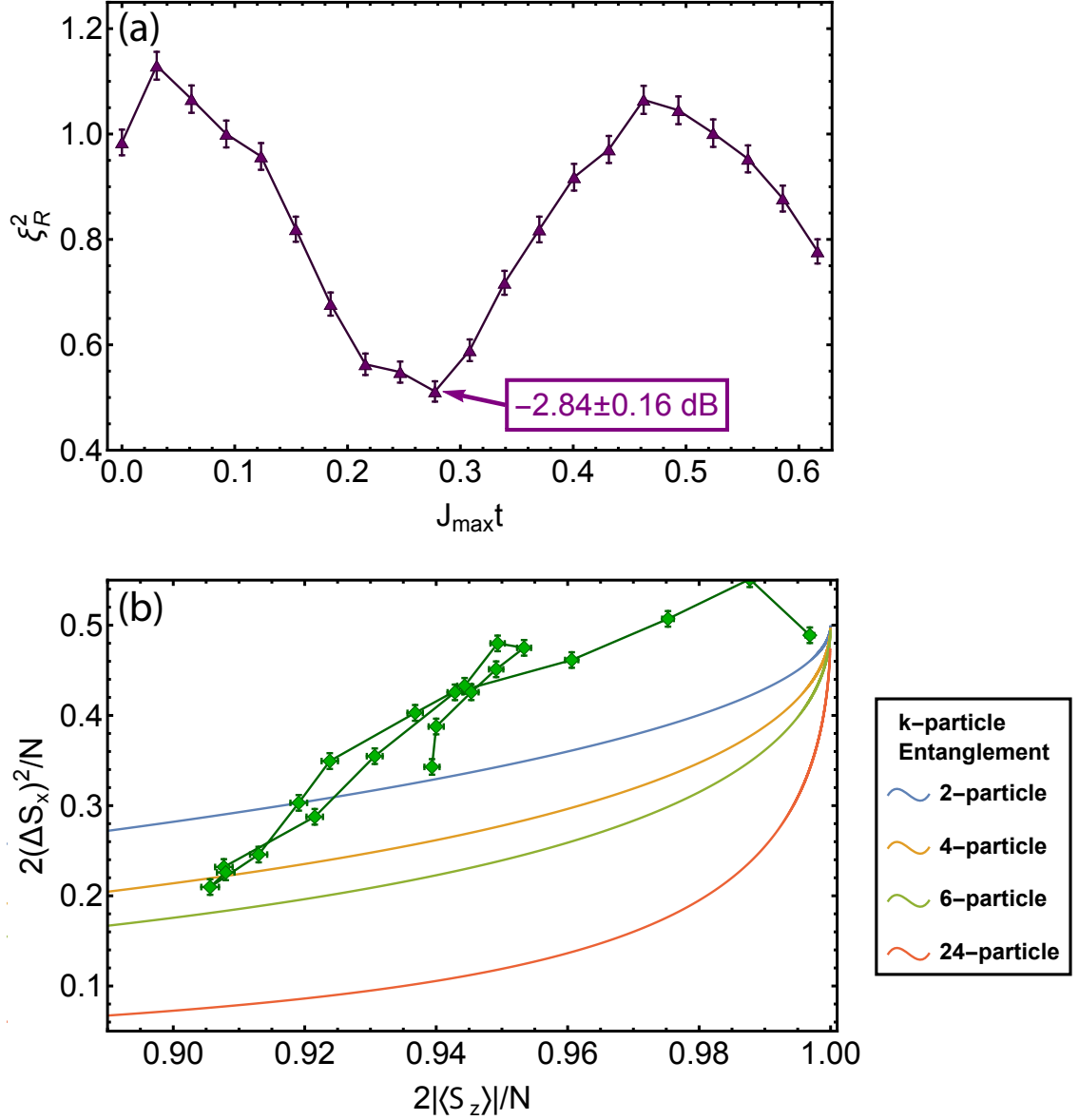


Figure 5.1: Measurement of spin squeezing in 24 ions. Computed Ramsey spin squeezing parameter ξ_R^2 from 24 spins (a). Maximum observed squeezing is -2.84 ± 0.16 dB. While this is small compared to ultra-cold atomic experiments, the system size here is also significantly smaller. Also shown is ΔS_x^2 as a function of $|\langle S_z \rangle|$ (b). Curves of k -particle entanglement are generated from [105]. Data has a maximal entanglement of four-particle entanglement. While the amount of entanglement is not large, theory only predicts a maximum of 10-particle entanglement and our measurement is consistent with $\sim 17\%$ of the entire system entangled which is larger than comparable experiments by an order of magnitude.

cross-talk creates false correlations which systematically bias the variance larger than it is. We believe that this also explains the small increase in the variance at the second time step. This could be improved by instead using global measurements and no longer discriminating individual spin states, but that would also sacrifice the computational advantage of the quantum simulator. By improving our imaging objective to a higher NA, we believe that this systematic can be eliminated even in large chains, allowing for even deeper squeezing.

5.2 Quantum Fisher Information

Another promising witness of entanglement is the Quantum Fisher Information (QFI) which has recently been shown to witness genuine multi-partite entanglement [108, 109]. Genuine multi-partite entangled pure states are defined as those that cannot be created without participation of all spins. In other words, a density matrix ρ of N subsystems is genuinely multi-partite entangled if and only if it does not admit any bipartite decomposition. Namely if $\rho^{(k)}$ is an irreducible density matrix of k subsystems, then ρ is only genuinely multi-partite entangled if

$$\rho \neq \rho^{(k)} \otimes \rho^{(N-k)} \quad \forall k. \quad (5.3)$$

From a quantum metrology perspective, the QFI quantifies the sensitivity of a given input state to a unitary transformation $e^{i\vartheta\hat{\mathcal{O}}}$ generated by the Hermitian operator $\hat{\mathcal{O}}$. Interestingly, the QFI reveals useful entanglement even in the case of non-Gaussian spin states where the spin squeezing witness ξ_R does not [110].

5.2.1 Directional QFI

For a pure state, the QFI for a linear local operator $\hat{\mathcal{O}}$ reduces to the variance of that operator:

$$F_Q = 4(\Delta\hat{\mathcal{O}})^2 = 4(\langle\hat{\mathcal{O}}^2\rangle - \langle\hat{\mathcal{O}}\rangle^2). \quad (5.4)$$

For a mixed state, the expression is more complicated, but this case will be discussed later. A direct link can now be drawn between ξ_R and F_Q by the relation $F_Q/N \geq 1/\xi_R^2$ [110]. For states which can be fully characterized by their variance, $F_Q/N \approx 1/\xi_R^2$ but as a state becomes less Gaussian, F_Q continues to indicate entanglement while ξ_R no longer does. In addition to the witness of genuine multi-partite entanglement, there are also bounds on the QFI which determine the k -particle entanglement present. If we write the QFI of a specific k -producible state of N ions ρ_k with the observable $\hat{\mathcal{O}}$ as $F_Q[\rho_k, \hat{\mathcal{O}}]$, then the QFI must satisfy the following inequality [108, 109]

$$F_Q[\rho_k, \hat{\mathcal{O}}] \leq sk^2 + r^2 \quad (5.5)$$

where $s = \lfloor \frac{N}{k} \rfloor$ is the largest integer smaller than or equal to $\frac{N}{k}$ and $r = N - sk$. Thus, if the QFI violates the bound in Eq. 5.5, then there must be at least $(k+1)$ -particle entanglement. Computing this bound for $k=1$, we see that $F_Q > N \Rightarrow f_Q \equiv F_Q/N > 1$ in order for there to be at least bi-partite entanglement. It is also clear that maximum possible value for f_Q is to have N -partite entanglement in a system of N spins, meaning that $f_Q \leq N$.

Let us see an example by assigning $\hat{\mathcal{O}} \equiv S_z = \sum_i^N \sigma_z^i$ and ρ to be a product

state along the \hat{x} direction of the Bloch sphere. If we compute the QFI, we find that $f_Q[\rho, S_z] = 1$, saturating the unentangled bound. If ρ was instead a product state all along \hat{z} , then $f_Q[\rho, S_z] = 0$ indicating that the direction we probe the state with the QFI matters. This is further emphasized by instead letting ρ_{GHZ} be a GHZ state in the \hat{z} direction, namely a superposition of all spins up in \hat{z} and all spins down in \hat{z} . If we compute the QFI in each direction of the Bloch sphere, we can use the results to generate a vector $\vec{f}_Q[\rho] = \{f_Q[\rho, S_x], f_Q[\rho, S_y], f_Q[\rho, S_z]\}$. Applying this to the GHZ state:

$$\vec{f}_Q[\rho_{GHZ}] = \{1, 1, N\} \quad (5.6)$$

Since F_Q is tied directly to metrological advantage, it is clear that there is a huge gain in the \hat{z} direction while not nearly as much in the other two directions. This implies that there is more information gained when looking in all three directions as opposed to just one.

5.2.2 Total QFI

In fact, the bounds of k -particle entanglement can be recomputed in the context of measuring in all three directions. Let a new quantity be defined which is just the sum of the QFI in each direction of the Bloch sphere:

$$\bar{f}_Q[\rho] = \sum_l f_Q[\rho, \hat{O}_l] \quad (5.7)$$

where $l \in x, y, z$. The new bound for a k -producible state of N ions ρ_k with a linear local observable $\overline{\mathcal{O}}$ is [108, 109]:

$$\overline{f}_Q[\rho_k] \leq \frac{1}{N} [s(k^2 + 2k - \delta_{k,1}) + r^2 + 2r - \delta_{r,1}] \quad (5.8)$$

where as before $s = \lfloor \frac{N}{k} \rfloor$ is the largest integer smaller than or equal to $\frac{N}{k}$, $r = N - sk$ and now $\delta_{a,b}$ is the Kronecker delta-function. For a separable state, the max value of $\overline{f}_Q = 2$ while the maximal value of any quantum state is $\overline{f}_Q \leq N + 2$.

Now we can revisit the example discussed above, namely a product state along the \hat{x} direction where $\hat{\mathcal{O}} = \vec{S}$, which gives a total QFI of $\overline{f}_Q = 2$, saturating the separable state bound. This also gives more information about the entanglement of the system when looking at the GHZ state in the \hat{z} direction ρ_{GHZ} , namely $\overline{f}_Q = N+2$ which saturates the maximal QFI bound. While the GHZ state saturates both f_Q and \overline{f}_Q , there are genuinely multi-partite entangled states which are not detected by f_Q . One such example is ρ_{D_z} which is a Dicke state with $N/2$ excitations and is fully symmetric and an eigenstate of \hat{J}_z . If we write out the QFI vector $\vec{f}_Q[\rho_{D_z}] = \{\frac{N+2}{2}, \frac{N+2}{2}, 0\}$, where none of the f_Q demonstrate genuine multi-partite entanglement, but only partial k -particle entanglement. Whereas, it is clear that if we instead examine \overline{f}_Q , we find genuine multi-particle entanglement.

So far, everything stated has been in the context of pure states. When the measured state is a mixed state, the form of the QFI itself changes. In general, for a given density matrix $\rho = \sum_k \lambda_k |k\rangle \langle k|$, the QFI is then just $F_Q[\rho, S_{\hat{n}}] = \hat{n}^T \Gamma_C \hat{n}$

where Γ_C is a matrix defined by

$$[\Gamma_C]_{ij} = 2 \sum_{l,m} (\lambda_l + \lambda_m) \left(\frac{\lambda_l - \lambda_m}{\lambda_l + \lambda_m} \right)^2 \langle l | S_i | m \rangle \langle m | S_j | l \rangle. \quad (5.9)$$

This general statement requires knowledge of the density matrix of the state in question, which of course takes us back to full tomography. Yet for pure states this statement reduces to exactly $[\Gamma_C]_{ij} = \langle S_i S_j + S_j S_i \rangle / 2 - \langle S_i \rangle \langle S_j \rangle$ [111] which is just the variance of S .

Further, the QFI is convex in the state, namely $f_Q[p_1 \rho_1 + p_2 \rho_2, S_l] \leq p_1 f_Q[\rho_1, S_l] + p_2 f_Q[\rho_2, S_l]$. This implies that by computing the QFI for a pure state from a mixed state measurement, you may be over estimating the actual size of the QFI and thus the entanglement depth in the system. While this is true generally, there is a case where the inequality can be rewritten as an equality. Here we define a mixed state ρ_m as the following:

$$\rho_m = p\rho + (1-p)\frac{\mathbb{1}}{2^N}. \quad (5.10)$$

This particular mixed state reduces to a very simple expression for the QFI by evaluating Eq. 5.9 [109], which can be written as

$$f_Q[\rho_m, S_l] = \frac{p^2}{p + (1-p)2^{-(N-1)}} f_Q[\rho, S_l]. \quad (5.11)$$

For large N , this expression simplifies to $f_Q[\rho_m, S_l] \sim p f_Q[\rho, S_l]$. Despite this particular case, it is in general difficult to experimentally prove entanglement using the QFI based on the variance of the observable. Some experiments have mea-

sured the QFI without the pure state assumption [106, 112] by using a small angle approximation, but this technique is not generally applicable.

5.2.3 Measured QFI for 10 spins

While not proving demonstrable entanglement, the pure state QFI is still helpful in the diagnosis of quantum simulations. Here we will consider a simulation similar to that of [34] where the system is prepared in a product state of $|\uparrow\uparrow\cdots\uparrow\rangle_x$ and then quenched to the Hamiltonian

$$\mathcal{H} = \sum_{i,j} \frac{J_{ij}}{2} (\sigma_x^i \sigma_x^j + \sigma_y^i \sigma_y^j). \quad (5.12)$$

Previously we showed that the correlations in the \hat{x} direction violate the Lieb-Robinson bounds [113] when the interaction is sufficiently long-ranged. By repeating the quench experiment, yet also measuring in all three directions of the Bloch sphere, we can construct the pure state QFI for the system and estimate the entanglement in the system.

Using these measurements, we compute the total QFI $\overline{f_Q}$ for a system of 10 spins (see Fig. 5.2a). The measurement shows a quick growth of entanglement in the system, ending in a state consistent with 10-particle entanglement. Since the QFI is convex in the state, we compared our results to exact diagonalization of Eq. 5.12.

Examination of the results showed that the dynamics were very sensitive to small σ_z perturbations in the Hamiltonian. Due to small uncontrolled fourth-order

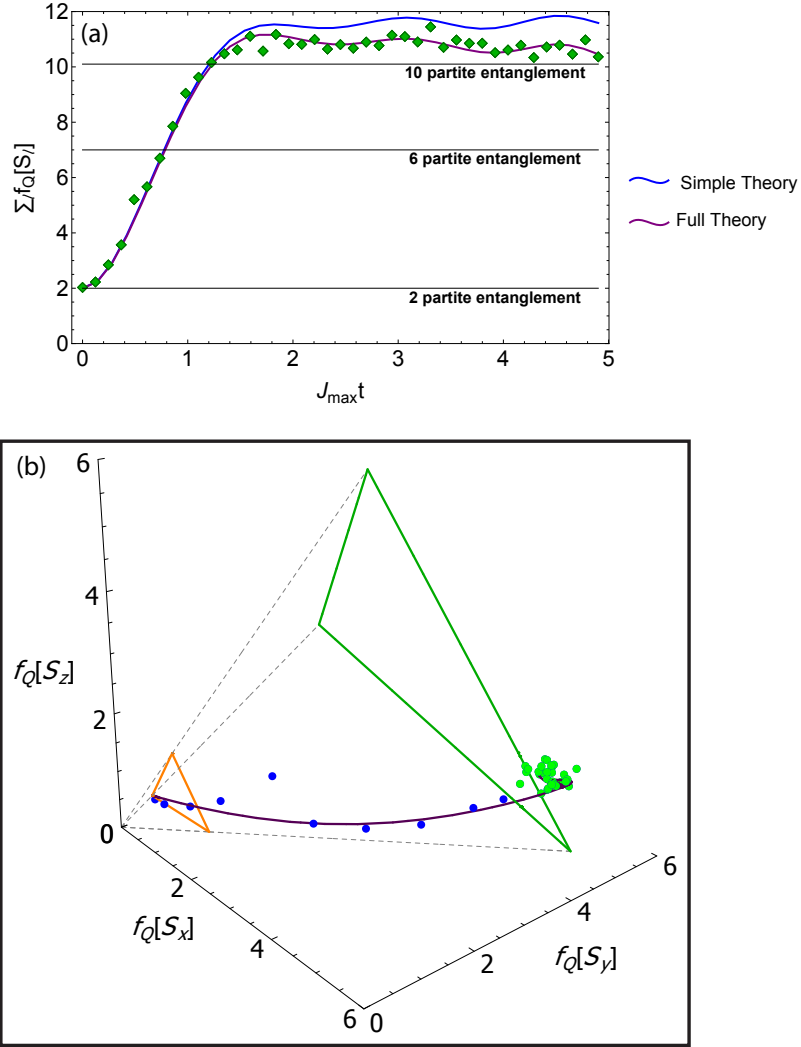


Figure 5.2: Measurement of QFI in 10 Spins. Plot of 10 ion \bar{f}_Q as a function of time (a). Here we see that measurements are consistent with the entirety of system being entangled at longer times. We compare the data to theory, first with no noise (blue line) and second with numerics which incorporate noisy J_{ij} along with spontaneous emission (purple line). Spontaneous emission appears to be the primary divergence of measured dynamics from the noiseless predictions. Statistical error bars of 1 s.d. are shown but smaller than point size. By plotting evolution of 10 ions through the QFI vector space (b), we show that the ten ion data is consistent in all three directions with predicted evolution (purple line) from full theory. System first starts in product state (orange plane) and quickly evolves to violate bound for 10-particle entanglement (green plane). Green points highlight data which violates 10-particle bound.

Stark shifts arising from the Raman lasers, σ_z perturbations are present in the simulation at approximately 15 Hz when the largest coupling strength is $J_{max}/2\pi = 167$ Hz. By incorporating this field into the numerics, we generate a simple model of the system which is shown in Fig. 5.2a as the blue line. While the data is consistent with the theory at short times, at longer times the data begins to diverge. Due to laser intensity noise of $\sim 2\%$, both the strength of J_{max} and the small uncontrolled fourth-order shift are noisy. Since this noise is small and slow compared to an experiment, we treated it perturbatively by assuming that it was constant for each experiment. Under this assumption, we generated a Hamiltonian where J_{ij} and the σ_z were scaled by a random number chosen from a normal distribution centered around J_{max} and 15 Hz respectively. The width of the normal distribution was set to $4\%J_{max}$ for J_{ij} and 15 Hz for the σ_z . We then solved the time-dependent Schroedinger equation for this Hamiltonian and computed the observables. This was then repeated 100 times and the observables were then averaged together.

Finally, we incorporated the effect of spontaneous emission into the model by assuming that the probability for an emission of a single photon per experiment was small enough that the dynamics would be largely unaffected. This allowed us to treat it as a measurement effect. In our system, since almost all of spontaneous emission is Raman, e.g. emits into a different state [67], and is twice as likely to decay into one of the Zeeman states which will project bright upon measurement, we modified the pauli-matrices in the computation of the spin observables to be the

following:

$$\begin{aligned}
\sigma_x[\epsilon] &= \begin{bmatrix} \epsilon & 1 - \epsilon \\ 1 & 0 \end{bmatrix} \\
\sigma_y[\epsilon] &= \begin{bmatrix} \epsilon & i(1 - \epsilon) \\ -i & 0 \end{bmatrix} \\
\sigma_z[\epsilon] &= \begin{bmatrix} 1 & \epsilon \\ 0 & -(1 - \epsilon) \end{bmatrix}
\end{aligned} \tag{5.13}$$

Using these modified Pauli-matrices, we computed the QFI where we plugged in $\gamma_{(p,|\{1,0\}\rangle)}$ found in section 3.2.2 to the probability of a single spontaneous emission, $1 - e^{-N\gamma_{(p,|\{1,0\}\rangle)}t}$.

The full theory is compared to the data in Fig. 5.2a (purple line). The data is consistent with the full theory, showing that we have a rough characterization of the system. We note that the most important inclusion is the spontaneous emission probability, as this is the reason for the observed QFI decaying as a function of time. To show that the numerics capture the observed dynamics, we also construct the \vec{f}_Q in Fig. 5.2b, where the data are the points and the theory the purple line. The data follows the arc of the theory very well in the vector space. We highlight the points in green which are consistent with 10-particle entanglement.

This analysis indicates that spontaneous emission is the primary cause of the deviation of our data from the predicted values. Since spontaneous emission independently effects all ions equally, the mixed state density matrix of our system ρ_{obs}

is a mixture of the coherent state density matrix ρ_{coh} and a purely diagonal matrix which is a mixture of all possible states ρ_{diag} :

$$\rho_{obs} = p\rho_{coh} + (1 - p)\rho_{diag} \quad (5.14)$$

where p is the probability of not having a spontaneous emission event at a given time. While the exact composition of ρ_{diag} would require reconstruction of the full density matrix, if we approximate it as a perfectly mixed state, then the QFI reduces to Eq. 5.11. If we compare the result to the full numerics described above or the data, the agreement is almost perfect, showing that this dissipation in our system is captured by the QFI. While such an argument is a weak demonstration of entanglement, it can still be used as a metric to determine the quantumness of the simulation.

5.2.4 Measured QFI for 24 spins

We emphasize this further by performing an identical experiment using 24 ions. This system size is right on the edge of what is possible to use exact diagonalization in order to classically simulate the system. In this case, we had our colleague Zhexuan Gong run the numerics on a supercomputer taking a total of 2 days. By adding only a couple more spins to the simulation, the problem becomes functionally impossible for exact diagonalization and requires approximation methods such as DMRG. By comparing our data to the numerics, we find that behavior is similar to that of the 10 ion data, agreeing very well at short times but diverging at later times (see Fig. 5.3). By applying the ideas above about the effect of spontaneous emission,

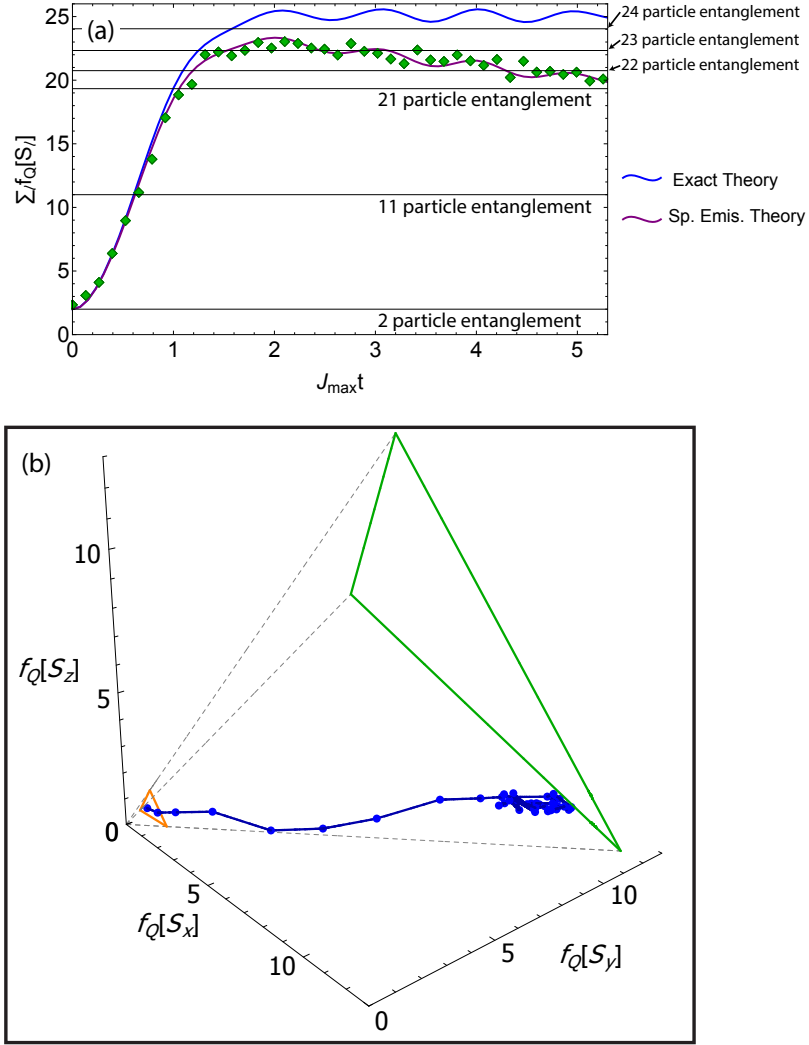


Figure 5.3: Measurement of QFI in 24 Spins. Plot of 24 ion \bar{f}_Q as a function of time with pure state assumption (a). Due to size of system, exact diagonalization is not possible on normal computer. Numerics were run on campus supercomputer, taking 2 days to complete. As few as only a couple additional spins would make such a calculation functionally impossible, requiring approximation techniques such as DMRG to make the problem tractable. We compare our data to the exact numerics (blue) and also to approximation of Eq. 5.11 from spontaneous emission (purple). We also show the 24 ion trajectory through the QFI vector space (b). While having much of the same character as the 10 ion case, we see that the spontaneous emission prevents the system from growing to 24-particle entanglement. Line is a guide for the eye.

we compare the data to a modified theory $\overline{f_{Q_{obs}}}$, where $\overline{f_{Q_{obs}}} = e^{-N\gamma_{(p,|\{1,0\})}t} \overline{f_{Q_{coh}}}$ and $\overline{f_{Q_{coh}}}$ is the QFI predicted by the numerics.

The agreement between the data and the modified theory shows that the dominant source of error in the simulation arises from spontaneous emission, which is enhanced as we increase the system size to larger numbers. This experiment also shows the usefulness of the QFI as a metric for how quantum a system is, despite the fact that we do not have demonstrable entanglement. As system sizes continue to grow, observables which are simple to measure and intimately tied to the coherence of a many-body system will become extremely important as a means to verifying that the system is in some sense still quantum even when classical numerics are no longer possible.

Chapter 6: Failures of Quantum Thermalization

Statistical mechanics can predict thermal equilibrium states for most classical systems, but for an isolated quantum system there is no general understanding on how equilibrium states dynamically emerge from the microscopic Hamiltonian [114–120]. Exceptions to quantum thermalization have been observed, but typically require inherent symmetries [116, 121] or noninteracting particles in the presence of static disorder [119, 122–124]. For this reason, the predictions of many-body localization (MBL), in which disordered quantum systems can fail to thermalize despite strong interactions and high excitation energy, were surprising and have attracted considerable theoretical attention [119, 120, 125–127]. This MBL phase is predicted to emerge for a broad set of interaction ranges and disorder strengths, though the precise phase diagram is not well known [128] since equilibrium statistical mechanics breaks down in the MBL phase and numerical simulations are limited to ~ 20 particles [125, 126]. While recent experiments searching for MBL have measured constrained mass transport and the breakdown of ergodicity in disordered atomic systems with interactions [37, 38], we have directly observed MBL in a long-range transverse field Ising model with programmable, random disorder in a system of ten spins [40].

Yet this failure of thermalization observed in MBL is only one way quantum thermalization diverges from the classical. Despite the fact that quantum dynamics are always unitary, we normally expect that measurements made within a subsystem trace over the rest of the system and appear thermal because the rest of the system acts as a thermal bath [95,129,130]. Yet, as mentioned above, there are cases where this is not true. For integrable models an extensive number of conserved quantities prevent the efficient exploration of phase space [116,117] and the system relaxes to a steady-state predicted by a generalized Gibbs ensemble (GGE) [131,132] specified by the initial values of the integrals of motion. For near-integrable systems, such as weakly interacting ultracold gases, thermalization can still occur, but only over extremely long time scales beyond current experimental reach [121,133]. However, it is possible to observe quasi-stationary states, often called prethermal, that emerge within an experimentally accessible time scale.

Previous observations of prethermal states have focused on those described by a GGE associated with the integrable part of the system [121,133]. Here, we observe a new form of prethermalization [134], where a system of interacting spins rapidly evolves to a quasi-stationary state that cannot be described by a GGE. This type of prethermal state arises when a system has long range interactions and open boundaries such that the translational invariance is broken, even in the thermodynamic limit. As a result, spin excitations feel an emergent double-well potential whose depth grows with interaction range (Fig.6.1). Memory of the initial state is preserved by this emergent potential, but is eventually lost due to weak tunneling between the two wells and the interactions between spin excitations.

6.1 Experimental Setup

To study prethermalization in our trapped ion quantum simulator, we apply a large transverse field Ising model Hamiltonian:

$$H = \sum_{i < j} J_{ij} \sigma_i^x \sigma_j^x + B \sum_i \sigma_i^z, \quad (6.1)$$

where B is a uniform effective transverse field (see section 2.3.2). We set the interaction $J_{ij} = \frac{J_{\max}}{|i-j|^\alpha}$ where $J_{\max}/(2\pi)$ is the maximum coupling strength which ranges from 0.45 – 0.98 kHz, and set the magnetic field $B/(2\pi) = 10$ kHz. We tune the power law exponent α between $\alpha = 0.55$ and 1.33 by changing the axial confinement of the ions. With long-range interactions, H is in general non-integrable, in contrast to the nearest-neighbor case where the 1D model is integrable [135] and thermalization is anticipated in the long time limit according to eigenstate thermalization hypothesis [136–138]. However, with a small number of spin excitations one can map Eq. 6.1 into bosons and approximate the Hamiltonian with an integrable term of free bosons and an integrability breaking perturbation of interacting bosons that eventually thermalizes the system at times longer than $\sim B^2/J^3$ (see section 6.3).

We initialize the chain of seven spins by optically pumping all spins to the $|\downarrow_z\rangle$ state, and then use a tightly focused individual-ion addressing laser to excite a single spin on one end of the chain to the $|\uparrow_z\rangle$ state as seen in Fig. 6.1a (see chapter 4). The spins then evolve under Eq. 6.1 and we measure the time evolution of the spin projection in the \hat{z} -basis. For the shortest range interactions we

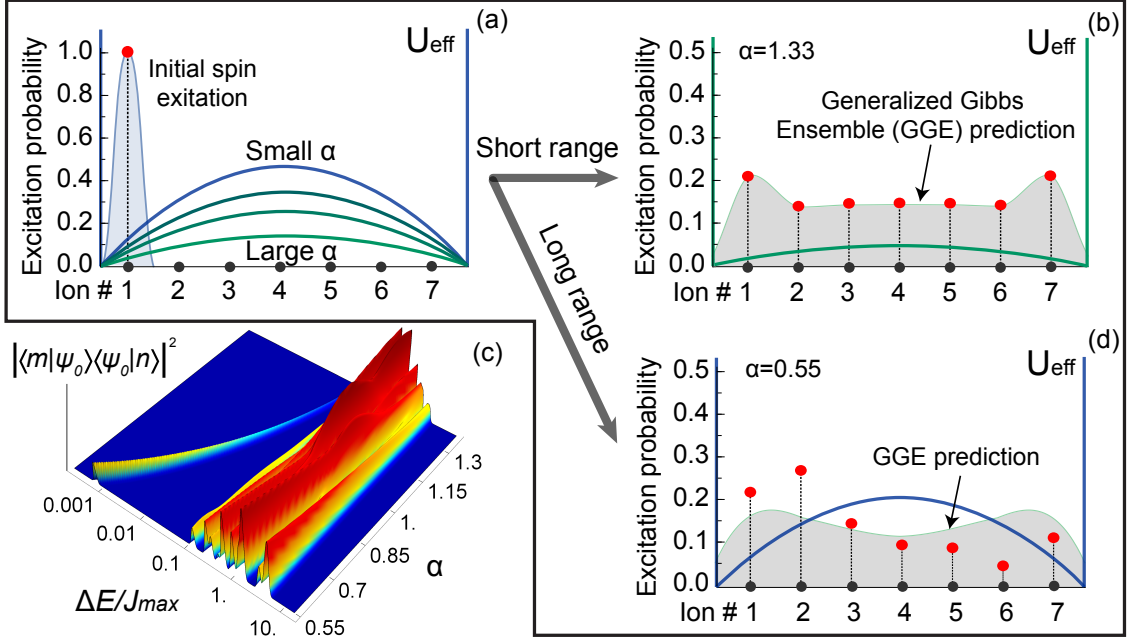


Figure 6.1: Emergent double well potential. (a) The spin chain starts with a single spin excitation on the left end. (b) For short range interactions ($\alpha = 1.33$), we map the system to a particle in a 1D square well where the excitation becomes symmetrically distributed across the chain as predicted by the GGE, $\langle \sigma_i^z \rangle_{\text{GGE}}$. (d) However, for long-range interactions ($\alpha = 0.55$) the Hamiltonian resembles a double-well potential which prevents the efficient transfer of the spin and the excitation location retains memory of the initial state and resides primarily on the left half, in contrast to $\langle \sigma_i^z \rangle_{\text{GGE}}$. (c) (Double well gives rise to) near-degenerate eigenstates which emerge as α is decreased as seen in the calculated energy difference between all pairs of eigenstates versus α with amplitude weighted by the product of the eigenstates overlap with the initial state . Because of this near degeneracy, the initial phase relationship between these two eigenstates remains frozen for the experimentally accessible timescales.

realize ($\alpha = 1.33$) the system rapidly evolves to a prethermal state predicted by the GGE associated with the integrals of motion corresponding to the momentum space occupation number of the non-interacting bosons (see section 6.3) (Fig. 6.1b).

However, in the long-range interacting case ($\alpha = 0.55$) we see the location of the spin excitation reaches an equilibrium value that retains a memory of the initial state (Fig. 6.1d) out to the longest experimentally achievable time of $25/J_{\max}$. This prethermal state is in obvious disagreement with both a thermal state and the GGE prediction, as both maintain the right-left symmetry of the system.

In the thermodynamic limit, the spin-wave boson model for short-range interactions are similar to those of a free-particle in a square-well. However, for long-range interactions, there is an emergent double-well potential and the spin-wave model has an extensive number of near-degenerate eigenstates. These eigenstates, which are superpositions of its symmetric and antisymmetric ground states, correspond to spin excitations in the left and right potential well. For seven spins, we calculate the energy difference between all pairs of eigenstates for seven spins and plot them with respect to α in Fig. 6.1c where the amplitudes, $|\langle m|\psi_0\rangle\langle\psi_0|n\rangle|^2$, are the product of each eigenstates', $|m\rangle, |n\rangle$, overlap with the initial state. With $\alpha = 0.55$ the two lowest energy states are almost degenerate, with an energy difference one-thousand times smaller than J_{\max} , due to the tunneling rate which is exponentially small in the height of the double well. As a result the spin excitation will remain in its initial well until it tunnels into the other well at a much longer time.

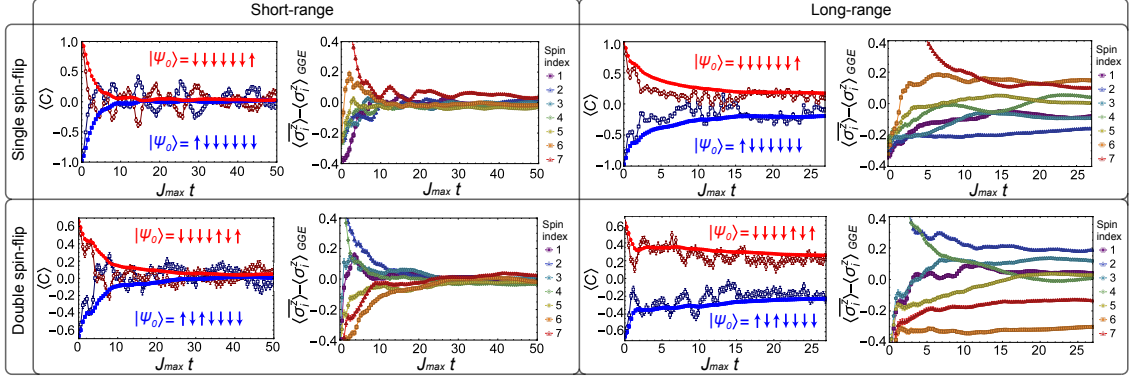


Figure 6.2: Measured location of spin excitation. The average position of the spin excitation, $\langle C \rangle$, is plotted for an initial excitation on the left (dark blue) and right (dark red) along with their cumulative time average (blue and red), for short-range ($\alpha = 1.33$) and long-range ($\alpha = 0.55$) interactions with initial states with one spin excitation (left panel) and two spin excitations (right panel). The cumulative time average of the deviation of the postselected individual spin projections from the generalized Gibbs ensemble, $\langle \sigma_i^z \rangle - \langle \sigma_i^z \rangle_{GGE}$, is also plotted. For short-range interactions the spins quickly thermalize to a value predicted by the GGE, but for the long-range interacting system a prethermal state emerges.

6.2 Observation of Prethermalization

To better characterize the “location” of the spin excitation we construct the observable

$$C = \sum_i \frac{2i - N - 1}{N - 1} \frac{\sigma_i^z + 1}{2}, \quad (6.2)$$

where N is the number of ions. The expectation value of C varies between -1 and 1 for a spin excitation on the left and right ends respectively. Due to the spatial inversion symmetry of the spin-wave boson model and Eq. 6.1, the GGE predicted and thermal values of $\langle C \rangle$ are zero. In Fig. 6.2, we plot $\langle C \rangle$ along with its cumulative time average $\langle \overline{C} \rangle$ for $\alpha = 1.33$ (short-range) and $\alpha = 0.55$ (long-range). To further emphasize the asymmetry of the prethermalization we prepare initial states with a

single-spin excitation on the left or right ends of the chain.

With short-range interactions the system quickly relaxes to the prethermal value predicted by the GGE where $\langle C \rangle$ is near zero irrespective of the initial state. $\langle \overline{C}_{t=50/J_{\max}} \rangle = -0.018(4)$ ($-0.032(4)$) for the initial spin excitation on the right (left). But with long-range interactions, the prethermal state that emerges retains a clear memory of the initial conditions as $\langle \overline{C}_{t=25/J_{\max}} \rangle = 0.205(4)$ ($-0.179(4)$) for the excitation starting on the right (left), showing a clear discrepancy with both the thermal and GGE predictions.

It is useful to talk about thermalization in terms of local quantities since subsystems must use the rest of the chain as a heat bath. In Fig. 6.2 we plot the cumulative time average of the deviation of the single spin magnetizations $\langle \sigma_i^z \rangle$ from the GGE. Here we postselect the data for the correct number of spin excitations to eliminate the effects of imperfect state preparation and small deviations from our model Hamiltonian due to unwanted excitations of the phonon modes. For the short-range interactions we see the cumulative time average quickly converge to the GGE predicted value. However, with the long-range interactions we see the individual spins reach a steady state that does not match the GGE as the pair of near degenerate eigenstates prevents the efficient transfer of the excitation across the chain.

We show the prethermal state's robustness to weak interactions, similar to MBL [119,120], by preparing initial states with two spin excitations. In this case, the multiple spin flips increase the size of the integrability breaking part of the Hamiltonian which represents weak interactions between the spin-wave bosons. How-

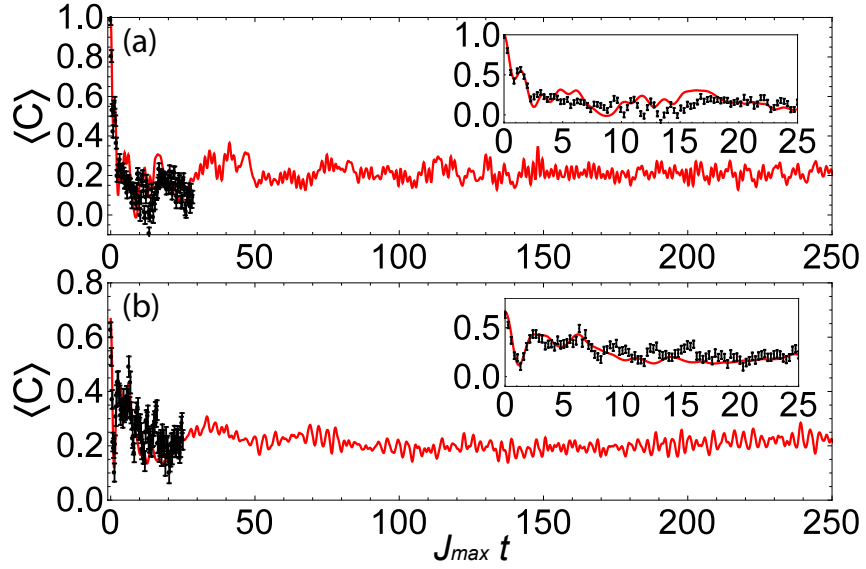


Figure 6.3: Comparison of prethermal data to exact numerics. Comparison between a numerical simulation of the transverse field Ising model and experimental data for a single spin excitation (top panel) and a double excitation (bottom panel). The inset shows excellent agreement between experiment and numerics accounting for experimental noise for $\langle C \rangle$. For both the single and double spin flip cases, the prethermal state persists for much longer than the experimental timescale and eventually relaxes to the thermal state.

ever, the prethermal state still persists. For better contrast between the prethermal and GGE predicted values of $\langle C \rangle$, we flip the second and fourth spin such that $|\psi_0\rangle = |\downarrow\uparrow\downarrow\uparrow\downarrow\downarrow\rangle$. We emphasize that the observed prethermalization and departure from the GGE prediction is not sensitive to the specific choice of initial state. But for a small sized system, these initial states offer us the maximum signal to noise ratio. As before, we also prepare the mirror image of the initial state by exciting the fourth and sixth ions ($|\psi_0\rangle = |\downarrow\downarrow\downarrow\uparrow\downarrow\uparrow\rangle$). We observe relaxation to the value predicted by the GGE for short-range interactions, but with long-range interactions we see a prethermal state that strongly deviates from the GGE (bottom panel of Fig. 6.2).

In Fig. 6.3 we plot the experimental evolution of the prethermal state for both the double and single spin flip initial states along with a long-time numerical simulation under Eq. 6.1 with an inset comparing the short-time dynamics to a model accounting for known experimental noise. There is excellent agreement between the two and confirmation that the prethermal states persist well beyond the current experimental time limit. Due to the interactions between the spin-wave bosons, the system will eventually relax to the thermal equilibrium in the thermodynamic limit, however relaxation to the GGE may or may not be seen depending on the range of interactions.

To demonstrate that the prethermal state we observe is not due to small system size, we repeat the experiment in a chain of 22 ions, the largest ion chain used for quantum simulation in the literature to date. The time evolution and cumulative time average of $\langle C \rangle$ are depicted in Fig. 6.4. Experimentally, as well as in the

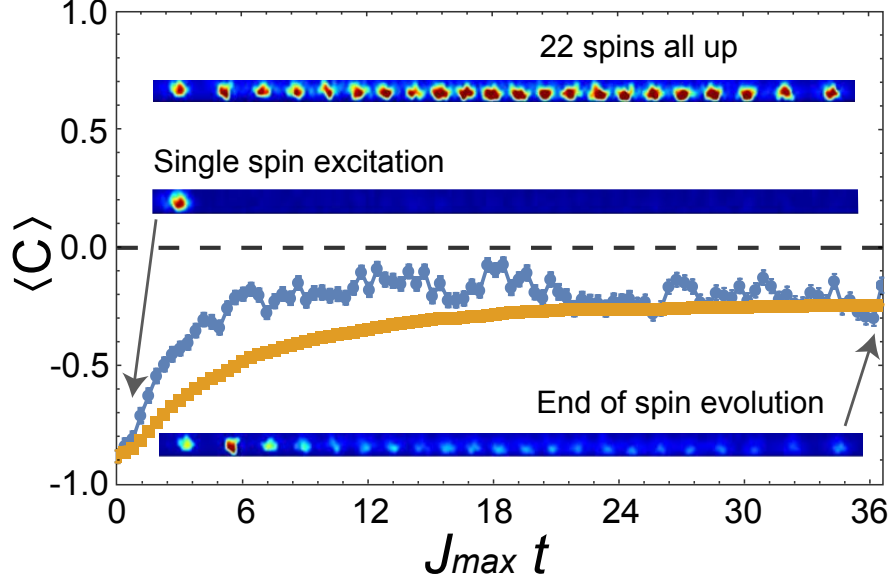


Figure 6.4: Scaling to large system size. Time evolution (light blue) and cumulative time average (orange) of $\langle C \rangle$ with false color pictures of the 22 ion chain, where the brightness of each ion is determined by the value of $\langle \sigma_i^z \rangle$. The ions fluoresce during detection when in the $|\uparrow\rangle$ state (top picture). We initialize the chain with a single spin excitation on the left end of the chain (middle picture). After evolving for 36 J_{\max} the spin excitation is delocalized, but its average position remains on the left half of the chain (bottom picture).

analytic result in the thermodynamic limit, we see the system relaxes to a similar quasi-equilibrium state as before that clearly has memory of the initial state.

We point out the observed prethermalization and deviation from the GGE should disappear if the system is subject to periodic boundary conditions, regardless of system size. Here we emphasize that the long-range interactions make the boundary conditions relevant for bulk properties and thus changing the boundary conditions can impact an extensive number of eigenstates. The effects of long-range interactions on many-body dynamics are, however, far richer than the effect discussed in the current experiment. For sufficiently long-range interactions, the notion of locality breaks down and quasi-particles in the system can travel at divergent

velocities for thermodynamic systems, potentially leading to dramatically different thermalization/prethermalization time scales in certain systems [34, 35, 139].

6.3 Spin-boson mapping and the GGE

To explain our observed prethermalization, it is convenient to map the spins into bosons by using the Holstein-Primakoff transformation: $\sigma_i^z = 2a_i^\dagger a_i - 1$, $\sigma_i^+ = a_i^\dagger \sqrt{1 - a_i^\dagger a_i}$. We will assume that the average spin excitation density $\bar{n} = \sum_i \langle a_i^\dagger a_i \rangle / N$ is much smaller than 1. This assumption is justified in our experiments because (1) our initial states have small spin excitation densities and (2) we set $\max(J_{ij}) \ll B$ so the amount of \bar{n} that will be dynamically created is small [$\sim (\max(J_{ij})/B)^2$]. Therefore to the lowest order we can approximate $\sigma_i^+ \approx a_i^\dagger$, and Eq. 6.1 reduces to an integrable Hamiltonian H_0 made of non-interacting bosons

$$H_0 = \sum_{i < j} J_{ij} (a_i^\dagger a_j + a_i^\dagger a_j^\dagger + h.c.) + 2B \sum_i a_i^\dagger a_i \quad (6.3)$$

$$H_1 = H - H_0.$$

Here H_1 contains interactions between the bosons which are parametrically small in \bar{n} , and, as a result, we can treat H_1 as a perturbation to H_0 . Thus, it is natural to expect the system (in the thermodynamic limit) to first relax to a prethermal state described by the GGE of H_0 , and to later relax to a thermal state described by the full H . Naively, we expect the thermalization to happen at a time scale much longer than the relaxation to GGE, based on the different energy scales of H_0 and H_1 . However, this is not always the case, as discussed below.

Integrable models have many conserved quantities that are not taken into account by traditional ensembles from statistical mechanics. Thus, the GGE was developed to make predictions about equilibrium values of observables in these systems by incorporating the additional integrals of motion [131, 132, 140–143]. The GGE predicted density matrix is given by:

$$\rho_{GGE} = \sum_k e^{-\lambda_k \hat{I}_k} / \text{tr}(e^{-\lambda_k \hat{I}_k}) \quad (6.4)$$

where λ_k is the overlap of the initial state with the integral of motion, \hat{I}_k . We observe relaxation to the GGE if for any local observable \hat{O} , $\langle O(t) \rangle \approx \text{tr}(O \rho_{GGE})$. The GGE is equivalent to the grand canonical ensemble for a general quantum system when the only conserved quantities are particle number and total energy [131].

To explicitly define the GGE of H_0 , we would need to first diagonalize H_0 and find the integrals of motion. Note that Eq. 6.1 only involves J_{ij} for $i < j$. For convenience, we will define a new matrix \mathcal{J} such that $\mathcal{J}_{ii} = 0$ and $\mathcal{J}_{ij} = \mathcal{J}_{ji} = J_{ij}$ for $i < j$. H_0 can be rewritten as

$$H_0 = \sum_{i,j} \mathcal{J}_{ij} \left[a_i^\dagger a_j + \frac{1}{2} (a_i^\dagger a_j^\dagger + a_i a_j) \right] + 2B \sum_i a_i^\dagger a_i. \quad (6.5)$$

An orthogonal matrix \mathcal{V} can be used to diagonalize the matrix \mathcal{J} as $\sum_{i,j} \mathcal{V}_{ik} \mathcal{J}_{ij} \mathcal{V}_{jk'} = \nu_k \delta_{kk'}$, where $\{\nu_k\}$ are the eigenvalues of matrix \mathcal{J} . Introducing $c_k = \sum_i \mathcal{V}_{ik} a_i$, we have

$$H_0 = \sum_k \left[(\nu_k + 2B) c_k^\dagger c_k + \frac{1}{2} \nu_k (c_k^\dagger c_k^\dagger + c_k c_k) \right]. \quad (6.6)$$

Next, we perform a Bogoliubov transformation $c_k = \cosh(\theta_k)d_k - \sinh(\theta_k)d_k^\dagger$ with $\theta_k = \frac{1}{2} \tanh^{-1}(\frac{\nu_k}{\nu_k + 2B})$ to fully diagonalize H_0 :

$$H_0 = \sum_k \epsilon_k d_k^\dagger d_k \quad \epsilon_k \equiv 2\sqrt{B(B + \nu_k)}, \quad (6.7)$$

The GGE for H_0 is defined as

$$\rho_{GGE} = \frac{e^{-\sum_k \lambda_k d_k^\dagger d_k}}{\text{Tr}(e^{-\sum_k \lambda_k d_k^\dagger d_k})}, \quad (6.8)$$

with λ_k determined by $\langle d_k^\dagger d_k \rangle_0 = \langle d_k^\dagger d_k \rangle_{GGE}$, where the notation $\langle \cdots \rangle_0$ denotes the expectation value in the initial state $|\psi_0\rangle$, and the notation $\langle \cdots \rangle_{GGE}$ denotes the expectation value in ρ_{GGE} . Using the fact that our initial state $|\psi_0\rangle$ is always a Fock state in the basis of $\{a_i^\dagger a_i\}$, the value of $\langle d_k^\dagger d_k \rangle_0$ can be calculated by the following formula

$$\langle d_k^\dagger d_k \rangle_0 = \cosh(2\theta_k) \sum_i \mathcal{V}_{ik}^2 \langle a_i^\dagger a_i \rangle_0 + \sinh^2(\theta_k). \quad (6.9)$$

To calculate the expectation values of $\sigma_i^z = 2a_i^\dagger a_i - 1$ in GGE, we use the following equations

$$\begin{aligned} \langle a_i^\dagger a_i \rangle_{GGE} &= \langle \sum_{k,k'} \mathcal{V}_{ik} \mathcal{V}_{ik'} c_k^\dagger c_{k'} \rangle_{GGE}, \\ &= \sum_k \mathcal{V}_{ik}^2 \langle \cosh(2\theta_k) d_k^\dagger d_k + \sinh^2(\theta_k) \rangle_{GGE}, \\ &= \sum_k \mathcal{V}_{ik}^2 [\cosh(2\theta_k) \langle d_k^\dagger d_k \rangle_0 + \sinh^2(\theta_k)], \end{aligned} \quad (6.10)$$

where we use the fact that ρ_{GGE} is diagonal in the Fock basis of $\{d_k^\dagger d_k\}$, so $\langle d_k^\dagger d_{k'} \rangle_{GGE} = \langle d_k^\dagger d_{k'}^\dagger \rangle_{GGE} = 0$ for $k \neq k'$.

6.4 Origin of the double well

The low-energy eigenstates of a massive particle in a double-well-shaped potential are localized orbitals inside either well (Fig. 6.1b). The tunneling rate (which is exponentially small in the height of the barrier) splits the degeneracy of the localized orbitals in each well and leads to pairs of symmetric and antisymmetric wavefunctions (upon the spatial inversion of the chain). This physical picture explains the observed prethermalization: Initial excitations placed in the left half of the chain will be localized for an extended period of time (inversely proportional to the tunneling rate) under the evolution of H_0 , until the tunneling between the two wells eventually delocalizes the excitations.

Interestingly, the double-well-shaped potential is emergent in our system, because the non-interacting Hamiltonian H_0 contains no inhomogeneous potential. This emergent inhomogeneity is somewhat a surprising effect because the motional Hamiltonian of the ions in the trap and the spin-motion couplings induced by the Raman lasers are all homogeneous. The key is that the long-range interactions make our spin Hamiltonian Eq. 6.1 no longer translationally invariant (even in the thermodynamic limit). This is in contrast to an open-boundary spin chain with only short-range interactions, where it is usually safe to assume translational invariance for sufficiently large system sizes.

The notion of boundary starts to break down for sufficiently long-ranged interactions, and therefore we cannot attribute the observed prethermalization to boundary effects. Usually, boundary effects only affect a finite number of eigenstates and do not affect local quenches in the bulk. However, here there is extensive number of eigenstates that are localized in the two wells described by the potential $U(z)$, and excitations placed with an extensive number of lattice sites away from the edges are still subject to qualitatively similar dynamics.

Finally, we point out that interactions in H_1 can also delocalize the initial spin excitations placed in one of the wells, and eventually thermalize the system. As a result, there is an interesting interplay between the timescale of the prethermalization to GGE and the timescale of thermalization. If the interactions in H_1 are sufficiently weaker than the kinetic tunneling rate in H_0 (which can be achieved by turning down the magnetic field strength B , or changing the range of interactions), then we expect the system to have two prethermal phases, with the observed prethermalization followed by prethermalization to the GGE of H_0 , and further followed by the thermalization process. On the contrary, if the tunneling rate is sufficiently smaller than the interaction strength of H_1 , then the prethermal states described by the GGE of H_0 may never appear during the time evolution, and we will find thermalization directly following the observed prethermalization. These interesting multi-stage relaxation processes will require future experimental investigations, where longer coherence time and larger number of the spins are technically achievable.

Bibliography

- [1] P. Shor, “Algorithms for quantum computation: Discrete logarithms and factoring,” *Proceedings of the Annual Symposium on Foundations of Computer Science*, pp. 124–134, 1994.
- [2] L. K. Grover, “Quantum mechanics helps in searching for a needle in a haystack,” *Phys. Rev. Lett.*, vol. 79, p. 325, 1997.
- [3] M. Mosca, *Quantum Algorithms*, pp. 7088–7118. New York, NY: Springer New York, 2009.
- [4] A. M. Childs and W. van Dam, “Quantum algorithms for algebraic problems,” *Rev. Mod. Phys.*, vol. 82, pp. 1–52, Jan 2010.
- [5] B. M. Terhal, “Quantum error correction for quantum memories,” *Rev. Mod. Phys.*, vol. 87, pp. 307–346, Apr 2015.
- [6] T. D. Ladd, F. Jelezko, R. Laflamme, Y. Nakamura, C. Monroe, and J. L. O’Brien, “Quantum computers,” *Nature*, vol. 464, p. 45, 2010.
- [7] I. Bloch, J. Dalibard, and W. Zwerger, “Many-body physics with ultracold gases,” *Rev. Mod. Phys.*, vol. 80, p. 885, 2008.
- [8] F. A. Zwanenburg, A. S. Dzurak, A. Morello, M. Y. Simmons, L. C. L. Hollenberg, G. Klimeck, S. Rogge, S. N. Coppersmith, and M. A. Eriksson, “Silicon quantum electronics,” *Rev. Mod. Phys.*, vol. 85, pp. 961–1019, Jul 2013.
- [9] J. Clarke and F. K. Wilhelm, “Superconducting quantum bits,” *Nature*, vol. 453, pp. 1031–1042, June 2008.
- [10] R. Blatt and D. Wineland, “Entangled states of trapped atomic ions,” *Nature*, vol. 453, p. 1008, 2008.
- [11] C. J. Ballance, T. P. Harty, N. M. Linke, M. A. Sepiol, and D. M. Lucas, “Laser-driven quantum logic gates with precision beyond the fault-tolerant threshold.” arXiv:1512.04600, 2015.

- [12] J. P. Gaebler, T. R. Tan, Y. W. Y. Lin, R. Bowler, A. C. Keith, S. Glancy, K. Coakley, E. Knill, D. Leibfried, and D. J. Wineland, “High-fidelity universal gate set for ${}^9\text{Be}^+$ ion qubits.” arXiv:1604.00032, 2016.
- [13] Z. Chen, J. Kelly, C. Quintana, R. Barends, B. Campbell, Y. Chen, B. Chiaro, A. Dunsworth, A. G. Fowler, E. Lucero, E. Jeffrey, A. Megrant, J. Mutus, M. Neeley, C. Neill, P. J. J. O’Malley, P. Roushan, D. Sank, A. Vainsencher, J. Wenner, T. C. White, A. N. Korotkov, and J. M. Martinis, “Measuring and suppressing quantum state leakage in a superconducting qubit,” *Phys. Rev. Lett.*, vol. 116, p. 020501, Jan 2016.
- [14] R. Barends, J. Kelly, A. Megrant, A. Veitia, D. Sank, E. Jeffrey, T. C. White, J. Mutus, A. G. Fowler, B. Campbell, Y. Chen, Z. Chen, B. Chiaro, A. Dunsworth, C. Neill, P. O’Malley, P. Roushan, A. Vainsencher, J. Wenner, A. N. Korotkov, A. N. Cleland, and J. M. Martinis, “Superconducting quantum circuits at the surface code threshold for fault tolerance,” *Nature*, vol. 508, pp. 500–503, Apr. 2014.
- [15] T. Monz, D. Nigg, E. A. Martinez, M. F. Brandl, P. Schindler, R. Rines, S. X. Wang, I. L. Chuang, and R. Blatt, “Realization of a scalable shor algorithm,” *Science*, vol. 351, no. 6277, pp. 1068–1070, 2016.
- [16] S. Debnath, N. M. Linke, C. Figgatt, K. A. Landsman, K. Wright, and C. Monroe, “Demonstration of a programmable quantum computer module.” arXiv:1603.04512, March 2016.
- [17] S. Lloyd, “Universal quantum simulators,” *Science*, vol. 273, p. 1073, 1996.
- [18] R. Feynman, “Simulating physics with computers,” *International Journal of Theoretical Physics*, vol. 21, p. 467, 1982.
- [19] I. M. Georgescu, S. Ashhab, and F. Nori, “Quantum simulation,” *Rev. Mod. Phys.*, vol. 86, pp. 153–185, Mar 2014.
- [20] I. Bloch, J. Dalibard, and S. Nascimbene, “Quantum simulations with ultracold gases,” *Nature Physics*, vol. 8, p. 267, 2012.
- [21] R. Blatt and C. F. Roos, “Quantum simulations with trapped ions,” *Nature Physics*, vol. 8, p. 277, 2012.
- [22] A. Aspuru-Guzik and P. Walther, “Photonic quantum simulators,” *Nature Physics*, vol. 8, p. 285, 2012.
- [23] A. A. Houck, H. E. Tureci, and J. Koch, “On-chip quantum simulation with superconducting circuits,” *Nat Phys*, vol. 8, pp. 292–299, Apr. 2012.
- [24] E. Farhi, J. Goldstone, S. Gutmann, J. Lapan, A. Lundgren, and D. Preda, “A quantum adiabatic evolution algorithm applied to random instances of an np-complete problem,” *Science*, vol. 292, p. 472, 2001.

- [25] M. W. Johnson, M. H. S. Amin, S. Gildert, T. Lanting, F. Hamze, N. Dickson, R. Harris, A. J. Berkley, J. Johansson, P. Bunyk, E. M. Chapple, C. Enderud, J. P. Hilton, K. Karimi, E. Ladizinsky, N. Ladizinsky, T. Oh, I. Perminov, C. Rich, M. C. Thom, E. Tolkacheva, C. J. S. Truncik, S. Uchaikin, J. Wang, B. Wilson, and G. Rose, “Quantum annealing with manufactured spins,” *Nature*, vol. 473, pp. 194–198, May 2011.
- [26] S. Boixo, T. F. Ronnow, S. V. Isakov, Z. Wang, D. Wecker, D. A. Lidar, J. M. Martinis, and M. Troyer, “Evidence for quantum annealing with more than one hundred qubits,” *Nat Phys*, vol. 10, pp. 218–224, Mar. 2014.
- [27] J. Simon, W. S. Bakr, R. Ma, M. E. Tai, P. M. Preiss, and M. Greiner, “Quantum simulation of antiferromagnetic spin chains in an optical lattice,” *Nature*, vol. 472, p. 307, 2011.
- [28] R. Islam, C. Senko, W. C. Campbell, S. Korenblit, J. Smith, A. Lee, E. E. Edwards, C.-C. J. Wang, J. K. Freericks, and C. Monroe, “Emergence and frustration of magnetic order with variable-range interactions in a trapped ion quantum simulator,” *Science*, vol. 340, p. 583, 2013.
- [29] P. Richerme, C. Senko, J. Smith, A. Lee, S. Korenblit, and C. Monroe, “Experimental performance of a quantum simulator: Optimizing adiabatic evolution and identifying many-body ground states,” *Phys. Rev. A*, vol. 88, p. 012334, 2013.
- [30] R. Barends, A. Shabani, L. Lamata, J. Kelly, A. Mezzacapo, U. L. Heras, R. Babbush, A. G. Fowler, B. Campbell, Y. Chen, Z. Chen, B. Chiaro, A. Dunsworth, E. Jeffrey, E. Lucero, A. Megrant, J. Y. Mutus, M. Neeley, C. Neill, P. J. J. OMalley, C. Quintana, P. Roushan, D. Sank, A. Vainsencher, J. Wenner, T. C. White, E. Solano, H. Neven, and J. M. Martinis, “Digitized adiabatic quantum computing with a superconducting circuit,” *Nature*, vol. 534, pp. 222–226, June 2016.
- [31] T. Uehlinger, G. Jotzu, M. Messer, D. Greif, W. Hofstetter, U. Bissbort, and T. Esslinger, “Artificial graphene with tunable interactions,” *Phys. Rev. Lett.*, vol. 111, p. 185307, Oct 2013.
- [32] N. Goldman, G. Juzelinas, P. hberg, and I. B. Spielman, “Light-induced gauge fields for ultracold atoms,” *Reports on Progress in Physics*, vol. 77, no. 12, p. 126401, 2014.
- [33] M. Cheneau, P. Barmettler, D. Poletti, M. Endres, P. Schauss, T. Fukuhara, C. Gross, I. Bloch, C. Kollath, and S. Kuhr, “Light-cone-like spreading of correlations in a quantum many-body system,” *Nature*, vol. 481, p. 484, 2012.
- [34] P. Richerme, Z.-X. Gong, A. Lee, C. Senko, J. Smith, M. Foss-Feig, S. Michalakakis, A. V. Gorshkov, and C. Monroe, “Non-local propagation of correlations

- in quantum systems with long-range interactions,” *Nature*, vol. 511, p. 198, 2014.
- [35] P. Jurcevic, B. P. Lanyon, P. Hauke, C. Hempel, P. Zoller, R. Blatt, and C. F. Roos, “Quasiparticle engineering and entanglement propagation in a quantum many-body system,” *Nature*, vol. 511, p. 202, 2014.
 - [36] R. Islam, R. Ma, P. M. Preiss, M. Eric Tai, A. Lukin, M. Rispoli, and M. Greiner, “Measuring entanglement entropy in a quantum many-body system,” *Nature*, vol. 528, pp. 77–83, Dec. 2015.
 - [37] M. Schreiber, S. S. Hodgman, P. Bordia, H. P. Lschen, M. H. Fischer, R. Vosk, E. Altman, U. Schneider, and I. Bloch, “Observation of many-body localization of interacting fermions in a quasi-random optical lattice,” *Science*, vol. 349, p. 842, 2015.
 - [38] S. S. Kondov, W. R. McGehee, W. Xu, and B. DeMarco, “Disorder-induced localization in a strongly correlated atomic hubbard gas,” *Phys. Rev. Lett.*, vol. 114, p. 083002, Feb 2015.
 - [39] J.-y. Choi, S. Hild, J. Zeiher, P. Schauß, A. Rubio-Abadal, T. Yefsah, V. Khemani, D. A. Huse, I. Bloch, and C. Gross, “Exploring the many-body localization transition in two dimensions,” *Science*, vol. 352, no. 6293, pp. 1547–1552, 2016.
 - [40] J. Smith, A. Lee, P. Richerme, B. Neyenhuis, P. W. Hess, P. Hauke, M. Heyl, D. A. Huse, and C. Monroe, “Many-body localization in a quantum simulator with programmable random disorder,” *Nat Phys*, vol. advance online publication, pp. –, June 2016.
 - [41] J. P. Covey, S. A. Moses, M. Garttner, A. Safavi-Naini, M. T. Miecnikowski, Z. Fu, J. Schachenmayer, P. S. Julienne, A. M. Rey, D. S. Jin, and J. Ye, “Doublon dynamics and polar molecule production in an optical lattice,” *Nat Commun*, vol. 7, pp. –, Apr. 2016.
 - [42] M. Saffman, T. G. Walker, and K. Mølmer, “Quantum information with rydberg atoms,” *Rev. Mod. Phys.*, vol. 82, pp. 2313–2363, Aug 2010.
 - [43] R. Loew, H. Weimer, J. Nipper, J. B. Balewski, B. Butscher, H. P. Buechler, and T. Pfau, “An experimental and theoretical guide to strongly interacting rydberg gases,” *Journal of Physics B: Atomic, Molecular and Optical Physics*, vol. 45, no. 11, p. 113001, 2012.
 - [44] O. Firstenberg, T. Peyronel, Q.-Y. Liang, A. V. Gorshkov, M. D. Lukin, and V. Vuletic, “Attractive photons in a quantum nonlinear medium,” *Nature*, vol. 502, p. 71, 2013.

- [45] K. Kim, S. Korenblit, R. Islam, E. E. Edwards, M.-S. Chang, C. Noh, H. Carmichael, G.-D. Lin, L.-M. Duan, C.-C. J. Wang, J. K. Freericks, and C. Monroe, “Quantum simulation of the transverse field ising model with trapped ions,” *New J. Physics*, vol. 13, p. 105003, 2011.
- [46] C. Senko, J. Smith, P. Richerme, A. Lee, W. C. Campbell, and C. Monroe, “Coherent imaging spectroscopy of a quantum many-body spin system,” *Science*, vol. 345, p. 430, 2014.
- [47] B. Neyenhuis, J. Smith, A. C. Lee, J. Zhang, P. Richerme, P. W. Hess, Z.-X. Gong, A. V. Gorshkov, and C. Monroe, “Observation of prethermalization in long-range interacting spin chains.” In preparation.
- [48] K. R. Islam, *Quantum Simulation of Interacting Spin Models with Trapped Ions*. PhD thesis, University of Maryland, College Park, 2012.
- [49] S. Korenblit, *Quantum Simulations of the Ising Model: Devil’s Staircase and Arbitrary Lattice Proposal*. PhD thesis, University of Maryland, College Park, 2013.
- [50] C. Senko, *Dynamics and excited states of quantum many-body spin chains with trapped ions*. PhD thesis, University of Maryland, 2014.
- [51] D. Hayes, D. N. Matsukevich, P. Maunz, D. Hucul, Q. Quraishi, S. Olmschenk, W. Campbell, J. Mizrahi, C. Senko, and C. Monroe, “Entanglement of atomic qubits using an optical frequency comb,” *Phys. Rev. Lett.*, vol. 104, p. 140501, 2010.
- [52] D. J. Wineland, C. Monroe, W. M. Itano, D. Leibfried, B. E. King, and D. M. Meekhof, “Experimental issues in coherent quantum-state manipulation of trapped atomic ions,” *Journal of Research of the National Institute of Standards and Technology*, vol. 103, p. 259, 1998.
- [53] E. T. Jaynes and F. W. Cummings, “Comparison of quantum and semiclassical radiation theories with application to the beam maser,” *Proc. IEEE*, vol. 51, p. 89, 1963.
- [54] K. Molmer and A. Sorensen, “Multiparticle entanglement of hot trapped ions,” *Phys. Rev. Lett.*, vol. 82, p. 1835, 1999.
- [55] E. Solano, R. L. de Matos Filho, and N. Zagury, “Deterministic bell states and measurement of the motional state of two trapped ions,” *Phys. Rev. A*, vol. 59, p. R2539, 1999.
- [56] S.-L. Zhu, C. Monroe, and L.-M. Duan, “Trapped ion quantum computation with transverse phonon modes,” *Phys. Rev. Lett.*, vol. 97, p. 050505, 2006.

- [57] T. Choi, S. Debnath, T. A. Manning, C. Figgatt, Z.-X. Gong, L.-M. Duan, and C. Monroe, “Optimal quantum control of multimode couplings between trapped ion qubits for scalable entanglement,” *Phys. Rev. Lett.*, vol. 112, p. 190502, May 2014.
- [58] P. J. Lee, K.-A. Brickman, L. Deslauriers, P. C. Haljan, L.-M. Duan, and C. Monroe, “Phase control of trapped ion quantum gates,” *Journal of Optics B*, vol. 7, p. S371, 2005.
- [59] H. F. Trotter, “On the product of semi-groups of operators,” *Proceedings of the American Mathematical Society*, vol. 10, p. 545, 1959.
- [60] B. P. Lanyon, C. Hempel, D. Nigg, M. Müller, R. Gerritsma, F. Zähringer, P. Schindler, J. T. Barreiro, M. Rambach, G. Kirchmair, M. Hennrich, P. Zoller, R. Blatt, and C. F. Roos, “Universal digital quantum simulation with trapped ions,” *Science*, vol. 334, no. 6052, pp. 57–61, 2011.
- [61] C. Balzer, A. Braun, T. Hannemann, C. Paape, M. Ettler, W. Neuhauser, and C. Wunderlich, “Electrodynamically trapped yb^+ ions for quantum information processing,” *Phys. Rev. A*, vol. 73, p. 041407, Apr 2006.
- [62] S. Olmschenk, K. C. Younge, D. L. Moehring, D. N. Matsukevich, P. Maunz, and C. Monroe, “Manipulation and detection of a trapped yb^+ hyperfine qubit,” *Phys. Rev. A*, vol. 76, p. 052314, 2007.
- [63] R. Islam, W. C. Campbell, T. Choi, S. M. Clark, S. Debnath, E. E. Edwards, B. Fields, D. Hayes, D. Hucul, I. V. Inlek, K. G. Johnson, S. Korenblit, A. Lee, K. W. Lee, T. A. Manning, D. N. Matsukevich, J. Mizrahi, Q. Quraishi, C. Senko, J. Smith, and C. Monroe, “Beat note stabilization of mode-locked lasers for quantum information processing,” *Optics Letters*, vol. 39, p. 3238, 2014.
- [64] W. C. Campbell, J. Mizrahi, Q. Quraishi, C. Senko, D. Hayes, D. Hucul, D. N. Matsukevich, P. Maunz, and C. Monroe, “Ultrafast gates for single atomic qubits,” *Phys. Rev. Lett.*, vol. 105, p. 090502, 2010.
- [65] J. Mizrahi, *Ultrafast control of spin and motion in trapped Ions*. PhD thesis, University of Maryland, 2013.
- [66] D. J. Wineland, M. Barrett, J. Britton, J. Chiaverini, B. DeMarco, W. M. Itano, B. Jelenkovic, C. Langer, D. Leibfried, V. Meyer, T. Rosenband, and T. Schaetz, “Quantum information processing with trapped ions,” *Philosophical Transactions of the Royal Society A*, vol. 361, pp. 1349–1361, 2003.
- [67] R. Ozeri, W. M. Itano, R. B. Blakestad, J. Britton, J. Chiaverini, J. D. Jost, C. Langer, D. Leibfried, R. Reichle, S. Seidelin, J. H. Wesenberg, and D. J. Wineland, “Errors in trapped-ion quantum gates due to spontaneous photon scattering,” *Phys. Rev. A*, vol. 75, p. 042329, 2007.

- [68] H. J. Metcalf and P. van der Straten, *Laser Cooling and Trapping*. Springer-Verlag, 1999.
- [69] A. Kramida, Yu. Ralchenko, J. Reader, and NIST ASD Team. NIST Atomic Spectra Database (ver. 5.3), [Online]. Available: <http://physics.nist.gov/asd> [2016, March 31]. National Institute of Standards and Technology, Gaithersburg, MD., 2015.
- [70] B. C. Fawcett and M. Wilson, “Computed oscillator strengths, Landé g values, and lifetimes in Yb II,” *Atomic Data and Nuclear Data Tables*, vol. 47, pp. 241–317, 1991.
- [71] E. Biémont, J.-F. Dutrieux, I. Martin, and P. Quinet, “Lifetime calculations in Yb II,” *J. Phys. B: At. Mol. Opt. Phys.*, vol. 31, pp. 3321–3333, 1998.
- [72] J. Hynecek and T. Nishiwaki, “Excess noise and other important characteristics of low light level imaging using charge multiplying ccds,” *IEEE Transactions on Electron Devices*, vol. 50, pp. 239–245, Jan 2003.
- [73] A. C. Lee, “Ytterbium ion qubit state detection on an iccd camera,” b.sc. thesis, University of Maryland, College Park, 2012.
- [74] C. Shen and L.-M. Duan, “Correcting detection errors in quantum state engineering through data processing,” *New Journal of Physics*, vol. 14, p. 053053, 2012.
- [75] d. Lichtman, Martin Tom, *Coherent operations, entanglement, and progress toward quantum search in a large 2D array of neutral atom qubits*. [Madison, Wis.] : [University of Wisconsin–Madison], 2015., 2015.
- [76] J. J. Bollinger, D. J. Heinzen, W. M. Itano, S. . L. Gilbert, and D. J. Wineland, “A 303-mhz frequency standard based on trapped be ions,” *IEEE Transactions on Instrumentation and Measurement*, vol. 40, no. 2, pp. 126–128, 1991.
- [77] P. Fisk, M. Sellars, M. Lawn, and C. Coles, “Accurate measurement of the 12.6 ghz ”clock” transition in trapped $^{171}\text{Yb}^{+}$ ions,” *Ultrasonics, Ferroelectrics, and Frequency Control, IEEE Transactions on*, vol. 44, pp. 344–354, March 1997.
- [78] M. A. Nielsen and I. L. Chuang, *Quantum Computation and Quantum Information: 10th Anniversary Edition*. New York, NY, USA: Cambridge University Press, 10th ed., 2011.
- [79] J. Mizrahi, B. Neyenhuis, K. G. Johnson, W. C. Campbell, C. Senko, D. Hayes, and C. Monroe, “Quantum control of qubits and atomic motion using ultrafast laser pulses,” *Applied Physics B*, vol. 114, no. 1, pp. 45–61, 2013.
- [80] Zemax LLC, “Zemax (version 13.2),” 2013.

- [81] N. F. Ramsey, “Experiments with separated oscillatory fields and hydrogen masers,” *Rev. Mod. Phys.*, vol. 62, pp. 541–552, Jul 1990.
- [82] T. Graß, C. Muschik, A. Celi, R. W. Chhajlany, and M. Lewenstein, “Synthetic magnetic fluxes and topological order in one-dimensional spin systems,” *Phys. Rev. A*, vol. 91, p. 063612, Jun 2015.
- [83] E. A. Martinez, C. A. Muschik, P. Schindler, D. Nigg, A. Erhard, M. Heyl, P. Hauke, M. Dalmonte, T. Monz, P. Zoller, and R. Blatt, “Real-time dynamics of lattice gauge theories with a few-qubit quantum computer,” *Nature*, vol. 534, pp. 516–519, June 2016.
- [84] D. V. Else, B. Bauer, and C. Nayak, “Floquet time crystals.” arXiv:1603.08001 [cond-mat.dis-nn], 2016.
- [85] T. Lanting, A. J. Przybysz, A. Y. Smirnov, F. M. Spedalieri, M. H. Amin, A. J. Berkley, R. Harris, F. Altomare, S. Boixo, P. Bunyk, N. Dickson, C. Enderud, J. P. Hilton, E. Hoskinson, M. W. Johnson, E. Ladizinsky, N. Ladizinsky, R. Neufeld, T. Oh, I. Perminov, C. Rich, M. C. Thom, E. Tolkacheva, S. Uchaikin, A. B. Wilson, and G. Rose, “Entanglement in a quantum annealing processor,” *Phys. Rev. X*, vol. 4, p. 021041, May 2014.
- [86] T. Albash, W. Vinci, A. Mishra, P. A. Warburton, and D. A. Lidar, “Consistency tests of classical and quantum models for a quantum annealer,” *Phys. Rev. A*, vol. 91, p. 042314, Apr 2015.
- [87] T. Albash, I. Hen, F. M. Spedalieri, and D. A. Lidar, “Reexamination of the evidence for entanglement in a quantum annealer,” *Phys. Rev. A*, vol. 92, p. 062328, Dec 2015.
- [88] T. F. Rønnow, Z. Wang, J. Job, S. Boixo, S. V. Isakov, D. Wecker, J. M. Martinis, D. A. Lidar, and M. Troyer, “Defining and detecting quantum speedup,” *Science*, 2014.
- [89] V. S. Denchev, S. Boixo, S. V. Isakov, N. Ding, R. Babbush, V. Smelyanskiy, J. Martinis, and H. Neven, “What is the computational value of finite range tunneling?,” arXiv:1512.02206, 2015.
- [90] R. Islam, E. E. Edwards, K. Kim, S. Korenblit, C. Noh, H. Carmichael, G.-D. Lin, L.-M. Duan, C.-C. J. Wang, J. K. Freericks, and C. Monroe, “Onset of a quantum phase transition with a trapped ion quantum simulator,” *Nature Communications*, vol. 2, p. 377, 2011.
- [91] P. Jurcevic, P. Hauke, C. Maier, C. Hempel, B. P. Lanyon, R. Blatt, and C. F. Roos, “Spectroscopy of interacting quasiparticles in trapped ions,” *Phys. Rev. Lett.*, vol. 115, p. 100501, Sep 2015.

- [92] H. Häffner, W. Hänsel, C. F. Roos, J. Benhelm, D. C. al kar, M. Chwalla, T. Koerber, U. D. Rapol, M. Riebe, P. O. Schmidt, C. Becher, O. Guehne, W. Duer, and R. Blatt, “Scalable multiparticle entanglement of trapped ions,” *Nature*, vol. 438, p. 643, 2005.
- [93] J.-W. Pan, Z.-B. Chen, C.-Y. Lu, H. Weinfurter, A. Zeilinger, and M. Żukowski, “Multiphoton entanglement and interferometry,” *Rev. Mod. Phys.*, vol. 84, pp. 777–838, May 2012.
- [94] O. Gühne and G. Tóth, “Entanglement detection,” *Physics Reports*, vol. 474, no. 1-6, pp. 1 – 75, 2009.
- [95] A. M. Kaufman, M. E. Tai., A. Lukin, M. Rispoli, R. Schittko, P. M. Preiss., and M. Greiner, “Quantum thermalization through entanglement in an isolated many-body system.” arXiv:1603.04409.
- [96] C. Schwemmer, G. Tóth, A. Niggebaum, T. Moroder, D. Gross, O. Gühne, and H. Weinfurter, “Experimental comparison of efficient tomography schemes for a six-qubit state,” *Phys. Rev. Lett.*, vol. 113, p. 040503, Jul 2014.
- [97] C. A. Riofrio, D. Gross, S. T. Flammia, T. M. D. Nigg, R. Blatt, and J. Eisert, “Experimental quantum compressed sensing for a seven-qubit system.” Preprint.
- [98] O. Marty, M. Cramer, and M. B. Plenio, “Practical entanglement estimation for spin-system quantum simulators,” *Phys. Rev. Lett.*, vol. 116, p. 105301, Mar 2016.
- [99] W.-B. Gao, C.-Y. Lu, X.-C. Yao, P. Xu, O. Gühne, A. Goebel, Y.-A. Chen, C.-Z. Peng, Z.-B. Chen, and J.-W. Pan, “Experimental demonstration of a hyper-entangled ten-qubit schrodinger cat state,” *Nat Phys*, vol. 6, pp. 331–335, May 2010.
- [100] T. Monz, P. Schindler, J. T. Barreiro, M. Chwalla, D. Nigg, W. A. Coish, M. Harlander, W. Hänsel, M. Hennrich, and R. Blatt, “14-qubit entanglement: generation and coherence,” *Phys. Rev. Lett.*, vol. 106, p. 1304, 2011.
- [101] D. J. Wineland, J. J. Bollinger, W. M. Itano, and F. L. Moore, “Spin squeezing and reduced quantum noise in spectroscopy,” *Phys. Rev. A*, vol. 46, p. R6797, 1992.
- [102] M. Kitagawa and M. Ueda, “Squeezed spin states,” *Phys. Rev. A*, vol. 47, pp. 5138–5143, Jun 1993.
- [103] K. C. Cox, G. P. Greve, J. M. Weiner, and J. K. Thompson, “Deterministic squeezed states with collective measurements and feedback,” *Phys. Rev. Lett.*, vol. 116, p. 093602, Mar 2016.

- [104] O. Hosten, N. J. Engelsen, R. Krishnakumar, and M. A. Kasevich, “Measurement noise 100 times lower than the quantum-projection limit using entangled atoms,” *Nature*, vol. 529, pp. 505–508, Jan. 2016.
- [105] A. S. Sørensen and K. Mølmer, “Entanglement and extreme spin squeezing,” *Phys. Rev. Lett.*, vol. 86, pp. 4431–4434, May 2001.
- [106] J. G. Bohnet, B. C. Sawyer, J. W. Britton, M. L. Wall, A. M. Rey, M. Foss-Feig, and J. J. Bollinger, “Quantum spin dynamics and entanglement generation with hundreds of trapped ions,” *Science*, vol. 352, no. 6291, pp. 1297–1301, 2016.
- [107] O. Marty and M. Plenio, “Measuring entanglement in the long-range ising model.” Private communication, November 2015.
- [108] P. Hyllus, W. Laskowski, R. Krischek, C. Schwemmer, W. Wieczorek, H. Weinfurter, L. Pezzé, and A. Smerzi, “Fisher information and multiparticle entanglement,” *Phys. Rev. A*, vol. 85, p. 022321, Feb 2012.
- [109] G. Tóth, “Multipartite entanglement and high precision metrology,” *Phys. Rev. A*, vol. 85, p. 022322, 2012.
- [110] L. Pezzé and A. Smerzi, “Entanglement, nonlinear dynamics, and the heisenberg limit,” *Phys. Rev. Lett.*, vol. 102, p. 100401, Mar 2009.
- [111] P. Hyllus, O. Gühne, and A. Smerzi, “Not all pure entangled states are useful for sub-shot-noise interferometry,” *Phys. Rev. A*, vol. 82, p. 012337, Jul 2010.
- [112] H. Strobel, W. Muessel, D. Linnemann, T. Zibold, D. B. Hume, L. Pezzè, A. Smerzi, and M. K. Oberthaler, “Fisher information and entanglement of non-gaussian spin states,” *Science*, vol. 345, no. 6195, pp. 424–427, 2014.
- [113] E. Lieb and D. Robinson, “The finite group velocity of quantum spin systems,” *Commun. Math. Phys.*, vol. 28, p. 251, 1972.
- [114] A. Polkovnikov, K. Sengupta, A. Silva, and M. Vengalatorre, “Colloquium: Nonequilibrium dynamics of closed interacting quantum systems,” *Rev. Mod. Phys.*, vol. 83, p. 863, 2011.
- [115] M. A. Cazalilla and M. Rigol, “Focus on dynamics and thermalization in isolated quantum many-body systems,” *New Journal of Physics*, vol. 12, no. 5, p. 055006, 2010.
- [116] T. Kinoshita, T. Wenger, and D. S. Weiss, “A quantum newton’s cradle,” *Nature*, vol. 440, p. 900, 2006.
- [117] S. R. Manmana, S. Wessel, R. M. Noack, and A. Muramatsu, “Strongly correlated fermions after a quantum quench,” *Phys. Rev. Lett.*, vol. 98, p. 210405, May 2007.

- [118] M. Babadi, E. Demler, and M. Knap, “Far-from-equilibrium field theory of many-body quantum spin systems: Prethermalization and relaxation of spin spiral states in three dimensions,” *Phys. Rev. X*, vol. 5, p. 041005, Oct 2015.
- [119] P. W. Anderson, “Absence of diffusion in certain random lattices,” *Phys. Rev.*, vol. 109, p. 1492, 1958.
- [120] D. M. Basko, I. L. Aleiner, and B. L. Altshuler, “Possible experimental manifestations of the many-body localization,” *Phys. Rev. B*, vol. 76, p. 052203, 2007.
- [121] M. Gring, M. Kuhnert, T. Langen, T. Kitagawa, B. Rauer, M. Schreitl, I. Mazets, D. A. Smith, E. Demler, and J. Schmiedmayer, “Relaxation and prethermalization in an isolated quantum system,” *Science*, vol. 337, p. 1318, 2012.
- [122] D. S. Wiersma, P. Bartolini, A. Lagendijk, and R. Righini, “Localization of light in a disordered medium,” *Nature*, vol. 390, p. 671, 1997.
- [123] J. Billy, V. Josse, Z. Zuo, A. Bernard, B. Hambrecht, P. Lugan, D. Clément, L. Sanchez-Palencia, P. Bouyer, and A. Aspect, “Direct observation of anderson localization of matter waves in a controlled disorder,” *Nature*, vol. 453, p. 891, 2008.
- [124] G. Roati, C. D’Errico, L. Fallani, M. Fattori, C. Fort, M. Zaccanti, G. Modugno, M. Modugno, and M. Inguscio, “Anderson localization of a non-interacting bose-einstein condensate,” *Nature*, vol. 453, p. 895, 2008.
- [125] V. Oganesyan and D. A. Huse, “Localization of interacting fermions at high temperature,” *Phys. Rev. B*, vol. 75, p. 155111, 2007.
- [126] A. Pal and D. A. Huse, “Many-body localization phase transition,” *Phys. Rev. B*, vol. 82, p. 174411, 2010.
- [127] M. Serbyn, Z. Papić, and D. A. Abanin, “Local conservation laws and the structure of the many-body localized states,” *Phys. Rev. Lett.*, vol. 111, p. 127201, 2013.
- [128] N. Yao, C. Laumann, S. Gopalakrishnan, M. Knap, M. Müller, E. Demler, and M. Lukin, “Many-body localization in dipolar systems,” *Phys. Rev. Lett.*, vol. 113, p. 243002, 2014.
- [129] M. van den Worm, B. Sawyer, J. Bollinger, and M. Kastner, “Relaxation timescales and decay of correlations in a long-range interacting quantum simulator,” *New J. Phys.*, vol. 15, p. 083007, 2013.
- [130] P. Reimann, “Foundation of statistical mechanics under experimentally realistic conditions,” *Phys. Rev. Lett.*, vol. 101, p. 190403, Nov 2008.

- [131] M. Rigol, V. Dunjko, V. Yurovsky, and M. Olshanii, “Relaxation in a completely integrable many-body quantum system: An ab initio study of the dynamics of the highly excited states of 1d lattice hard-core bosons,” *Phys. Rev. Lett.*, vol. 98, p. 050405, 2007.
- [132] E. Ilievski, J. D. Nardis, B. Wouters, J.-S. Caux, F. H. Essler, and T. Prosen, “Complete generalized gibbs ensembles in an interacting theory,” *Phys. Rev. Lett.*, 2015.
- [133] T. Langen, S. Erne, R. Geiger, B. Rauer, T. Schweigler, M. Kuhnert, W. Rohringer, I. E. Mazets, T. Gasenzer, and J. Schmiedmayer, “Experimental observation of a generalized gibbs ensemble,” *Science*, vol. 348, no. 6231, pp. 207–211, 2015.
- [134] J. Berges, S. Borsányi, and C. Wetterich, “Prethermalization,” *Phys. Rev. Lett.*, vol. 93, p. 142002, Sep 2004.
- [135] E. Ising, “Contribution to the theory of ferromagnetism,” *Z. Phys.*, 1925.
- [136] M. Srednicki, “Chaos and quantum thermalization,” *Phys. Rev. E*, vol. 50, p. 888, 1994.
- [137] M. Rigol, V. Dunjko, and M. Olshanii, “Thermalization and its mechanism for generic isolated quantum systems,” *Nature*, vol. 452, p. 854, 2008.
- [138] G. D. Palma, A. Serafini, V. Giovannetti, and M. Cramer, “Necessity of eigenstate thermalization,” *Physical Review Letters*, 2015.
- [139] E. H. Lieb and D. W. Robinson, “The finite group velocity of quantum spin systems,” *Communications in Mathematical Physics*, 1972.
- [140] M. Kollar, F. A. Wolf, and M. Eckstein, “Generalized gibbs ensemble prediction of prethermalization plateaus and their relation to nonthermal steady states in integrable systems,” *Phys. Rev. B*, vol. 84, p. 054304, Aug 2011.
- [141] E. T. Jaynes, “Information theory and statistical mechanics. ii,” *Physical Review*, 1957.
- [142] M. A. Cazalilla, “Effect of suddenly turning on interactions in the luttinger model,” *Physical Review Letters*, 2006.
- [143] J.-S. Caux and R. M. Konik, “Constructing the generalized gibbs ensemble after a quantum quench,” *Physical Review Letters*, 2012.